A Multi-constellation Multi-Frequency GNSS Software Receiver Design for Ionosphere Scintillation Studies

Senlin Peng

Dissertation submitted to the Faculty of the

Virginia Polytechnic Institute and State University

in partial fulfilment of the requirements for the degree of

Doctor of Philosophy

in

ELECTRICAL ENGINEERING

Wayne A. Scales, Chair

Jade (Yu) Morton

Jeffrey H. Reed

Tamal Bose

Mazen Farhood

July 27, 2012

Blacksburg, Virginia

Keywords: GNSS, Software Receiver, Ionosphere Scintillation, Vector Tracking Loop

A Multi-constellation Multi-Frequency GNSS Software Receiver Design for Ionosphere Scintillation Studies

Senlin Peng

(ABSTRACT)

Ionospheric scintillations can cause significant amplitude and/or phase fluctuations of GNSS signals. This work presents analysis results of scintillation effects on the new GPS L5 signal based on data collected using a real-time scintillation monitoring and data collection system at HAARP, Alaska. The data collection setup includes a custom narrow band front end that collects GPS L1, L2 IF samples and two reconfigurable USRP2 based RF front ends to collect wideband GPS L5 and GLONASS L1 and L2 signals. The results confirm that scintillation has a stronger impact on GPS L2 and L5 signals than on the L1 signal. Our preliminary results also show that carrier phase and amplitude scintillations on each signal are highly correlated. The amplitude and carrier phase scintillation are also correlated among the three signals.

In this study, a multi-constellation multi-band GNSS software receiver has been developed based on USRP2, a general purpose radio platform. The C++ class-based software receiver were developed to process the IF data for GPS L1, L2C, and L5 and GLONASS L1 and L2 signals collected by the USRP2 front end. The front end performance is evaluated against the outputs of a high end custom front end driven by the same local oscillator and two commercial receivers, all using the same real signal sources. These results demonstrate that the USRP2 is a suitable front end for applications, such as ionosphere scintillation studies.

Another major contribution of this work is the implementation of a Vector tracking loop (VTL) for robust carrier tracking. The VTL is developed based on the extended Kalman filter (EKF) with adaptive covariance matrices. Both scalar tracking loop (STL) and VTL are implemented. Once an error in the scalar loop is detected, the results from the VTL are used to assist the STL. The performance of the VTL is compared with the traditional STL with three different data sets: raw GPS RF data with short signal outages, RF data with

strong scintillation impacts collected during the last solar maximum, and high dynamic data with long interval signal outages from a GPS simulator. The results confirm the performance improvement of the VTL over scintillation impacts and show that the VTL can maintain signal lock during long intervals of signal outage if the satellite ephemerides are available and the pseudorange estimation is within one code chip accuracy. The dynamic performance improvement of the VTL is verified as well. The results show the potential of robust tracking based on VTL during scintillation and interference.

Acknowledgements

I would like to express my gratitude to my supervisor, Dr. Wayne Scales, who have provided support for this research along the way. The work in this dissertation would be impossible without the kind, patient and generous help from him. Special appreciation is given to Dr. Jade Morton for her proficient technical guidance, continuous encouragement, and support throughout my graduate studies. She has impressed me with her hard-working, intelligent and good communication skills. I would also like to acknowledge Dr. Brent Ledvina, who introduced me into the satellite navigation field. The classes taught by Dr. Ledvina in GPS theory and software receiver provided me the chance to study navigation satellite system systematically. His great passion and expertise helped me to shape my professional career.

I would like to express thanks to my committee: Prof. Tamal Bose, Dr. Jeffrey Reed and Dr. Mazen Farhood. Thank you for reading my dissertation, giving me your keen comments, and guiding me through the process of completing my dissertation. I appreciate your comments on my defence. I also want to thank you for being so supportive to be on my oral committee. I am also grateful for my collaborations and friendships with the members and alumni of the GPS lab at Miami University and Virginia Tech: Lei Zhang, Fei Niu, Ruihui Di, Jiao Yu, Jun Wang, Steve Taylor, Ryan Wolfarth, Haiyang Fu and many others. I thank them all.

I sincerely thank my girl friend, Qing He for her understanding, patience and encouragement. Her unending support and love was of great help to me during difficult times of struggle. Finally, and most importantly, I extend my deepest love and gratitude to my parents, and relatives. I cannot finish my Ph.D. study without their support and love.

Contents

List of Tables

List of Figures

List of Acronyms

ADC	Analog to Digital Converter
AGC	Automatic Gain Control
ARNS	Aeronautical Radionavigation Service
BPSK	Binary Phase Shifting Kay
BOC	Binary Offset Carrier
C/A	Coarse Acquisition
CDMA	Code Division Multiple Access
C/N_0	Carrier-to-Noise Ratio
DLL	Delay Lock Loop
DOP	Dilution Of Precision
FAA	Federal Aviation Administration
FDMA	Frequency-division multiple access
FFT	Fast Fourier Transform
FIR	Finite Impulse Response
FLL	Frequency Lock Loop
GDOP	Geometric Dilution Of Precision
GLONASS	Global Navigation Satellite System
GNSS	Global Navigation Satellite System
GPS	Global Positioning System
IF	Intermediate Frequency
KF	Kalman Filter

EKF	Extended Kalman Filter
NCO	Numerically Controlled Oscillator
PLL	Phase Lock Loop
PRN	Pseudo Random Noise
PSD	Power Spectral Density
RAIM	Receiver Autonomous Integrity Monitoring
RF	Radio Frequency
SDR	Software Defined Radio
SNR	Signal-to-Noise Ratio
STL	Scalar Tracking Loop
USRP	Universal Software Radio Peripheral
VTL	Vector Tracking Loop
WBMOD	Wideband Scintillation Model

Chapter 1

Introduction

1.1 Background

The ionosphere is a part of the upper atmosphere, and is formed by the ultraviolet ionizing radiation from the sum. Different regions are produced by different chemical species [Klobuchar et al., 1996]. The ionosphere plays an important role in GNSS applications because it influences radio wave propagation through. Although the ionosphere delay is the biggest error source for satellite navigation systems, it can be directly measured by dual frequency GPS devices, and higher-order ionosphere errors are relatively small (cm for second order, mm for third order) [Morton et al.,2009]. However, deep and frequent GNSS signal fading due to electron density irregularities in the ionosphere raise a concern about the operational availability of navigation system. Transionospheric radio waves interfere constructively and destructively when they pass though electron density irregularities. This phenomenon can be understood as multipath effect inside the ionosphere. As a result, a receiver experiences amplitude fading and phase jitter of the received signal. This phe-

nomenon is referred to as ionosphere scintillation [Crane, 1977; Gwal et al., 2004]. The physical conceptual of ionosphere scintillation is depicted in figure 1.1 [Morton, 2011].

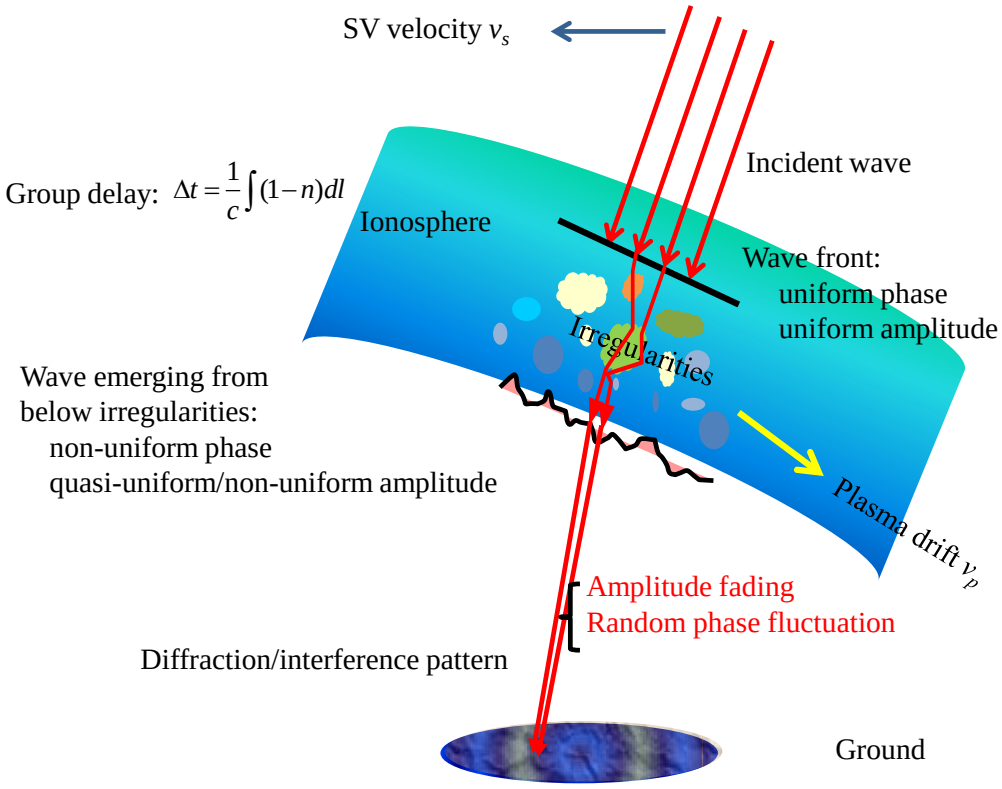

Figure 1.1: Ionosphere scintillation conceptual description.

Figure 1.2 compares the carrier to noise density ratio (C/N_0) of a received GPS signal during a nominal period without scintillation observed and the (C/N_0) during a strong scintillation period collected at Ascension Island in 2001[Zhang et al., 2010]. The (C/N_0) varies slowly and smoothly without scintillation as in Figure 1.2(top). However, if strong scintillation occurs, (C/N_0) fluctuates rapidly and sometimes drops more than 25 dB as in Figure 1.2 (bottom). These deep signal fades were observed in an equatorial area during the past solar maximum (2001). Solar activity follows about an 11-year average solar cycle, and

strong scintillation with deep signal fading is frequently observed for several hours after local sunset during solar maximum.

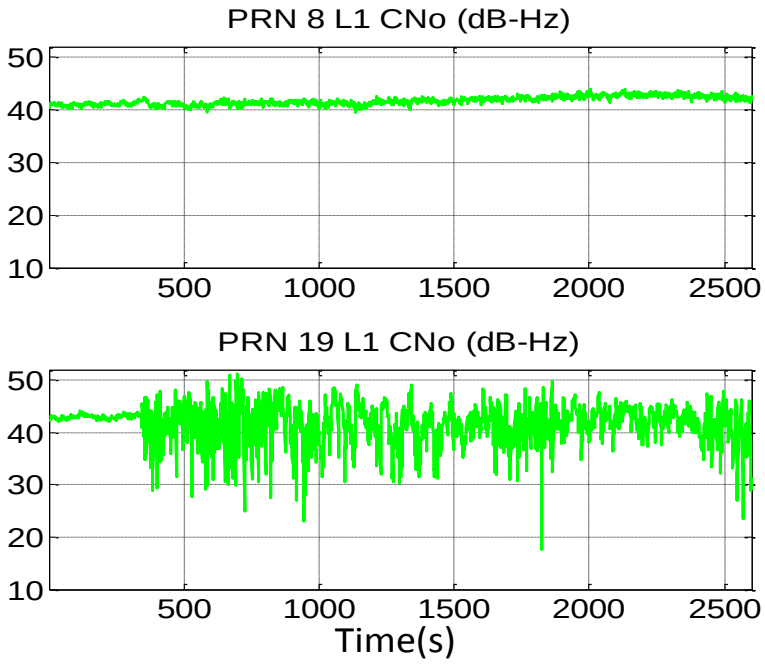

Figure 1.2: Strong scintillation example.

The deep signal fading caused by scintillation may break a receivers carrier tracking lock. Since GPS receivers rely on both code and carrier measurements, the loss of carrier tracking lock of a certain satellite channel can be effectively considered as the loss of the corresponding satellite until the carrier tracking lock is reestablished. GPS positioning requires a minimum of four simultaneously tracked satellites with good geometry [Misra and Enge, 2006; Kaplan and Hegarty, 2006]. If electron density irregularities cover a large portion of the sky, there is a chance that a receiver may lose more than one satellite simultaneously. Simultaneous loss of a significant number of satellites discontinues GPS navigation or degrades the navigation results. Therefore, strong ionosphere scintillation could be hazardous in terms of continuity and availability for GPS solutions. Note that ionosphere scintillation

is not usually observed in the mid-latitude region including the US, but it is frequently observed in the equatorial region including Brazil and India during solar maximum and the high latitude area after local sunset [Basu, 1981; Aarons, 1982]. The global distribution of scintillation activity is shown in Figure 1.3.

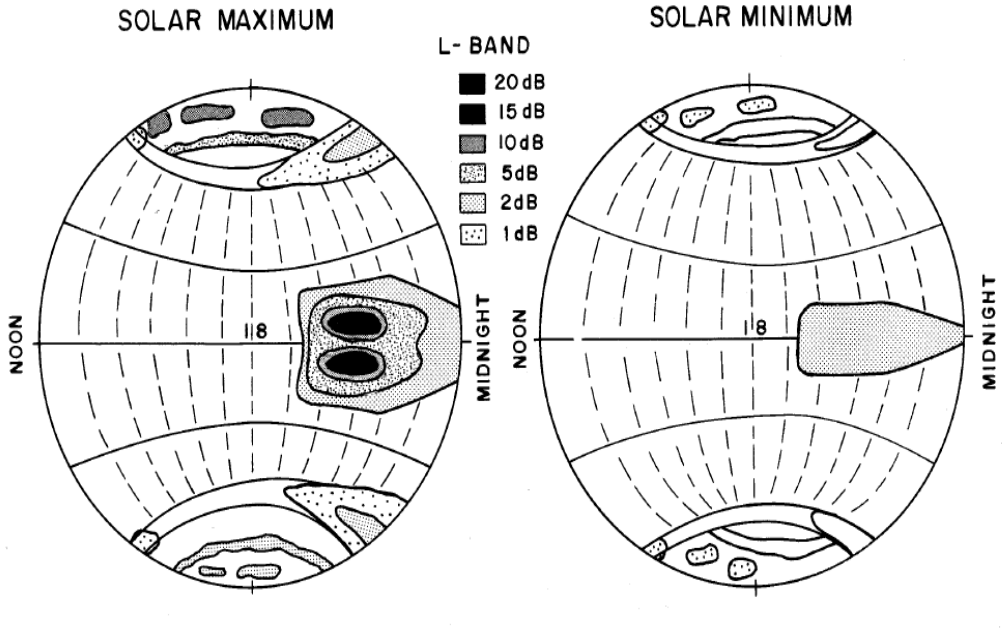

Figure 1.3: Global depth of L-band scintillation fading [Basu, 1981].

Although the physics of the ionosphere scintillation has been studied for several decades (e.g., [Singleton et al., 1961]) and scintillation effects on generic GPS applications are summarized in [Kintner et al., 2007; Beniguel et al., 2007], the characteristics of the scintillation effects on GPS signals are still not well explained, and the current navigation system is still vulnerable to strong scintillation events. As an effort to characterize GPS signal fading under scintillation, [El-Arini et al. 2003] analyzed the depth and the duration of fading based on a strong scintillation data set collected in Naha, Japan during the past solar maximum (2002). It is essential to use high rate GPS data (20 Hz or preferably 50 Hz)

to characterize signal environment in the time-domain, but a very limited number of high rate GPS data sets under strong scintillation is available from the past solar maximum. As already mentioned, solar maxima follow an 11-year average solar cycle. Hence, high rate scintillation data of solar maximum may not be collected until the next solar maximum occurs (around 2012 to 2013) [Kintner et al., 2007]. The lack of natural scintillation data is one of the main difficulties in understanding scintillation impacts on GNSS system.

Scintillations are more intense at the equator than at high latitude areas, and the characteristics are different between these two regions. As opposed to equatorial fluctuations, the polar fluctuations exhibit more phase than intensity fluctuations [Secan et al., 1997]. The scintillation index at high latitude is usually lower than in the low latitude area, but several large scintillation events which cause loss lock of receiver tracking loops haven been reported [El-Arini et al., 2009]at high latitudes. The probability of occurrence is relatively lower during summer than in winter and normally below the values obtained at equatorial regions [Basu, 1981]. Frequent phase fluctuations have been observed at high latitude areas and they may exist all the year. The magnitude of phase fluctuation is quite high and seems to be related to the magnetic activity [Basu, 1981].

A receiver may lose a few satellites simultaneously under strong scintillation, but it can still provide position solutions if it tracks at least four satellites with good geometry. Hence, it is important to know how often deep fades, which is one of the reasons for receivers to lose lock, of multiple satellites occur simultaneously. In other words, the correlation of deep fades between satellite channels under scintillation should be well understood. The impact of scintillation on GPS aviation can be mitigated by the geometric diversity of GPS satellites depending on the correlation level [Seo et al., 2011]. A high correlation of deep fades means that the deep fades of different satellite channels occur simultaneously with

a high probability. In addition to the concern for correlations between different satellites, researchers are also interested in the interval between different deep fadings, and the time delay between different frequencies channels [Seo et al., 2009b]. If a deep fading only last for very short interval, a frequency aided tracking loop can provide good tracking performance to handle scintillation effects. The time delay of scintillation between different frequencies is also quite important. If the time delay is large enough, a dual frequency receiver can maintain lock of the tracking loop by utilizing the Doppler relationship between different frequencies. As dual frequency raw RF data with natural scintillation events were recorded by the scintillation monitoring system [Peng et al., 2010], the detailed analysis of the correlation coefficients and time delay is to be discussed in subsequent works.

1.2 Prior Research

One of the major objectives of this work is to investigate the impact of ionosphere scintillations on L5 signals. The newly launched PRN25 is the first GPS satellite that carries a working L5 signal at the protected ARNS band [Van Dierendonck et.al, 2000]. The L5 signal is intended to provide better assurance for safety-of-life applications such as aviation. With a relatively low carrier frequency at 1.176GHz and a higher chipping rate at 10.23MHz, L5 is more susceptible to ionosphere scintillation compared to the other civilian signals at the L1 and L2 band [Fremouw et al., 1978]. It is well documented that ionosphere scintillations cause increased carrier tracking error and may lead to receiver loss of lock under severe conditions [Seo et al., 2009a; Humphreys et al., 2010a]. For aviation and other applications that require continuity and integrity, ionosphere scintillation poses a threat. This is especially true as we enter a new solar maximum period (2012-

2013) when scintillation activities will increase in both frequency and intensity. The new L5 signal also provides three major new properties that may be beneficial to improve the tracking performance against the ionosphere scintillation. First the signal is broadcasting with signal power of 3dB higher than the L1 signals. Second, a pilot dataless channel enables a pure tracking loop which can provide 6dB tracking threshold improvement. Longer coherent integration interval can also be used in the tracking loop which further improves the tracking performance. The bandwidth of the L5 signal is 10 times of the L1 signal which can provide better interference rejection. In this study, we demonstrate the impact of scintillation on L5 signal based on limited experimental data collected in Alaska.

1.3 Robust GNSS Receiver Tracking Loop Design for Ionosphere Scintillation

The performance of a GPS single frequency receiver in the presence of ionosphere scintillation has been studied in [Knight, 2000; Conker et al., 2003; Humphreys et al., 2010b; Zhang et al 2010]. The previous research to evaluate the robustness of the tracking loops during ionosphere scintillation can be divided into two categories: for the first group, a number of researchers have studied the effects of ionosphere scintillation on tracking loop performance for the GPS L1 signals [Humphreys et al., 2010b]. An excellent research effort was made in the paper [Knight, 2000] to evaluate the ionosphere scintillation effects on GPS receivers. A performance evaluation of different tracking loops under strong scintillation impact is concluded in the paper [Zhang et al., 2010]. In this paper, three carrier tracking loops have been evaluated: the conventional PLL, a FLL-assisted PLL, and a

Kalman filter-based PLL. The natural scintillation RF data from Ascension Island was processed intensively with different noise bandwidth, different coherent integration intervals. The steady state error and tracking robustness performance of these methods are obtained, which indicated that the FLL assisted PLL provided the best tracking performance. The major contribution of Knight's research [Knight, 2000] is using a widely accepted stochastic model of scintillation activity to investigate the effects of scintillations on GPS receivers. The model is closely linked to the Wide Band Scintillation Model (WBMOD)[Secan et al., 1997]. The WBMOD can predict various statistical scintillation parameters based on empirically derived models of the global distribution and behavior of ionosphere scintillation. [Knight, 2000] also derived the expressions of carrier and code tracking errors as a function of scintillation parameters. Intensive studies by Knight have provided the fundamentals for researchers who wish to further investigate overall receiver performance in the presence of scintillation. Another excellent work has been done in [Chiou et al., 2008]. [Chiou et al., 2008] provided a linear model analysis of both the PLL and FLL by considering all of the generic tracking error sources as well as the errors due to ionosphere scintillation. This work suggests that the use of an FLL as a backup tracking loop could effectively overcome ionosphere scintillation. This work also explored the technique of Doppler-aiding for both coherent and non-coherent tracking architectures. The performance of tightly-coupled GPS/INS integration loop was also evaluated. A GPS hardware simulation was developed and implemented for operation in environments which include aircraft dynamic, and strong ionosphere scintillation.

The second group of researchers contributed to determining the tracking loop performance without considering ionosphere scintillation [Hegarty et al., 1997; Chiou et al., 2005; Irsigler et al., 2002]. In particular, most attention in the previous work was focused

on the PLL. A comprehensive FLL linear model study on the noise performance with different frequency discriminators was conducted in [Natali 1984, 1986]. More recently, in [Irsigler et al., 2002], the FLL linear model including various error sources was considered. In the work by [Ward 1998], a FLL assisted PLL (FAPLL) was first developed and the performance of the FAPLL for weak signal and high dynamic situation were compared with the PLL and FLL. A conclusion on several tracking loops performance is detailed in [Hinedi 1985].

Vector tracking loops which track the GPS signals together rather than separately are quite different from the traditional receiver tracking loops. The concept of vector-based tracking can be traced back to the early 1980s [Copps 1980; Sennott 1984]. Vector tracking has several important advantages over scalar tracking loops [Lashley 2009]. The most important advantage is the increased immunity to interference and jamming. Vector tracking loops can minimize the time to re-acquisition of blocked signals. Moreover, vector tracking loops have a larger dynamics range than scalar tracking loops. The vector tracking loop was first detailed by [Spilker 1996], but few details are given on its exact implementation. A more detailed discussion of how to implement vector tracking is given in [Lashley et al., 2009; So et al., 2010]. Specifically in [Lashley 2009], the vector tracking method is demonstrated using data from a high fidelity GPS simulator. The simulation results show the vector tracking algorithms operating at a (C/N_0) of 19dB-Hz through 2 G, 4 G, and 8 G coordinated turns. The vector tracking algorithms are also shown operating through 2 G and 4 G turns at a (C/N_0) of 16dB-Hz. However, there are several things not clarified in the paper by [Lashley et al., 2009]. First, the coherent integration interval is not mentioned. Second, the errors of the tracking loop (phase, frequency) are not fed into the Kalman filter for the measurement update. Third, no information is available in this paper about the

estimation accuracy and stability of the vector tracking loop. Vector tracking loops can be a very efficient method to handle the ionosphere scintillation effects. The outputs of the vector tracking loops provide an estimation of the phase and frequency of the GPS signals which can minimize the impact of the scintillation effect. The lower (C/N_0) tracking threshold of the vector tracking loops makes it an ideal choice of robust signal tracking under strong ionosphere scintillation. Implementation of a vector tracking loop for ionosphere scintillation study is another contribution of this work, and intensive performance test and analysis are included in the later part of this work.

Chapter 2

Acquisition and Tracking of GNSS Signals

2.1 Overview of GNSS

We are experiencing a new era of satellite-based navigation systems with the recent GPS modernization which included L2C, L5, and the planned L1C signals, the increasing number of GLONASS satellites and reformed signals, the emergence of Galileo and Compass constellations, and a multitude of regional and spaced-based augmentation systems. Currently, there are two operational systems, the United States' GPS [Misra et al., 2006] and Russia's GLONASS [Revnivykh, 2010]. There are another two global satellite systems in construction: the Galileo positioning system of European Union [Hein et al., 2005]and the Compass navigation system of China[Cao et al., 2008]. At full development, the Galileo and Compass systems are intended to have about 27 and 35 satellites respectively. We are anticipating a whole family of GNSS systems which may consist of about 120 satellites

by 2020. Moreover, The multi-constellation systems offer diverse signal structures over a wide span of frequencies and improve the spatial coverage at nearly every geographical location on Earth. Figure 2.1 shows the current transmitting and future planned GNSS signals. In addition to enhancing continuity, availability, and integrity of navigation and timing solutions, such a system will enable unprecedented scientific research of the dynamic atmosphere on a global scale. All current navigation signals are broadcasting in L-band. As more systems and signals coming in line, the limited frequency spectrum in L-band is becoming heavily occupied. In the work [Hein et al., 2007], the C-band is proposed as candidate for future news signals.

Table 2.1: Summary

Nation	System	2012	2020
USA	GPS	31 satellites	32 satellites
Russia	GLONASS	30 satellites	32 satellites
EU	Galileo	2 satellites	27 satellites
China	Compass	13 satellites	35 satellites

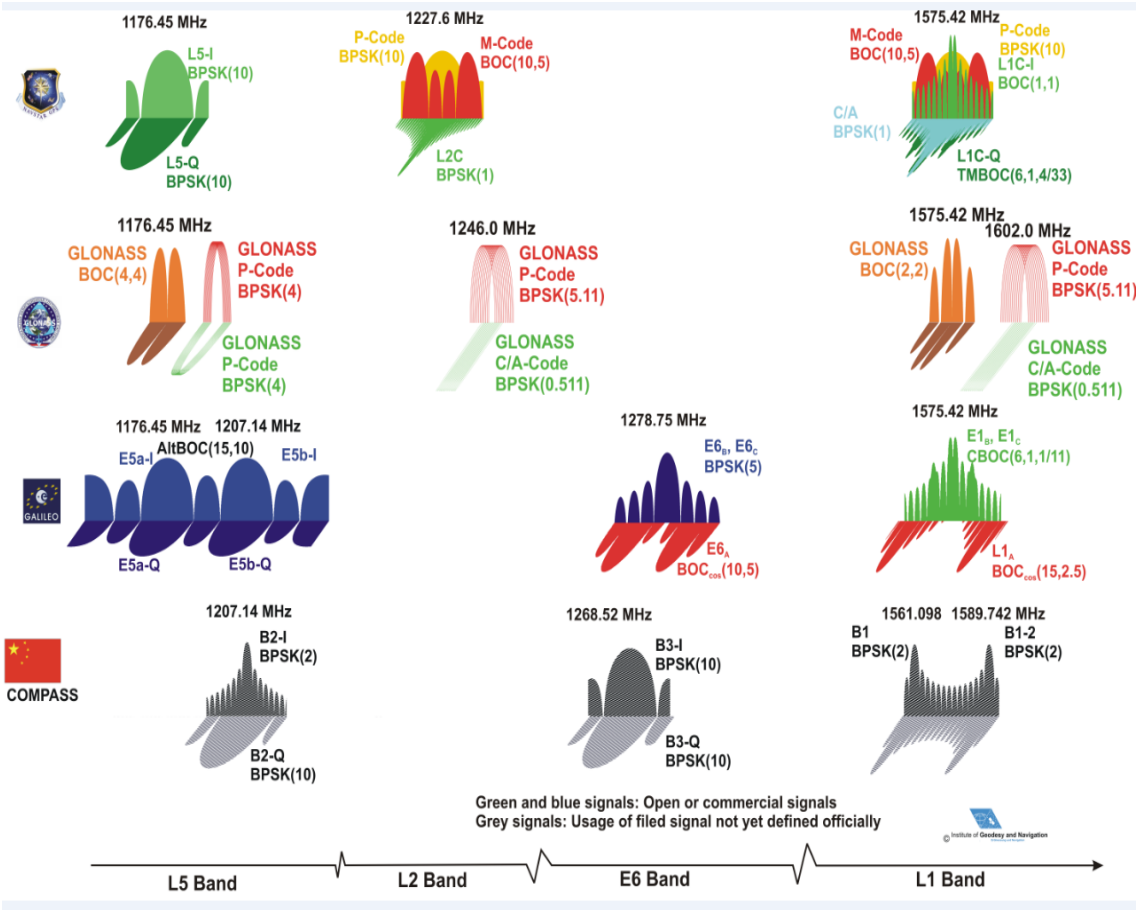

Figure 2.1: GPS, GLONASS, Galileo and planned Compass signals.

2.2 A Review of GNSS Receiver

An entire satellite navigation system consists of three segments: the space segment, the control segment and the user segment. The space segment consists of the satellites, precision clocks, and the signals they transmit to the ground, including the ranging singles and navigation messages. The control segment consists of ground stations. The main function of the control segment is to monitor the performance and control the orbits of all satellites. It also determines the satellite ephemerides by monitoring the ranging signals. The

ephemerides are parameters from which the satellite position can be accurately calculated. The ephemerides are regularly updated by the control segment. The user segment consists of receivers and their applications.

This section provides a brief review of a GNSS receiver. Figure 2.2 shows a typical GNSS receiver block diagram [Akos,1997]. The transmitted radio navigation signals are captured by the antenna firstly. A signal-conditioning process is conducted by the front-end to down-convert the signals from radio frequency (RF) to an appropriate intermediate frequency (IF) to facilitate the acquisition and tracking in the next step. After conditioning, the signal has been amplified to a level close to the range of the analog to digital(A/D)converter. A major task of the GNSS receiver is to estimate the key triplet $\{\tau, f_D, \phi\}$. The arrival time τ contains the information of the code phase. We also need to estimate the f_D to demodulate the navigation messages and get the pseudorange rate information. The carrier phase ϕ is also needed for high accuracy applications. The whole estimation process can be separated into two stages. This first stage is a global search for approximate values of $\{\tau, f_D\}$. This process is also known as signal acquisition. The second stage is called as signal tracking which is continuously searching for accurate estimation of these values. A Phase Locked Loop (PLL) is normally used for coherent signal tracking, while a frequency-locked loop (FLL) is used for no-coherent signal tracking. The details of the implementation of PLL and FLL will be covered in more details in the later part of this chapter.

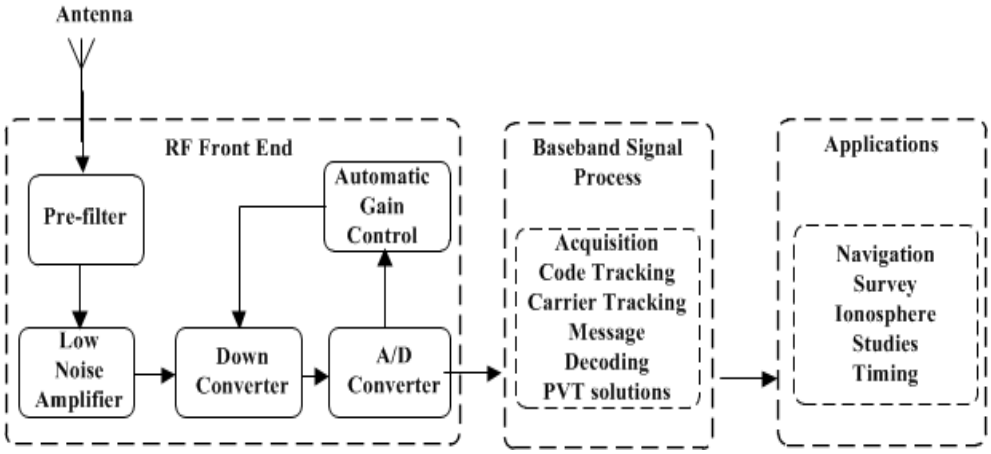

Figure 2.2: Block Diagram of GPS Receiver.

2.3 Signal Acquisition

After the signals pass through the RF front end, the signals are down converted, amplified and digitized. The signals are now well suited for processing. The signal from one satellite has the general form of:

$$S(t) = \sqrt{P}D(t-\tau)C(t-\tau)expj(2\pi(f_{IF}+f_D)t+\triangle\theta)+n(t), \tag{2.1}$$

where $\sqrt{P}$ is the amplitude of the incoming signal, $D(t-\tau)$ is the navigation data, $C(t-\tau)$is the PRN code, $\delta\theta$is the initial phase, f_{IF} is the intermediate frequency, f_D is the Doppler shift frequency, and $n(t)$is the noise. Doppler shift frequency is caused by the relative motion between the receiver and the satellite. The range of the Doppler shift is $\pm 10KHz$ for civilian applications. In order to demodulate the navigation messages from the satellite signal, a local PRN code and carrier must be generated. The purpose of the acquisition is to find out the visible satellites and the coarse values of the Doppler shift frequency and the code phase of the signals. The acquisition results are then used to initialize the tracking

loop. A typical acquisition scheme is shown in figure 2.3 [Misra et al., 2006].

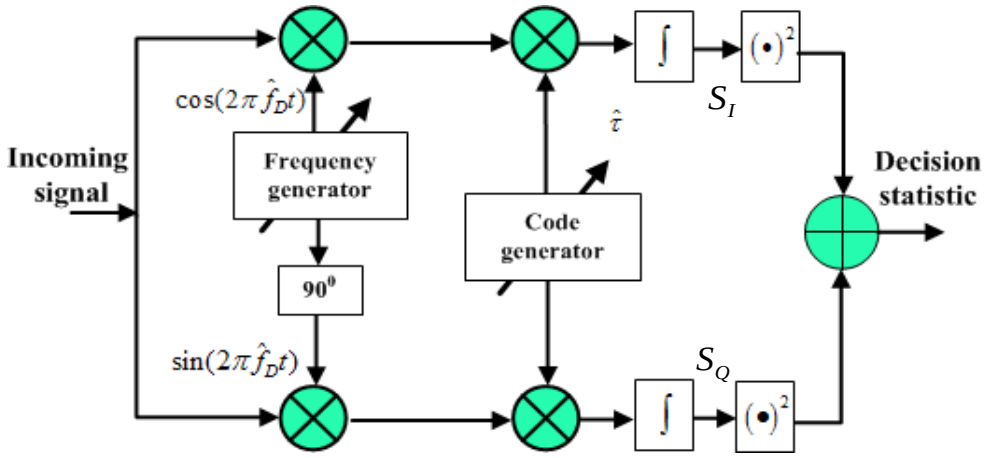

Figure 2.3: The scheme for GNSS signal acquisition.

The acquisition algorithm is based on multiplication of locally generated PRN code and locally generated carrier signals. The auto-correlation of PRN code can be represented by:

$$R(\Delta\tau) = \begin{cases} \dfrac{\tau}{T_C} + 1, & T_C < \tau < 0, \quad (2.2a) \\ \dfrac{-\tau}{T_C} + 1, , & 0 < \tau < T_C. \quad (2.2b) \\ 0, otherwise & (2.2c) \end{cases}$$

As the initial phase of the incoming signal is unknown, the in-phase and quadrature carrier are generated to mix with the input. The resulting signals are coherently integrated, leading to the in-phase and quadrature components S_I and S_Q. It can be shown that [Misra et al., 2006], the S_I and S_Q have the following form:

$$\begin{aligned} S_I(\triangle f_D, \triangle\tau) &= \frac{\sqrt{P}}{2} D sinc(\pi \triangle f_D T_{CO}) R(\triangle\tau)\cos(\triangle\phi) + n_I \\ S_Q(\triangle f_D, \triangle\tau) &= \frac{\sqrt{P}}{2} D sinc(\pi \triangle f_D T_{CO}) R(\triangle\tau)\sin(\triangle\phi) + n_Q \end{aligned} \quad (2.3)$$

where

$R(\cdot)$ is the cross-correlation between the local code and the filtered incoming code;

$\triangle f_D = f_D - \widehat{f_D}$ is the difference between the frequency of the local carrier and of the incoming signal;

$\triangle\tau = \frac{\tau_0 - \tau}{T_s}$ is the difference between the local code delay and the delay of the incoming code, normalized by the sampling interval;

$\triangle\phi$ is the difference between the phases of received and local carriers;

D is a value in the set $\{-1, 1\}$ that represents the effect of the navigation message and of the secondary code;

n_I and n_Q are two independent Gaussian random white noise with variance:

$$\sigma_n^2 = \sigma_{IF}^2 \frac{1}{N} = \frac{N_0 f_s}{2N} \tag{2.4}$$

Given these premises, it is possible to show that the decision variable, obtained as

$$S(\triangle f_D, \triangle\tau) = S_I^2(\triangle f_D, \triangle\tau) + S_Q^2(\triangle f_D, \triangle\tau) \tag{2.5}$$

is a χ^2 random variable with 2 degrees of freedom. When $\triangle f_D \approx 0$ and $\triangle\tau \approx 0$, that is when the local signal replica is aligned with the received signal, $S(\triangle f_D, \triangle\tau)$ is a non-central χ^2 random variable with non-centrality parameters equal to

$$\lambda = \frac{P}{4} sinc(\pi \triangle f_D T_{CO})^2 R^2(\triangle\tau) \approx \frac{P}{4}. \tag{2.6}$$

If the local and the received signal are not aligned, then, due to the orthogonality properties of the spreading codes, it is possible to assume that $S_X(F_D, \tau)$ is a central χ^2 random variable. Usually the presence of a satellite is declared when $S_X(F_D, \tau)$, for a fixed value of F_D and τ, passes a decision threshold β. If the threshold is passed and the signal is present, if it is correctly aligned, a detection occurs. On the other hand, if there is no signal present, or if it is not correctly aligned then a threshold crossing results in a false alarm. Those two conditions are the null and the alternative hypotheses:

H_0**:** The signal is present and correctly aligned with the local replica

H_1**:** The signal is absent or not correctly aligned with local replica

and the false alarm and detection probabilities are defined as

$$P_{fa}(\beta) = P(S(\triangle f_D, \triangle\tau) > \beta | H_1); \tag{2.7}$$

$$P_d(\beta) = P(S(\triangle f_D, \triangle\tau) > \beta | H_0); \tag{2.8}$$

By using properties of non-central and central χ^2 random variables, those two probability results:

$$P_{fa}^{sc}(\beta) = \exp\{-\frac{\beta}{2\sigma_n^2}\} \tag{2.9}$$

$$P_d^{sc}(\beta) = Q_1\left(\frac{\sqrt{\lambda}}{\sigma_n}, \frac{\sqrt{\beta}}{\sigma_n}\right) \approx Q_1\left(\sqrt{\frac{CN}{N_0 f_s}}, 2\sqrt{\frac{N\beta}{N_0 f_s}}\right) \tag{2.10}$$

where $Q_1(a, b)$ is the generalized Marcum Q-function of order 1, defined as

$$Q_K(a, b) = \frac{1}{a^{K-1}} \int_b^{+\infty} x^K \exp\{-\frac{x^2 + a^2}{2}\} B_{K-1}(ax) dx$$

and $B_{K-1}(\cdot)$ is the modified Bessel function of the first kind of order $K - 1$[]. The value β which is also called detection threshold is chosen according to the false alarm rate in equation 2.8.

2.4 FFT Based Signal Acquisition

A more computation-efficient method for signal acquisition is to use the Fast Fourier Transform (FFT) to simultaneously search for all possible code offsets at a particular frequency [Nee et al., 1991]. This method is especially important to achieve high acquisition sensitivity by extending the integration interval. The FFT based convolution is proved in reference

[28]. In order to implement of the FFT based acquisition algorithm, The following steps can be taken:

1 Take the DFT of the PRN code samples c_k to get C_k

2 Select a Doppler frequency

3 Perform complex mixing of the incoming signal with local generated sinusoidal. This operation will shift the incoming signal to base-band signal

4 Compute the DFT of the complex mixing results to get G_k

5 Multiply C_k with the complex conjugate of G_k; i.e., calculate $Z_k = C_k * G_k^*$

6 Take the inverse DFT of Z_k to get the correlation sequence z_k

7 Find the max value of $|z_k|$, if the max value exceeds the threshold, then the satellite is visible and the index is the code phase start position

2.5 Signal Tracking

After the acquisition process is complete, the rough estimation of the Doppler shift frequency and the code phase are computed. The main purpose of the tracking loop is to refine these values, keep tracking, and demodulate the navigation data [Spilker 1996; van Dierendonck 1996; Kaplan and Hegarty, 2006]. First, the input signal is multiplied with a carrier replica. As the initial phase of the incoming signal is unknown, in-phase and quadrature replicas are generated. This multiplication is used to wipe off the carrier from

the signal. Second, the signal is multiplied with a code replica, and the output of this multiplication gives the navigation message. The theory derivation is given in the following part.

In order to obtain the navigation data from the signal, the carrier and the PRN code need to be removed. The carrier removal is done by multiplying the input signal with a replica of the carrier. The local replica has the same frequency and phase with the incoming signal. The product of the multiplication is:

$$S(t) \times exp(-j(2\pi(f_{IF} + \widehat{f_D})t) + \widehat{\delta\phi}) = R(\Delta\tau)exp(-j(\pi(\Delta f_D T_{CO})))sinc(\pi\Delta f_D T_{CO}) \quad (2.11)$$

The derivation above shows that a local carrier replica with accurate frequency and phase and a code replica with the exact phase are essential parts of the tracking loop. The following parts describe the scalar tracking loop in the software receiver in detail. A scalar tracking loop always consists of delay lock loop (DLL), phase lock loop (PLL) or frequency lock loop (FLL) as shown oin figure 2.4 [Akos 1997]. The delay lock loop (DLL) refines the initial estimated code phase by the acquisition loop. The FLL refines the initial estimate of the Doppler frequency and tracks into the future. The PLL tracks the carrier phase and the carrier frequency with high accuracy. The functions of each part of the tracking loop are detailed in next section.

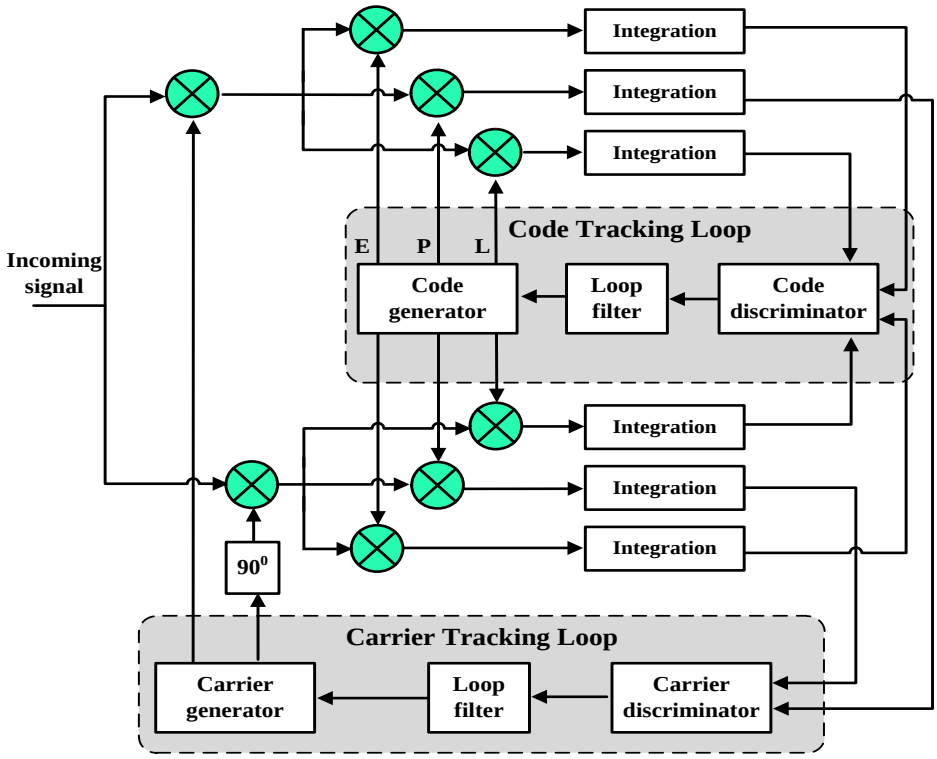

Figure 2.4: Block diagram of software receiver tracking loop.

2.6 Phase Lock Loop

The PLL is a basic building block for many subsystems used in the implementation of modern communication systems. PLLs are widely used in frequency synthesis, for frequency multipliers and dividers, for carrier and symbol synchronization, and in the implementation of coherent receivers [Proakis 2000]. Below is the block diagram of the phase lock loop [Best 1997]:

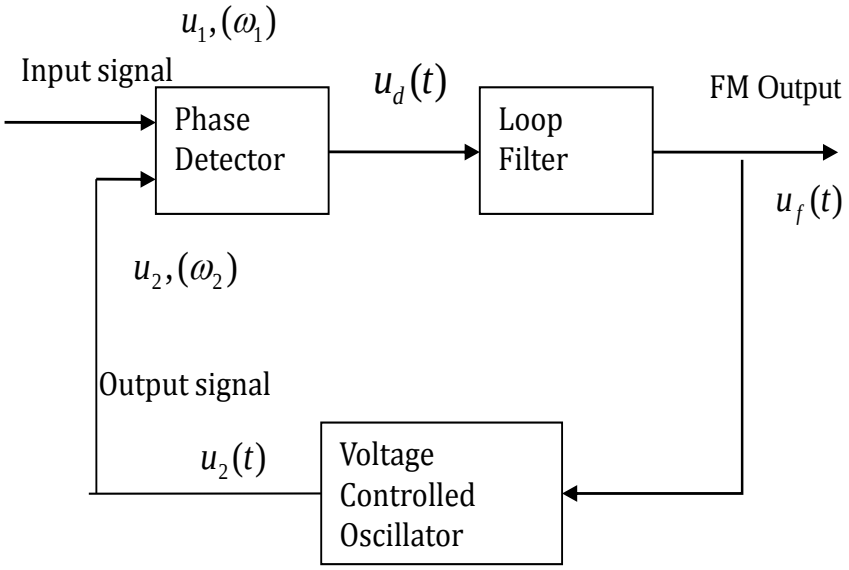

Figure 2.5: Block diagram of the PLL

The signals of interest within the PLL circuit are defined as follows:

1 The reference or input signal $u_1(t)$

2 The angular frequency ω_1 of the reference signal

3 The output signal $u_2(t)$ of the VCO

4 The angular frequency ω_2 of the output signal

5 $u_d(t)$ the output signal of the phase detector

6 The output signal of the loop filter: $u_f(t)$

7 The phase error defined as the phase difference between input and output signals: θ_e

The VCO oscillates at an angular frequency of ω_2, which is determined by the output signal $u_f(t)$ of the loop filter. The angular frequency of VCO is given by:

$$\omega_2(t) = \omega_0 + K_0 u_f(t) \tag{2.12}$$

Where K_0 is the VCO gain.The output signal of the Phase Detector $u_d(t)$ which is approximately proportional to the phase error θ_e.

$$u_d(t) = K_d \times \theta_e \tag{2.13}$$

Where K_d is the gain of the Phase Detector. First we assume the angular frequency of the input signal is equal to the center frequency of the VCO ω_0. The VCO then operates at its center frequency ω_0. In this case, the phase error θ_e is zero. If the phase error is zero, then the output signal u_d of the PD must also be zero. Consequently, the output signal of the loop filter u_f will also be zero. This is the condition that permits the VCO to operate at its center frequency.

Assume now that the frequency of the input signal is changed suddenly by the amount of $\Delta\omega$. The phase of the input signal starts leading the phase of the output signal. A phase error is built up and increases with time. The PD develops an output signal $u_d(t)$ which also increases with time. The output of loop filter, $u_f(t)$, which will also increase with $u_d(t)$. This will cause the VCO to increase the output frequency. The phase error becomes smaller now. After some settling time the VCO will oscillate at a frequency that is exactly the frequency of the input signal. The transfer function which relates the phase θ_1 of the input signal and the phase of the output θ_2 signal is given by:

$$H(s) = \frac{\theta_2(S)}{\theta_1(S)} \tag{2.14}$$

The input signal of a PLL is usually a sinusoidal wave:

$$u_1(t) = U_{10}\sin(\omega_1 t + \theta_1) \tag{2.15}$$

The output signal is usually a square wave and can therefore be written as a Walsh function [Best 1997]:

$$u_2(t) = U_{20}W(\omega_2 t + \theta_2) \tag{2.16}$$

To simplify the analysis, the Walsh function is replaced by the Fourier series:

$$u_2(t) = U_{20}[\frac{4}{\pi}\cos(\omega_2 t + \theta_2) + \frac{4}{3\pi}\cos(3\omega_2 t + \theta_2)\ldots] \tag{2.17}$$

The output signal of the phase detector when ω_1 equals to ω_2 is:

$$u_d(t) = u_1(t) \times u_2(t) = U_{10}U_{20}[\frac{2}{\pi}\sin(\theta_e) + \ldots] \tag{2.18}$$

When the value of θ_e is small, the output can be linearized as:

$$u_d(t) \approx K_d\sin(\theta_e) \approx K_d\theta_e \tag{2.19}$$

The angular frequency of VCO is given by:

$$\omega_2(t) = \omega_0 + K_0 u_f(t) \tag{2.20}$$

The phase θ_2 is given by the integral over the frequency variation:

$$\theta_2(t) = K_0\int u_f(t)dt \tag{2.21}$$

The Laplace transform is given by:

$$\theta_2(S) = \frac{K_0}{S}U_f(S) \tag{2.22}$$

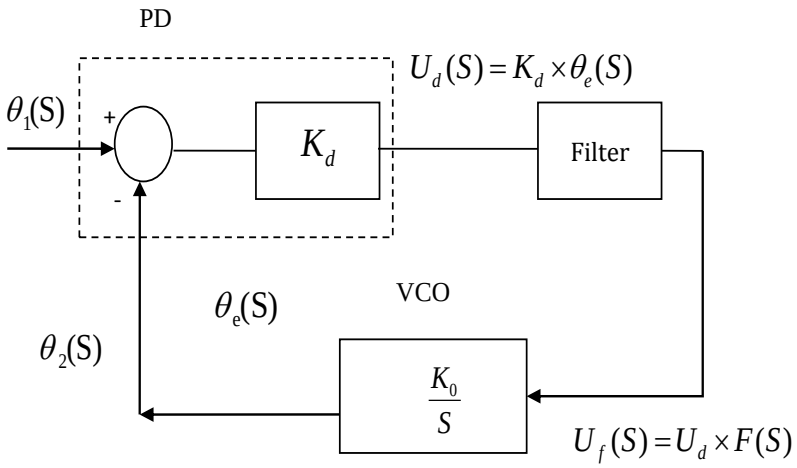

Figure 2.6: frequency domain model of the PLL

Figure 2.6 shows the model of the phase lock loop in frequency domain and how the preceding values related. The input of the loop can be frequency, phase and chips (Delay lock loop). The main purpose of the discriminator is to compute the error between the input and the output, and then we can compute the output through the transfer function. Let the loop gain be:

$$K = K_d * K_0 \tag{2.23}$$

The constant loop gain can be put into the filter function to simplify the phase lock. So the transfer function of the system can be simplified as :

$$H(S) = F(S)/S/(1 + F(S)/S) \tag{2.24}$$

For a second order loop

$$F(S) = K(S + A)/S \tag{2.25}$$

$$H(S) = (K(S + A))/(S^2 + KS + KA) = (K(S + A))/(S^2 + 2\xi\omega S + \omega^2) \tag{2.26}$$

The relationship of these coefficients:

$$\omega^2 = KA, K = 2\xi\omega \tag{2.27}$$

For a second order loop the noise bandwidth is computed as [Spilker 1996]:

$$B_L = \frac{\omega}{8\xi}(4\xi^2 + 1) \tag{2.28}$$

The transformation from continuous time signal to discrete time signal is given by [Oppenheim 2009]:

$$S = (Z - 1)/T \tag{2.29}$$

or

$$S = \frac{2}{T}\frac{1 - z^{-1}}{1 + z^{-1}} \tag{2.30}$$

$$F(S) = \frac{K(S + A)}{S} \tag{2.31}$$

$$F(Z) = \frac{(K(Z - 1) + ATK)}{(Z - 1)} \tag{2.32}$$

The output frequency from the carrier filter is:

$$f = F(Z) \times \theta_e \tag{2.33}$$

In software receiver, the VCO is replaced by a local sinusoid generator program. The new center frequency of the sinusoid can be computed by the equation above if the phase error θ_e is known. The Costas loop is adopted in the GPS receiver to estimate the phase error.

Let the input signal of the Costas loop is $\cos(\omega_{IF}t)$ [Proakis 2000]. The carrier generator generates in-phase $\cos(\omega_{IF}t + \theta_e)$ and quadrature sinusoids $\sin(\omega_{IF}t + \theta_e)$ to mix with the input signal where ω_{IF} is the IF frequency and θ_e is the phase error between in input and the local sinusoid. The in-phase arm mix result is:

$$\cos(\omega_{IF}t) * \cos(\omega_{IF} + \theta_e) = 1/2\cos(\theta_e) + 1/2\cos(2\omega_{IF}t + \theta_e) \tag{2.34}$$

The quadrature arm mix result is:

$$\cos(\omega_{IF}t) * \sin(\omega_{IF} + \theta_e) = 1/2\sin(\theta_e) + 1/2\sin(2\omega_{IF}t + \theta_e) \tag{2.35}$$

Then the mix results are integrated over time interval T. The double IF frequency term is removed by the integration and the following part remains:

$$\frac{1}{2}\cos(\theta_e) \times T \tag{2.36}$$

$$\frac{1}{2}\sin(\theta_e) \times T \tag{2.37}$$

The phase error can be estimated by an *arctan* discriminator:

$$arctan(\frac{\frac{1}{2}\sin(\theta_e) \times T}{\frac{1}{2}\cos(\theta_e) \times T}) = \theta_e \tag{2.38}$$

The noise bandwidth used in the software receiver is 10Hz. The choosing of the loop noise bandwidth is referenced to [Spilker 1996]. The *arctan* discriminator is selected as it is sensitive to frequency error but insensitive to the unknown carrier phase and data bits.

2.7 Frequency Lock Loop

The automatic frequency control (AFC) loop which is also called the frequency lock loop (FLL) is quite similar to the PLL [Best 2003]. In contrast to PLL, the FLL has a better performance in the presence of high Doppler rates, spectrum multipath and ionospheric anomalies. As the result, a FLL is used to lock the Doppler shift frequency prior to the PLL in the software receiver. After incoming signal been tracked by the FLL, the carrier loop switches to the more accurate PLL to get the phase information of the signal. A typical discrete time FLL diagram is shown below in Figure 2.7. The integration filters are used to

limit the input noise and remove double frequency parts after the mixing of the incoming signal and the local sinusoids.

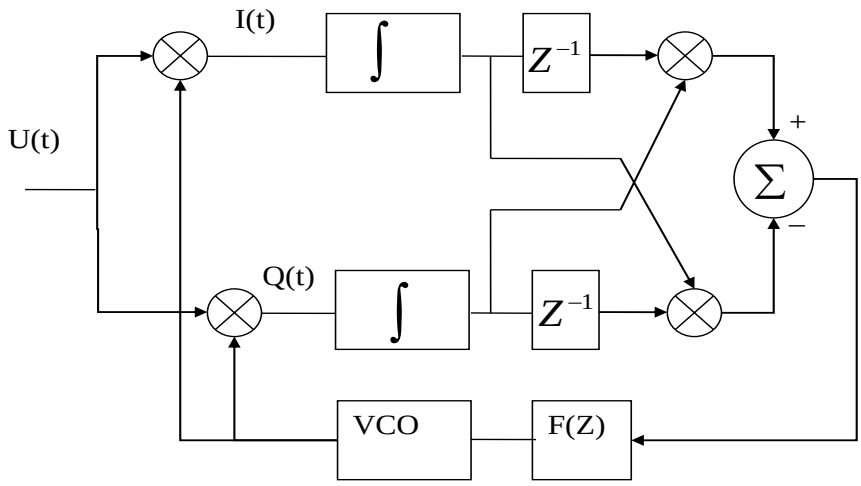

Figure 2.7: Block Diagram of FLL

Figure 2.7 shows the block diagram of the FLL and the effect of noise is not taken into account for simplicity. The initial output frequency of the VCO is an estimation of the incoming signal $f + \Delta f$. We want to keep the VCO output close to the input signal frequency f. The basic operation principle of the FLL is quite similar to the PLL. An in-phase and a quadrature arm are generated to mix with the incoming signal. The mix results for in-phase and quadrature are:

$$I(t) = A\times\cos(2\pi ft)\times\cos(2\pi(f+\Delta f)t) = \frac{1}{2}A\times\cos(2\pi\Delta ft)+\frac{1}{2}A\times\cos(2\pi(2f+\Delta f)t) \quad (2.39)$$

$$Q(t) = A\times\cos(2\pi ft)\times\sin(2\pi(f+\Delta f)t) = \frac{1}{2}A\times\sin(2\pi\Delta ft)+\frac{1}{2}A\times\sin(2\pi(2f+\Delta f)t) \quad (2.40)$$

The high frequency parts are removed by the integrator. Let the integration interval be T.

$$I_{k-1} = \int_0^T A \times \cos(2\pi\Delta f t)dt = \frac{A}{(2\pi\Delta f)} \times \sin(2\pi f T) \tag{2.41}$$

$$Q_{k-1} = \int_0^T A \times \sin(2\pi\Delta f t)dt = \frac{A}{(2\pi\Delta f)} \times (1 - \cos(2\pi\Delta f T)) \tag{2.42}$$

$$\begin{aligned} I_k &= \int_0^T A \times \cos(2\pi(\Delta f t + \Delta f T))dt \\ &= \frac{A}{(2\pi\Delta f)} \times [\sin(2\pi\Delta f 2T) - sin(2\pi\Delta f T)] \end{aligned} \tag{2.43}$$

$$\begin{aligned} Q_k &= \int_0^T A \times \sin(2\pi(\Delta f t + \Delta f T))dt \\ &= \frac{A}{(2\pi\Delta f)} \times [\cos(2\pi\Delta f T) - \cos(2\pi\Delta f 2T)] \end{aligned} \tag{2.44}$$

The discriminator output is represented by

$$D = \frac{(Q_k \times I_{k-1} - I_k \times Q_{k-1})}{(amplitude(I, Q))} \tag{2.45}$$

By some computation we can simplify the discriminator output as:

$$D = \sin(2\pi\Delta f T) \tag{2.46}$$

So after the linearization of the cross product, the result is the difference between the input frequency and the VCO output frequency times the sample interval T.

In the frequency lock loop, the Jaffe-Rechtin filter is chosen as the low pass filter. A second order Jaffe-Rechtin filter is used as an example. The transfer function of the filter is given by [Spilker 1996]:

$$F(s) = \frac{(B^2 + \sqrt{2}BS)}{AKS} \tag{2.47}$$

Where B is the noise bandwidth, A,K are amplify coefficients. In S domain the Laplace transform of integration is:

$$L(\int) = \frac{1}{S} \tag{2.48}$$

The input to the frequency loop is $f + \Delta f$. The output from the loop is f. The purpose of the loop is to compute Δf to update the output of the tracking loop. The transfer function of this system is computed as:

$$H(S) = \frac{(AKF(S))}{(S + AKF(S))} = \frac{(B^2 + \sqrt{2}BS)}{(S^2 + \sqrt{2}BS + B^2)} \tag{2.49}$$

The block diagram implementation of the system is shown in Figure 2.8:

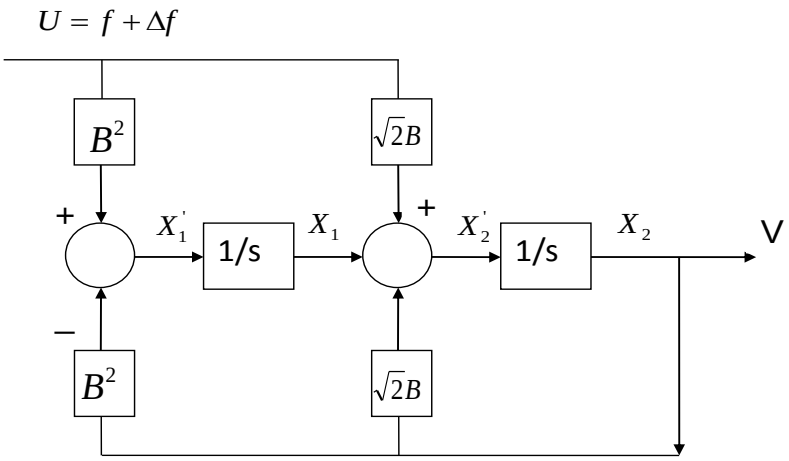

Figure 2.8: block diagram implementation of the FLL

The output of the system is V, the initial guess value of V is f. The initial input value is :

$$U = f + \Delta f \tag{2.50}$$

The state space equations for this system are:

$$X_1' = B^2 \times (U - V) \tag{2.51}$$

$$X_2' = X_1 + \sqrt{2}B \times (U - V) \tag{2.52}$$

$$V = [0\ 1] \times \begin{bmatrix} X_1 \\ X_2 \end{bmatrix} = X_2 \tag{2.53}$$

The Laplace transform of these equations above are:

$$S \times X_1 = B^2 \times (U(s) - V(S)) \tag{2.54}$$

$$S \times X_2 = X_1 + \sqrt{2}B \times (U(S) - V(S)) \tag{2.55}$$

Implementation these equations in discrete time by backward integration is:

$$S = \frac{(1 - Z^{-1})}{T} \tag{2.56}$$

So replace the S in (2.53) and (2.54) we have:

$$X_1(n+1) = X_1(n) + T \times B^2 \times (U - V) = X_1(n) + T \times B^2 \times \Delta f \tag{2.57}$$

$$X_2(n+1) = X_2(n) + T \times X_1 + T \times \sqrt{2}B \times (U - V) = X_2(n) + T \times X_1 + T \times \sqrt{2}B \times \Delta f \tag{2.58}$$

The next states of the registers can be computed by the equations above if the value of Δf is known. From equation (2.45) we have:

$$\theta = \frac{(Q_k I_{k-1} - I_k Q_{k-1})}{(amplitude(I, Q))} = \sin(2\pi \Delta f T) \tag{2.59}$$

From the equation above we can get the frequency offset between the input and output. This offset is used as the input to equation to compute the next state values.

2.8 Delay Lock Loop

The purpose of the code tracking loop is to refine and keep tracking the code phase of the specific ranging code in the signal. The code tracking loop used in this software receiver is the delay lock loop [Spilker 1963]. This loop consists of correlator, accumulator, DLL discriminator and loop filter as is shown in Figure 2.9. The design of DLL is based on

the autocorrelation and cross correlation property of the pseudo random code. The DLL correlates the received signal with a slightly early replica and a slightly late replica. As we know from the autocorrelation property, only when the two codes are perfectly aligned will a peak value be computed. If the two codes are shifted by more than one chip, there is almost no correlation between them. As the shift increases from zero to one chip, the correlation results decrease almost linearly.

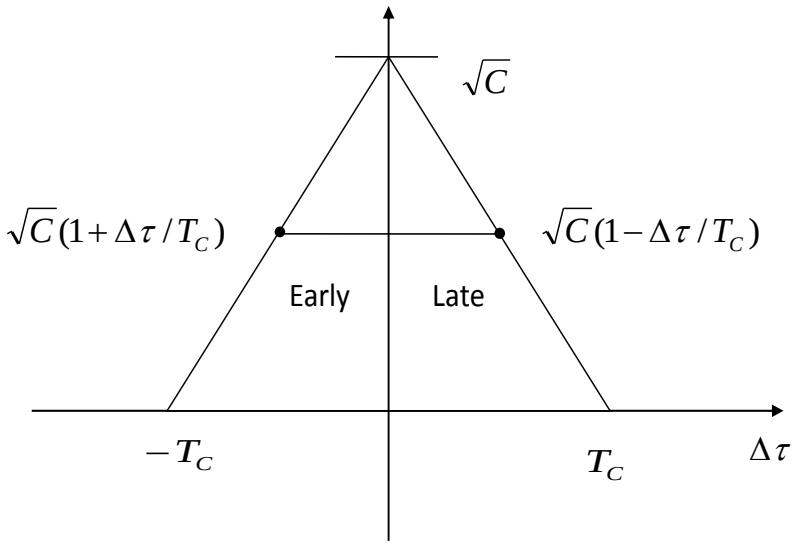

Figure 2.9: Early and Late Correlation Peak

The signal components of the early and late samples are given by:

$$S_E = \sqrt{C}R(\Delta\tau - dT_C/2) \tag{2.60}$$

$$S_L = \sqrt{C}R(\Delta\tau + dT_C/2) \tag{2.61}$$

where $R(\tau)$ is the autocorrelation function, T_C is the length of on chip of the pseudo random code, d is a constant value of the correlator spacing, $\Delta\tau$ is the offset between the prompt code and the object code in the signal, $\sqrt{C}$ is the maximum correlation value.

The time offset be computed by:

$$\Delta\tau = T_C(S_E - S_L)/2\sqrt{C} \tag{2.62}$$

The DLL discriminator provides the linear relationship of the time offset to the correlation results. Several typical types of DLL discriminators are described in the table 4.1 [Akos 1997].

The normalized early minus late envelope delay lock loop is very widely used. It removes the signal amplitude sensitivity, but it is very computationally expensive. The normalized early minus late envelope discriminator is used is this software receiver to track both GPS and GLONASS L1 signals. The difference between the power of early and late is calculated and sent to the discriminator. This difference indicates which one (early or late ranging code) contains more energy. The NCO must advance or delay the locally generated code according to this difference. When the power of the early and late correlators is the same, this means the prompt code lies perfectly with the incoming code and this is the objective of code tracking loop. The result of the discriminator is filtered and sent to the code NCO to update the chip rate of the pseudo random code.

Table 2.2: GLONASS and GPS system comparison

Type	Discriminator	Characteristics
Coherent	$I_E - I_L$	Low computational load. Does not require the Q branch but require a good carrier tracking loop.
Non Coherent	$(I_E - I_L) \times I_P + (Q_E - Q_L) \times Q_P$	Dot-product power. This is the only DLL discriminator that uses all three correlators and this results is the lowest baseband computational load. For 1/2 chip early-late spacing, it produces true tracking error within 0.5 chip of input error.
	$(I_E^2 - I_Q^2) + (Q_E^2 - Q_Q^2)$	Early-minus-late power. Moderate computational load. For 1/2 chip early-late spacing, it produces true tracking error within 0.5 chip of input error.
	$\frac{((I_E^2 - I_Q^2) + (Q_E^2 - Q_Q^2))}{((I_E^2 + I_Q^2) + (Q_E^2 + Q_Q^2))}$	Normalized early minus late envelope. Highest computational load. For 1/2 chip early-late spacing, it produces true tracking error within 0.5 chip of input error. Becomes unstable at 1.5 chip input error.

Chapter 3

Multi-constellation Multi-frequency GNSS Software Receiver Design

3.1 Chapter Overview

Existing deployment of ionosphere scintillation monitoring systems are limited to single frequency GPS receivers or at most dual frequency GPS receivers operating at the L1 and L2 bands [Groves et al., 2000; Van Direndonck et al., 1993; Skone et al., 2008]. The multi-constellation multi-frequency GNSS software receiver [Peng et al., 2011] described here offers many advantages over these systems. The first and also the most important advantage is that the software based receiver can be used to test tracking algorithms intensively as the flexibility of the software receiver. The multi-constellation systems also offer diverse signal structures over a wide span of frequencies and improve the spatial coverage at nearly every geographical location on Earth. The spacial distribution and the correlation between different frequency band can be explored by processing scintillation data on multiple frequency

bands.

The other advantage is due to the fact that GPS satellites have limited coverage at the aurora zone where scintillations frequently occur. GNSS satellites such as those in the GLONASS offer more high latitude coverage and can be used to fill the gaps left by GPS. The sheer number of combined satellites in all available constellations will increase the spatial resolution of the ionosphere tomography derived from the spaced GNSS receivers. A real-time scintillation monitoring and data collection system have been set upped at HAARP in Alaska. The software receiver is developed for the post signal processing of scintillation raw IF data and for advanced navigation algorithms development.

Currently, the software receiver is capable to process signals from GPS(L1,L2CM,L2CL, L5I, L5Q), GLONASS (L1,L2,L3) and Galileo (E1-EB, E1-EC) signals. The software receiver is able to provide PVT measurements for both GPS and GLONASS systems, as well as scintillation indies. The signal processing algorithms for Galileo E5 signals are also under further testing. An early-prompt-late Delay Lock Loop (DLL) with a adjustable chip correlator spacing is used in the software receiver for the code tracking. An advanced Vector Tracking Loop assisted Scalar Tracking Loop is also developed based on Extened Kalman filter. The detail implementation of the advanced tracking loop is to be detailed in later part of the thesis. The discriminators used for the FLL, PLL, and DLL are listed below [Peng et al., 2010]:

$$D_{FLL} = (sign(I_{P-1}I_P + Q_{P-1}Q_P) \times (I_{P-1}Q_P - I_PQ_{P-1}))/(2\pi T) \quad (3.1)$$

$$D_{PLL} = a\tan(Q_P/I_P)/(2\pi T) \quad (3.2)$$

$$D_{DLL} = \frac{(I_E^2 + Q_E^2) - (I_L^2 + Q_L^2)}{(I_E^2 + Q_E^2) + (I_L^2 + Q_L^2)} \quad (3.3)$$

3.2 Review of GPS Civilian Signal Structure

The current GPS system is broadcasting civilian signals at L1 (1575.42MHz), L2(1227.6MHz) and L5 (1176.45MHz)band. The signal structure and content for L1 and L2C are fully covered in [Van Dierendonck et.al, 2000]. A dual frequency (L1 & L2C) software receiver for scientific research has been developed on DSP in [OHanlon et.al, 2011]. This dual frequency receiver has demonstrated the potential applications of software receivers. In this work, a triple frequency (L1,L2C and L5) software based GPS receiver is implemented.

The L5 signal is part of the GPS modernization to improve GPS performance for civilian users [Gao et al., 2009b]. It consists of the two equal power components, the in-phase and data-less quadrature component. Each component is a BPSK signal with 10.23MHz chip rate and 1 millisecond (ms) code period. For the in-phase component, the PRN code is further modulated by the navigation message and a 10-bit NH sequence (NH10: 0000110101). For the quadrature component, the PRN code is modulated by a 20-bit NH sequence (NH20: 00000100110101001110). The NH code sequence length is 1 ms, therefore, NH10 and NH20 sequence length are 10 and 20 ms, respectively. The in-phase and quadrature channel are QPSK-modulated with the L5 carrier at 1176.45MHz. The 50bps navigation data bits on L5 are $1/2$ encoded with a Forward Error Correction (FEC) code which results in a symbol rate of 100sps. The FEC technique provides better bit error rate (BER) performance by making use of redundant data bits. The PRN code generation polynomials are provided in [Van Dierendonck et.al, 2000] as well as the initial values for the registers.

The combination of registers used in the L5 FEC encoder is shown in figure 3.1. The corresponding constraint length is 7 and the code generator polynomials for the upper and

lower outputs are given by equations 3.4 and 3.5:

$$G_1(X) = 1 + X + X_2 + X_3 + X_6 \tag{3.4}$$

$$G_2(X) = 1 + X_2 + X_3 + X_5 + X_6 \tag{3.5}$$

The Viterbi algorithm (VA) [Viterbi et al., 1967] is the classical approach to decoding convolutional code. The VA can be simply described as an algorithm which finds the most likely path or the path with minimum bit error through a set of observations. The recommended trace back length of $5 \times K$ is used in the VA, where $K = 7$ is the constraint length. The method implemented in this paper is based on [Forney 1974]. Interested readers may find more detailed description of the method in [Heller et al., 1971].

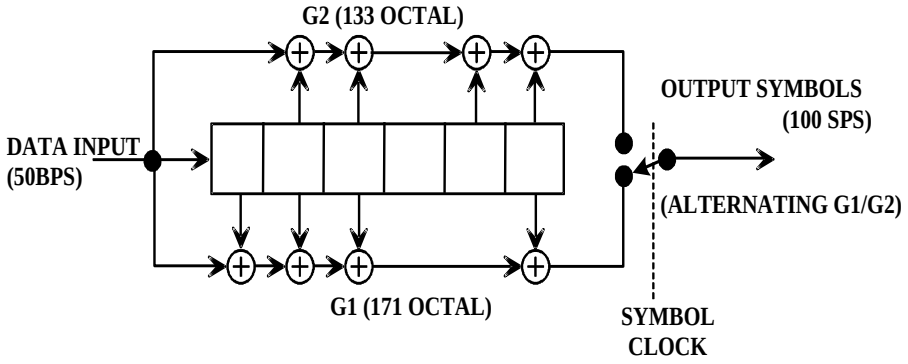

Figure 3.1: GPS L5 FEC convolutional encoder.

The message content of L5I is similar to that of the L1 signal. The bit length of the message word is 300bits as shown in figure 3.2. The first 8 bits are the preamble bits. The 17 bits TOW contained in the navigation message provide the GPS time of the next message frame. The last 24 bits are cyclic redundancy check (CRC) data bits for parity check. The generator polynomial for the CRC parity check is provided in [GPS ICD 705] and figure 3.3 shows the logic implementation of the CRC parity check [Peterson et al., 1961].

The first 276 bits in the navigation message are used as inputs for the generator polynomial. If the final states of all registers have the same values as the last 24 bits of the navigation message, then the parity check of the data bits is verified. After extracting the time information from the navigation message, the tracking results of different channels can be synchronized with the GPS time.

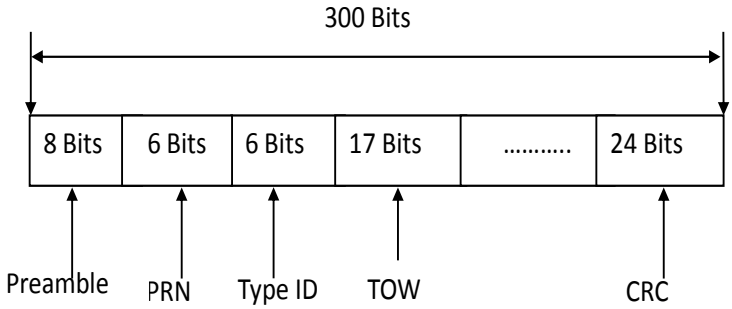

Figure 3.2: GPS L5 message content.

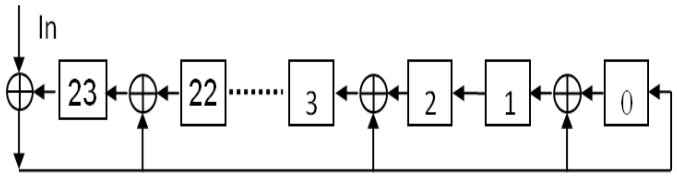

Figure 3.3: CRC-24Q implementation logic.

The performance of the L5 has been extensively evaluated [Tran 2004]. The code tracking error of L5 due to thermal noise and wide-band interference are lower than that on L1 signals. The carrier tracking of the L5 is much more robust than L1 with a tracking threshold improvement of 3.5 dB. The L5 code also provides better performance for longer delay multipath as a smaller chip length is used in L5 than in L1. However, the real ionospheric

scintillation impact on the L5 remains unknown as scintillation data on L5 is very scarce [Seo et al., 2009a]. In the paper by [Kim et al., 2003], a frequency domain scintillation model is used to evaluate the performance of L5. But frequency correlation among L1, L2, and L5 were not discussed.

3.2.1 Triple Frequency GPS Software Receiver Development

The first satellite (GPS GPS Block IIF SVN62)that transmits the operational L5 signals was successful launch on May 28, 2010. The software GNSS receiver is applied for the processing of 300 seconds of L1, L2C, and L5 signals collected on July 10, 2010 starting at 13:46:39.615 UTC time in Oxford, OH ($39^0 31' N$, $84^0 45' W$). The satellite elevation and azimuth were centered at approximately 31.5^0 and 74.73^0 during this short time interval. The Transform-Domain Instrumentation Global Navigation Satellite System Receiver (TRIGR), a triple frequency RF front end and data collection system designed and built at the Ohio University Avionics Engineering Center, and a Novatel 703GGG antenna were used to collect the RF samples. The receiver samples the L1, L2C, and L5 signals with 8-bit resolution at 56.32MHz frequency. This article presents preliminary receiver code and carrier tracking results and analysis of the signal qualities.

FFT-based batch processing algorithms were used to acquire and track the L1 CA signal first. The code and carrier information obtained from the L1 CA signal are then used to acquire and track the L2 CL and CM, and the L5 in-phase (L5I) and quadrature (L5Q) signals. A 2nd order DLL and 3rd order PLL were used to track all of the signals. To facilitate comparisons of the signals, the dateless signals on L2 CL and L5Q are both tracked with the conventional Costas PLLs. We used a 1 ms integration time, 1 Hz code loop bandwidth,

and 15 Hz carrier tracking loop bandwidth to track each of the signals. Figure 3.4 shows the Doppler frequencies obtained for all three signals. Based on the most recent Yuma Almanac data, we computed that at Oxford, OH, SVN62 reaches the highest elevation of 31.5 degrees at near 13:49 UTC. The Doppler frequencies clearly show agreement with this calculation.

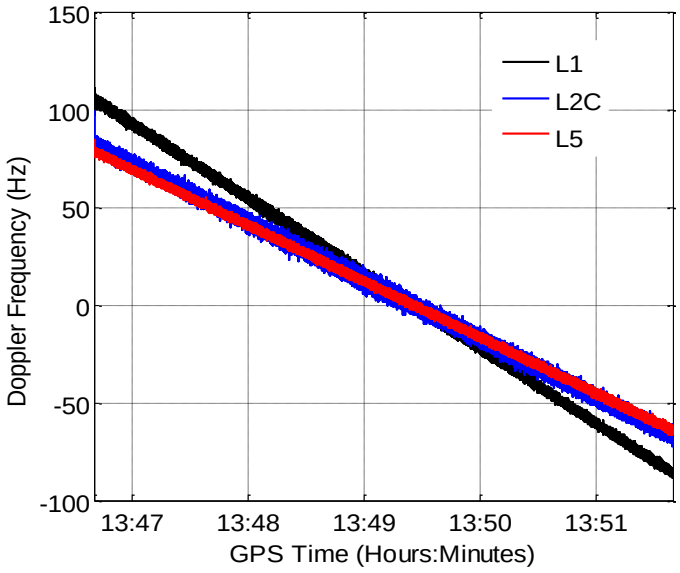

Figure 3.4: Doppler frequencies obtained from the carrier tracking loops for L1, L2C, and L5 signals.

Figure 3.5 shows the carrier to noise ratios (C/N_0) of the three signals over the 300 seconds interval. In computing C/N_0, we used a 20 ms integration time and the results are averaged over 1 second intervals for all three signals. Note that we used the conventional Costas PLL to track all three signals without taking advantage of the data-less pilot signals at the L2 CL and L5 in-phase channel as a means of comparisons. L1 CA signal C/N_0 is about 3dB above that of L2C, while the L5 signal appears to have less multipath-like features in its C/N_0. This is most likely due to the smaller chipping length or wider bandwidth of the

L5 signals.

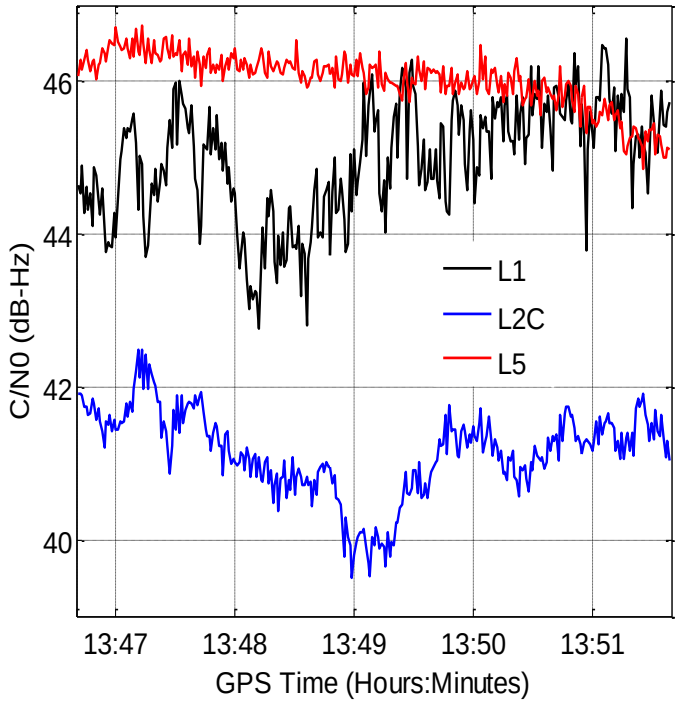

Figure 3.5: Carrier to noise ratios for L1, L2C, and L5 signals.

Figure 3.6 shows one second of example I (solid black lines) and Q (dashed gray lines) channel accumulations for the L1 CA (top panel), L2 CM (middle panel), and L5 in-phase (bottom panel) signals. These sequences are generated one second after the initialization of the tracking loops. Figure 3.7 show the I/Q constellation plots for the L5 signal. The measured phase quadrature angle is 89.6 degree, which is very close to the ideal value of 90 degrees for QPSK modulation.

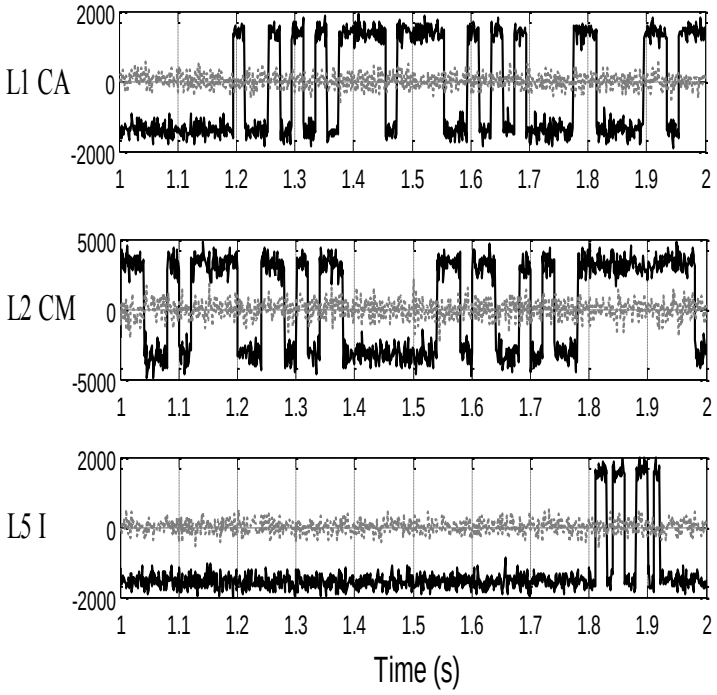

Figure 3.6: Accumulated I and Q Channel outputs for L1 CA (top), L2 CM (middle), and L5 In-phase (bottom) signals. A total of 1 second of data accumulations is plotted here starting at 13:47:39.615.

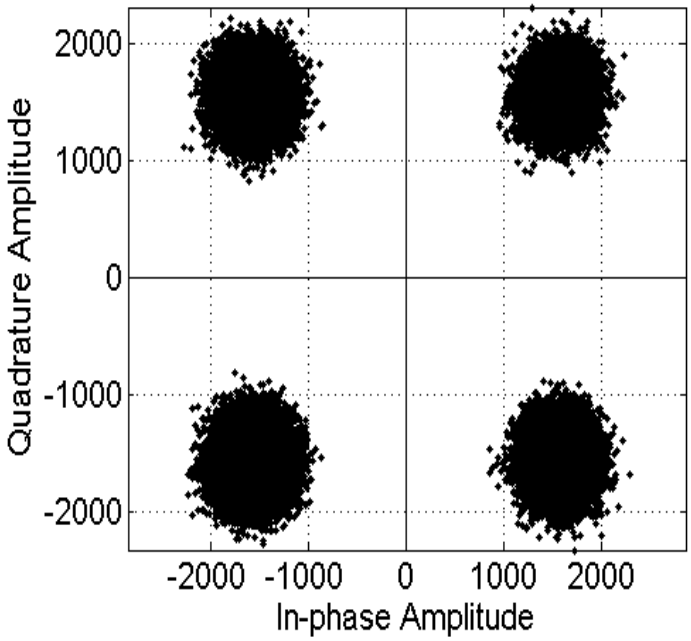

Figure 3.7: L5 signal I-Q constellation plot using the entire 300 second accumulation results.

Figure 3.7 shows the carrier phase minus code phase results for the L1 CA, L2 CM, L5 in-phase, and L5 quadrature during the 300 second tracking interval. The L5 signal observables are much less noisy compared to the L1 and L2C signals due to its wider signal bandwidth. The standard deviation of the observables are 3.4m, 3.7m, 3.7m, 0.4m, 0.4m for the L1 CA, L2 CM, L2 CL, L5I, and L5Q respectively. Note also that both the L5I and L5Q signals show the slight downward trend during the 300 second interval. This is due to the ionosphere induced code-carrier rate divergence contribution to the L5 signal observables. To validate this argument, we computed the relative ionosphere total electron

content (TEC) using the L1 and L2 carrier phase outputs ϕ_1 and ϕ_2:

$$TEC = \frac{f_{L1}^2 f_{L2}^2}{40.3(f_{L2}^2 - f_{L1}^2)}(\phi_1 - \phi_2) + TEC_0 \tag{3.6}$$

where TEC_0 is a constant offset due to the cycle ambiguities in carrier phase measurements. Equation (3.6) can be used to obtain the L5 signal code-carrier divergence:

$$\triangle L_5 = 2 \times \frac{40.3TEC}{f_{L5}^2} = \frac{2f_{L1}^2 f_{L2}^2}{f_{L2}^2 - f_{L1}^2}(\phi_1 - \phi_2) + \triangle L_{50} \tag{3.7}$$

We plotted ΔL_5 in Figure 3.8 to show the general agreement between the derived code-carrier divergence from the L1 and L2 measurements and the direct L5 code minus carrier observables. Note that we arbitrarily set the offset ΔL_{50} to 0 at 13:49 for the convenience of comparison. A divergence rate of approximately -5mm/s is observed on the L5 signal during the 300 second tracking period.

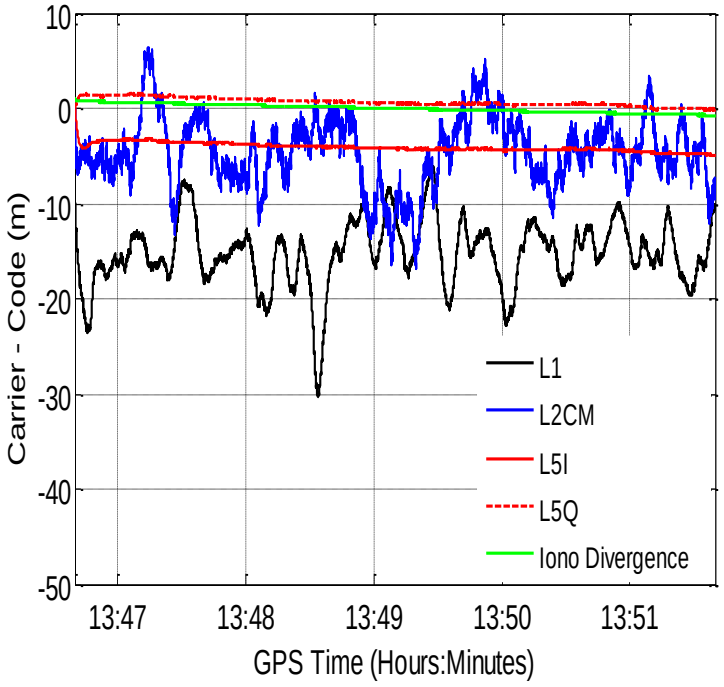

Figure 3.8: Code phase minus carrier phase results based on L1, L2 CM, L5I, and L5Q code

and carrier tracking loop outputs, and ionosphere code-carrier divergence at L5 computed using L1 and L2 carrier tracking loop outputs.

3.2.2 Signal Quality Analysis

We apply periodic averaging to the input samples prior to correlation operations for signal quality analysis. Figure 3.9 shows clearly the code structure of the received PRN25 signals after applying the pre-correlation periodic averaging technique to the baseband signals. The first 13.6 chips of the L1 C/A signal and the first 136 chips of L5 I and L5 Q signal are shown in the figure. They are in accordance with IS-GPS-200D and IS-GPS-705 specifications.

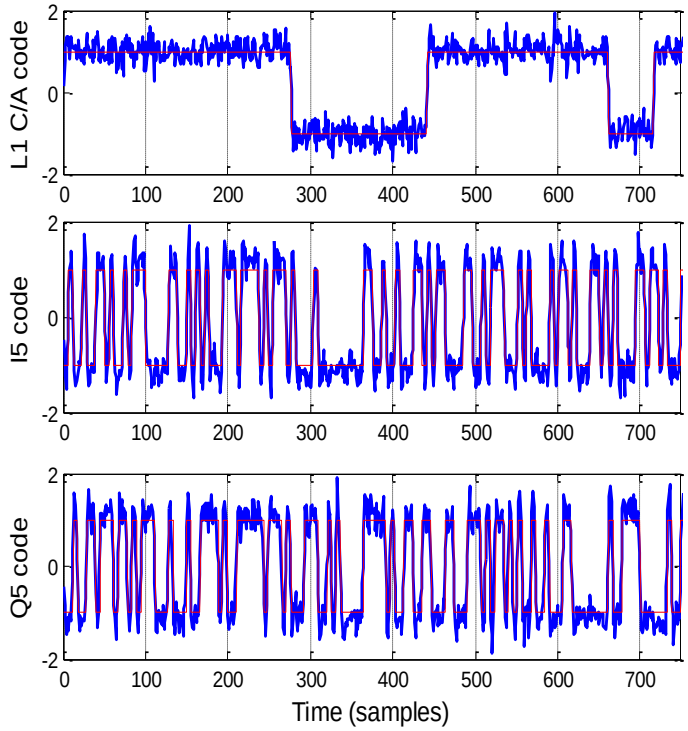

Figure 3.9: PRN 25 L1 and L5 signal code structure as revealed by the pre-correlation periodic averaging.

Since the pre-correlation signal power is far below that of the noise floor, we can't observe a clear PSD of the RF/IF/baseband signals directly. Through periodic averaging, the PSD envelope of the baseband L1 and L5 signals can be clearly seen in Figure 3.10. A total of 16s of input samples were used to obtain the PSD shown in Figure 3.10.

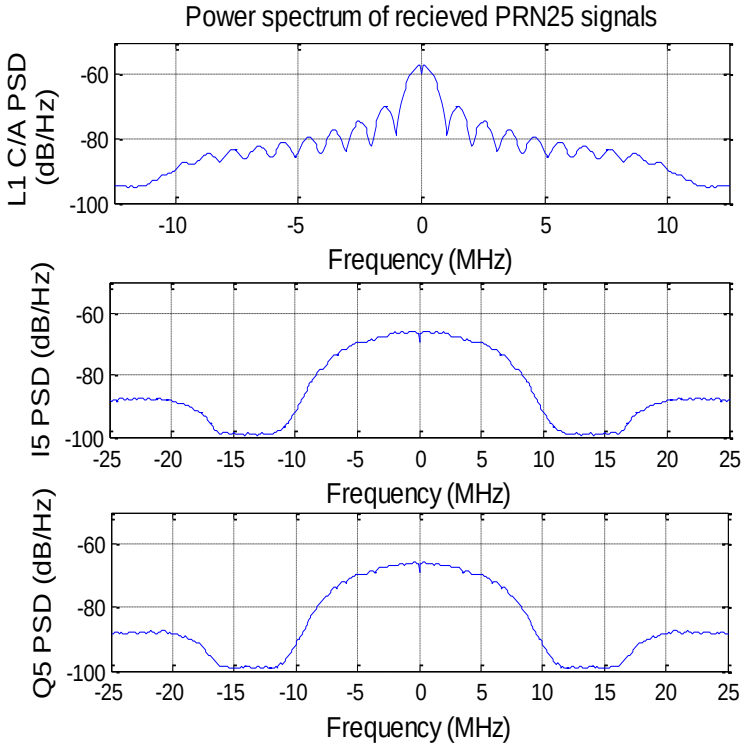

Figure 3.10: PSD of PRN 25 L1 CA, L5 I and Q signals obtained through period averaging.

Correlation function is fundamental for signal distortion and navigation performance analysis. The normalized cross correlation function (CCF) in Figure 3.11 is calculated according to [Peng et al., 2010]:

$$CCF(\epsilon) = \frac{\int_0^{T_p} S_{BB-PreProc}(t) \cdot S_{Ref}(t-\epsilon)dt}{\sqrt{(\int_0^{T_p} |S_{BB-PreProc}(t)|^2 dt) \cdot (\int_0^{T_p} |S_{Ref}(t)|^2 dt)}} \tag{3.8}$$

where $S_{BB-PreProc}(t)$ is the recovered baseband signal after pre-processing (including filtering by a 20MHz bandwidth front end filter, carrier and data wipe-off, with periodic

averaging to reduce the impact of noise on the results),S_{Ref} is the local reference signal with ideal binary C/A code,T_P is the integration period.

Correlation Loss refers to the power loss of the desired signal with respect to the total received signal power during the cross correlation operation with the local reference of the desired signal. It can be calculated from CCF:

$$P_{CCF}[dB] = \max_{over\ all\ \epsilon} (20 \cdot \log_{10}(|CCF(\epsilon)|)) \tag{3.9}$$

The results in Figure 3.11 indicate that the total correlation loss, including the loss caused by SV modulation and filter imperfections, receiver processing loss (due to limited filter bandwidth and other non-ideal processing), and propagation channel distortion. The smaller ratio of the processing bandwidth to the signal bandwidth leads to a larger correlation function distortion and larger correlation loss for L5 signals than for L1 signals.

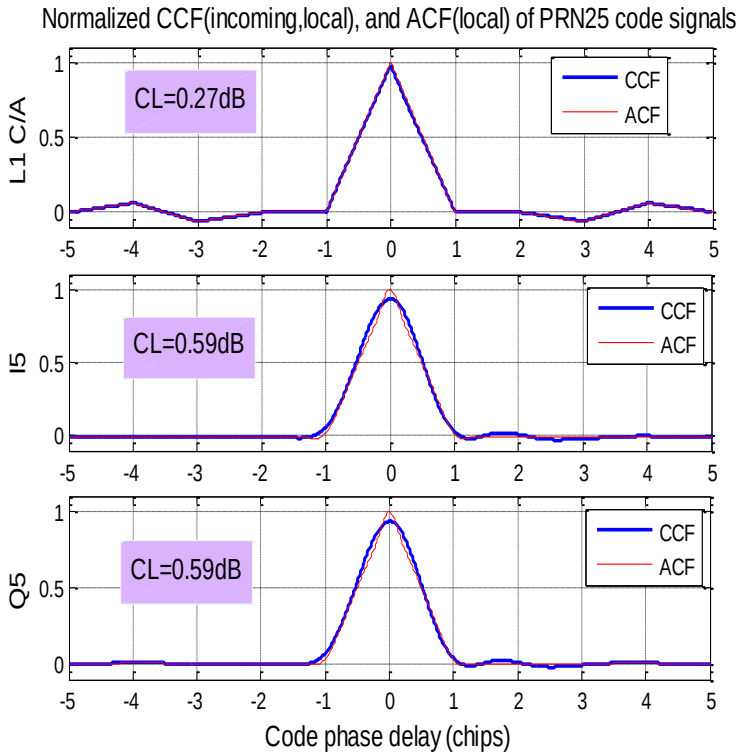

Figure 3.11: Normalized cross correlation function (compared with the ideal auto correlation function of PRN 25 code) and correlation loss of the received PRN25 L1 C/A , L5 I and Q signals.

3.3 GLONASS Signal Processing

The GLONASS system is another fully optional navigation system which contains 30 MEO satellites currently. They orbit at an altitude of 19100 km and at an inclination angle of 64.8^o [Revnivykh 2010] . In contrast to GPS, GLONASS is a Frequency Division Multiple Access (FDMA) system. There are two types of signals, a standard precision (SP) signal in L1 band and an obfuscated high precision (HP) signal in L2 band.

As mentioned previously, GLONASS uses (FDMA) modulation to provide a receiver access to each satellite signal. This means each satellite transmits its carrier signal on its own sub-band. The nominal values of transmitted L1 carrier frequencies are defined by the following equations [GLONASS ICD 2002]:

$$f_{L1k} = f_{L10} + k \times \triangle f_{L1}, f_{L10} = 1602MHz; \triangle f_{L1} = 562.5KHz \tag{3.10}$$

$$f_{L2k} = f_{L20} + k \times \triangle f_{L2}, f_{L20} = 1246MHz; \triangle f_{L2} = 437.5KHz \tag{3.11}$$

where the channel number k ranges from -7 to 13 (0 inclusive), f_{L1k} and f_{L2k} are the transmitted carrier frequency on L1 and L2 band; $\triangle f_{L1}$and $\triangle f_{L2}$ are the frequency offset between carriers. Currently, the GLONASS satellites use frequency channels with $m = [-2, 7]$. Both L1 and L2 sub-carriers are modulated by a modulo-2 addition of a pseudorandom (PR) ranging code, the navigation data bits, and the meander code. The PR ranging code has a chipping rate of 511k chips per second and a period of 1 millisecond. The data bit rate

of the navigation data bits is 50 bps, and the meander code has a bit rate of 100 bps. This meander code is phase-locked to the navigation data bits such that the resultant received navigation message has a bit rate of 100 bps. The PR ranging code, which is the same for each satellite, is generated using the polynomial [GLONASS ICD 2002]:

$$G(x) = 1 + x^5 + x^9 \tag{3.12}$$

The acquisition and tracking GLONASS signals are quite similar to GPS signals. The same tracking loop parameters are used in this dual frequency GLONASS receiver as the GPS receiver described in the previous section.

3.3.1 Navigation Data Processing

The navigation message provides the user with requisite data for determining the satellite positions, satellite clock offsets, satellite health, satellite time, etc. The structure of the GLONASS navigation message consists of super-frames, sub-frames, strings, and bits. The super-frame has a duration and nominal repetition rate of 2.5 minutes. Each super-frame consists of five subframes, where each subframe has a duration of 30 seconds. Each subframe consists of 15 strings, each with a duration of two seconds. The first 1.7 seconds of the GLONASS message string is 85 bits of navigation data encoded by a relative code (also called a differential code), and the last 0.3 second is the 30-bit time mark, which is used to locate the start of the next string, in a fashion similar to locating the preamble in a GPS navigation message. The first four strings of the super-frame contain the immediate data. The immediate data is a GLONASS's term for satellite position, velocity, acceleration, and timing corrections needed to compute satellite positions at any time. Figure 3.12 shows the GLONASS message structure.

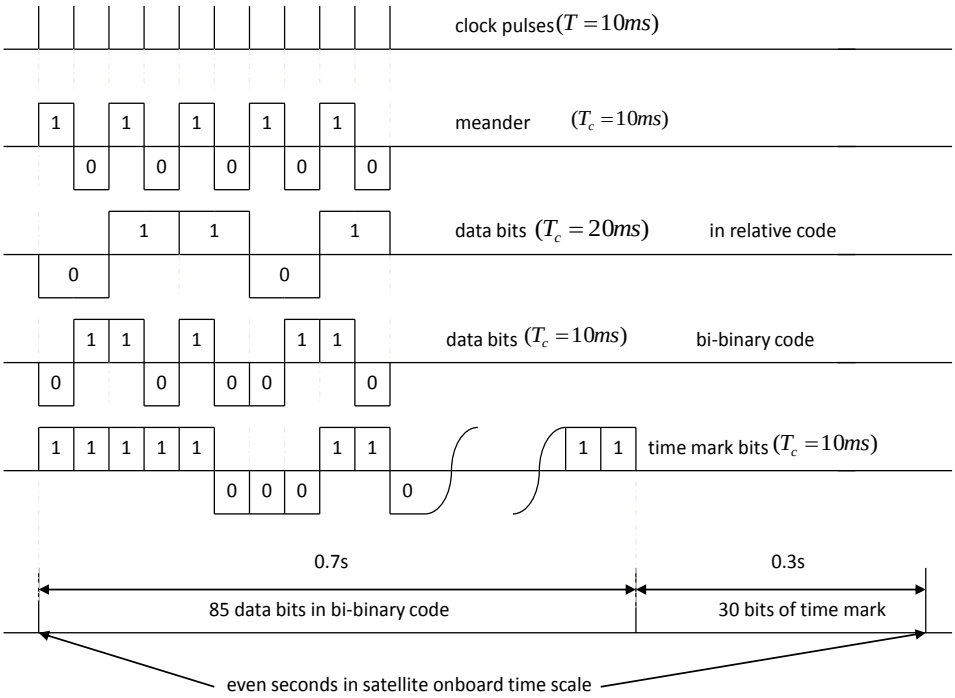

Figure 3.12: Data Sequence Generation

The broadcast navigation message consists of data bits with bit lengths of ten ms. The navigation message is constructed via modulo-2 addition of the true data bit time history with a bit length of 20 ms and the meander code with a bit length of ten ms. The true data bits and the meander code are phase locked so that the resulting navigation message bits have a bit length of ten ms.

3.3.2 Computation of GLONASS Satellite Positions

Computation of the GLONASS satellite positions is a requisite component of receiver's navigation algorithm. The computation of the GLONASS satellite positions is undertaken by using a procedure that relies on numerical integration of the first-order ordinary differen-

tial equations that define the motion of satellites. There are two necessary components for calculating the satellite positions: to set up the initial conditions and to use the numerical technique to solve the differential equations.

The initial conditions are parts of the broadcast GLONASS navigation message. The initial conditions at time t_b include the satellite position at time t_b, the satellite velocity at time t_b, other parameters needed for computing the satellite acceleration at time t_b, the satellite lock offset and a relativistic correction. The satellite acceleration parameters contain perturbations caused by the Earth's gravitational force and the lunar and solar force on the satellite. These initial conditions and parameters along with their units, as defined by the GLONASS ICD, are given in Table 5.1. These initial conditions are defined in the PZ-90 geodetic coordinate system, which is the primary coordinate reference frame used by GLONASS. The initial conditions and parameters are nominally updated every 30 minutes for each satellite by the GLONASS control segment. Once the initial conditions

Table 3.1: Several important parameters in GLONASS message

Description	Symbol	Units
Reference time	t_b	minutes
Relativistic correction	γ_n	dimensionless
Satellite clock offset	$\tau_n(t_b)$	seconds
Satellite position	$x_n(t_b), y_n(t_b), z_n(t_b)$	km
Satellite velocity	$\dot{x}_n(t_b), \dot{y}_n(t_b), \dot{z}_n(t_b)$	km/s
Lunar and solar perturbations	$\ddot{x}_n(t_b), \ddot{y}_n(t_b)$,$\ddot{z}_n(t_b)$	km/s^2

and parameters are obtained via decoding the broadcast navigation message, they are used in conjunction with a set of six first-order ordinary differential equations to achieve the satellite positions for any time. The same set of equations are used to define the motion of each GLONASS satellite. As a result, only the broadcast initial conditions are satellite dependent. The set of differential equations used to compute satellite positions are as follows[GLONASS ICD 2002]:

$$\frac{dx}{dt} = V_x \tag{3.13}$$

$$\frac{dy}{dt} = V_y \tag{3.14}$$

$$\frac{dz}{dt} = V_z \tag{3.15}$$

$$\frac{(dV_x)}{dt} = -\frac{\mu}{r^3}x - \frac{3}{2}J_0^2\frac{(\mu a_e^2)}{r^5}x(1 - \frac{(5z^2)}{r^2}) + \omega^2 x + 2\omega V_y + \ddot{x} \tag{3.16}$$

$$\frac{(dV_y)}{dt} = -\frac{\mu}{r^3}y - \frac{3}{2}J_0^2\frac{(\mu a_e^2)}{r^5}y(1 - \frac{(5z^2)}{r^2}) + \omega^2 y + 2\omega V_x + \ddot{y} \tag{3.17}$$

$$\frac{(dV_z)}{dt} = -\frac{\mu}{r^3}z - \frac{3}{2}J_0^2\frac{(\mu a_e^2)}{r^5}z(3 - \frac{(5z^2)}{r^2}) + \ddot{z} \tag{3.18}$$

$$r = \sqrt{x^2 + y^2 + z^2} \tag{3.19}$$

where μ denotes the gravitational constant, a_e represents the semi-major axis of Earth, J_0^2 is the second zonal harmonic of the geopotential, (x, y, z) describes the initial satellite position at time t_b, ω is the Earth rotation rate, (V_x, V_y, V_z) describes the initial satellite velocity at time t_b, and $(\ddot{x_n}, \ddot{y_n}, \ddot{z_n})$ is the initial satellite acceleration caused by the Earth's gravitational acceleration and lunar and solar perturbations at t_b. It should be noted that the GLONASS ICD Version 5.0 [GLONASS ICD 2002] incorporates two errors in the set of six differential equations. The equations provided here are corrected and are consistent with those found in [Lauri et al., 2008].

Numerical integration is used to solve the six differential equations in order to solve the

satellite position for any desired time. The 4th-order Runge-Kutta numerical integration method has been implemented in the software receiver. The method used to gain confidence in the satellite position calculations is to compare the computed satellite positions with positions from the GLONASS official website, which provides satellite positions for each satellite every 15 minutes. The reason these satellite positions can be used as a comparison to the computed satellite positions is that they are defined at a different time from t_b. The reported satellite positions, which are denoted true positions in Figure 3.13, are defined in GPS reference time.

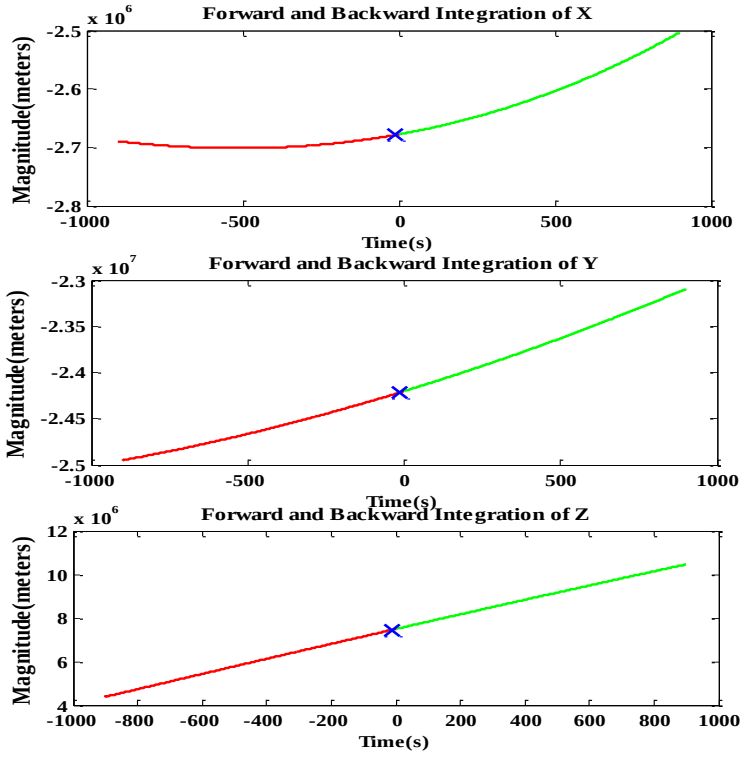

Figure 3.13: Satellite position time histories computed using backward and forward integration of the differential equations using two successive sets of initial conditions separated in time by 30 minutes for one SV

GPS reference time and GLONASS reference time are related by the equation [GLONASS

ICD 2002]:

$$T_{GPS} - T_{GLO} = \Delta T + \tau_{GPS} \tag{3.20}$$

where ΔT is a bias which is 3 hours plus the current number of leap seconds used in GPS to define the time difference between GPS time and UTC, and τ_{GPS} is the fractional offset which is found in the GLONASS navigation message.

The exact satellite position for every functional on-orbit GLONASS satellite is available starting from GPS time equal to zero, at the beginning of the GPS week, with a cadence of 15 minutes. The residual error between the computed satellite position and the true position is 2.94 meters as shown in figure 3.13. Hence, the computed satellite positions are proving to be reasonable and the error is within the stated error budget for the GLONASS satellite position accuracy. This comparison suggests that both the GLONASS satellite parameters in the navigation message are being decoded properly and that the numerical integration technique is performing well.

3.4 A Review of Binary Offset Signal

Galileo is European under developing GNSS. One feature of the Galileo is that it is under civilian control. The Galileo programme has two phases: the In-Orbit Validation (IOV) phase and the Full Operational Capability (FOC) phase. Galileo is inter-operable with the Global Positioning System (GPS) and the GLONASS two other current global satellite navigation systems. The fully deployed Galileo system consist of 30 satellites (27 operational and 3 spares), positioned in three circular Medium Earth Orbit planes at a nominal average orbit semi-major axis of 29601.297 Km, and at an inclination of the orbital planes of 56 degrees with reference to the equatorial plane.

The satellites are controlled and commanded from the Galileo Ground Control Segment (GCS) via its S-Band ground stations. The Galileo Open Service (OS) comprises of signals in the E1 frequency band (centered at the GPS L1 frequency of 1575.42 MHz) and the E5 frequency band (centered at 1191.795 MHz). A recent user receiver test with simulated signals and scenarios (van den Berg et al., 2010) demonstrated a 95% accuracy of 0.8 m (horizontal) and 1.02 m (vertical) for a combination of E1 and E5 signals under specified conditions [Hein et al., 2005].

The Binary Offset Carrier (BOC) signals are the newest flavour of the GNSS signals, which are designed to modernize the military Global Positioning System (GPS) service. The Galileo and the upgraded GPS mostly adopt the BOC signals.The idea of BOC was promoted by John Betz and others from 1999 [Betz 1999, 2001]. For a typical Phase Shift Keying signal, the range code chip wave form is a rectangular pulse

$$P(t) = \begin{cases} 1, & -1/2 \leq t \leq 1/2, \quad (3.21a) \\ 0, & \text{otherwise} \quad (3.21b) \end{cases}$$

where T_C is the chip interval.

The BOC signals simply replace this rectangular pulse with the following waveform:

$$\sum_{m=0}^{M-1} p(\frac{t - mT_S}{T_S}) \quad (3.22)$$

where T_S is the sub carrier symbol interval and $T_S = T_C/M$, . The representation of $BOC(m, n)$ has the following meaning: n is the ranging code (PRN) chipping rate normalized to 1.023Mcps. m is the subcarrier frequency which is also normalized to 1.023Mcps, however, the subcarrier frequency is defined as $1/2T_S$.

As a result, the number of subchips per chip is $M = 2m/n$. For example, BOC(1,1) has a chipping rate and a subcarrier rate of 1.023Mcps, so each chip contains two subchips. BOC

may offer several advantages over the Phase Shift Keying modulation: better jamming and interference resistance, less multipath error, more accurate TOA estimation, and coexist with current signals.

However, there is a noticeable problem in its practical reception caused by multi-peak. The normalized baseband PSD of BOC modulation is given by:

$$S_{BOC_{(fs,fc)}}(f) = \frac{1}{nTs}\left(\frac{\sin(\pi fTs)\sin(\pi fnTs)}{\pi f\cos(\pi fTs)}\right)^2 \quad for\ n = even; \tag{3.23}$$

$$S_{BOC_{(fs,fc)}}(f) = \frac{1}{nTs}\left(\frac{\sin(\pi fTs)\cos(\pi fnTs)}{\pi f\cos(\pi fTs)}\right)^2 \quad for\ n = odd: \tag{3.24}$$

3.5 The Galileo E1 Signal Processing

The Galileo E1-signal (Open Service) comprises of the signal components of E1-B and E1-C and is transmitted in the frequency band 1559 - 1610 MHz allocated to RNSS and ARNS on a worldwide co-primary basis. The signal components of E1-B and E1-C are data-component and pilot component respectively. The E1-signal provides the I/NAV message and supports Safety to Life service. The E1 signal is modulated by a CBOC(6,1,1/11) (Composite Binary Offset Carrier) at f_o and a symbol rate of 250 Sps and multiplexed with scheme shown in figure 3.14. This signal modulates with two different sub carriers: $sc_a = f_o$ and $sc_b = 6f_o$. CBOC linearly combines BOC(1,1) and BOC(6,1) sub-carriers. These sub-carriers, as the balanced sum of two squared-wave sub-carriers, have four different levels [Hein et al., 2005]. The base band E-1 signal is given by:

$$S_{E1}(t) = 1/\sqrt{2}(e_{E1-B}(\alpha sc_a + \beta sc_b) - e_{E1-C}(\alpha sc_a - \beta sc_b)); \tag{3.25}$$

where sub-carrier sc_a is BOC(1,1) modulation and sc_b is BOC(6,1) modulation, $\beta^2 = 10/11$ and $\alpha^2 = 1/11$. Figure 3.14 shows the Multiplexing scheme for E1 CBOC signals.

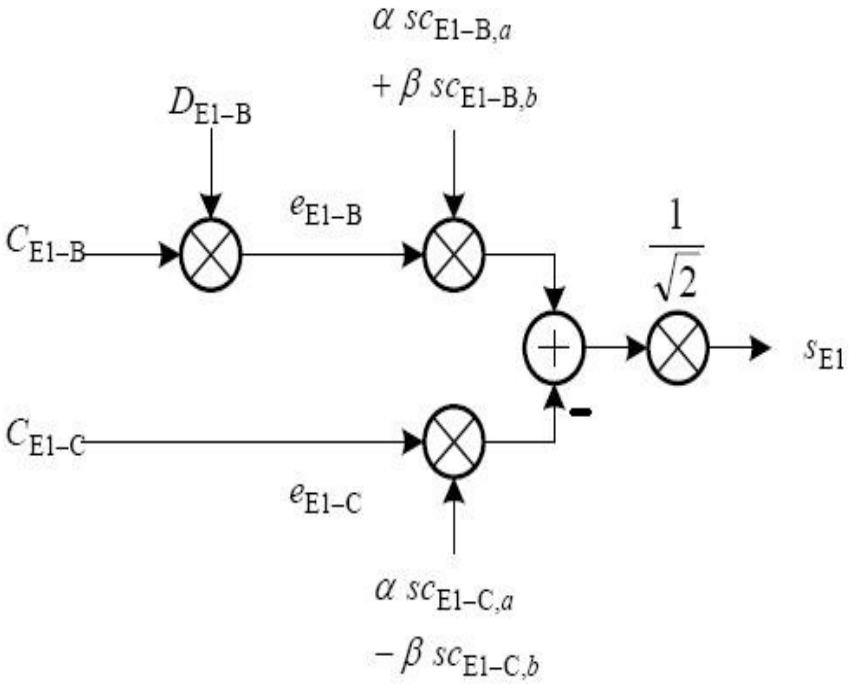

Figure 3.14: Multiplexing scheme for E1 CBOC signal.

The auto-correlation function for the BOC signals differs significantly from those C/A code. Let $R_{BOC}(\tau)$ denote the auto-correlation function for the BOC signal. The expression of $R_{BOC}(\tau)$ can be approximated by [Misra et al., 2006]

$$R_{BOC}(\tau = mT_S) = (-1)^m(\frac{|M-m|}{M}), for\ m = -M, ...M-1, M, \quad (3.26)$$
$$\approx 0\ otherwise$$

Figure 3.15 plots the auto-correlation for BOC(1,1) and BOC(15,2.5). We can clearly observe the multiple peaks corresponding to equation 3.26. The spectrum of the BOC(m,n) signal is centered at $\pm m \times 1.023e^6$ from its nominal center frequency. Figure 3.16 shows

the spectrum of BOC(1,1) signal. The normalized baseband PSD of a BOC modulation is:

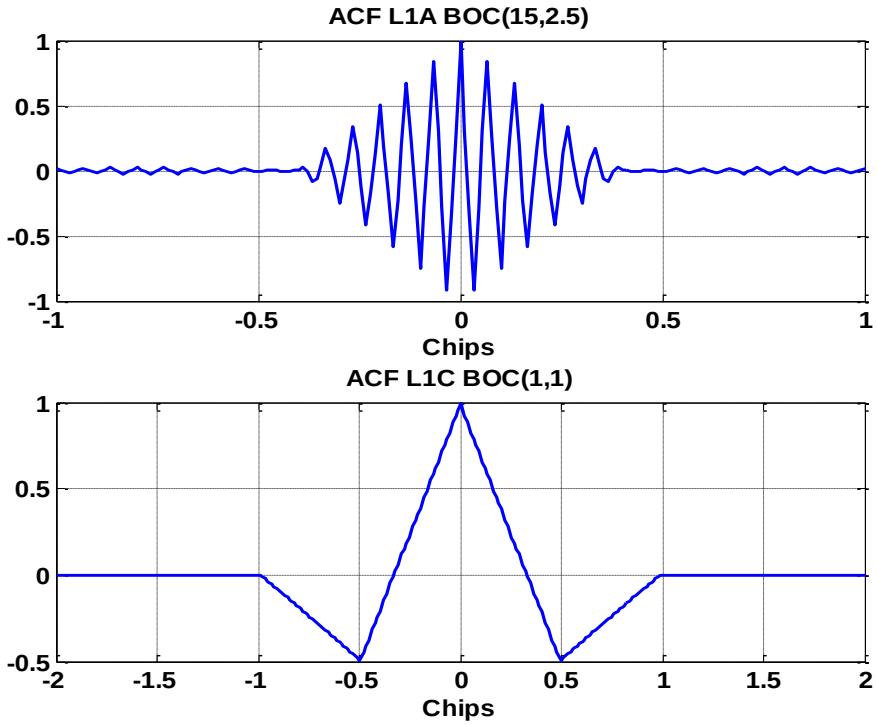

Figure 3.15: Auto-correlation of the E1 CBOC signals.

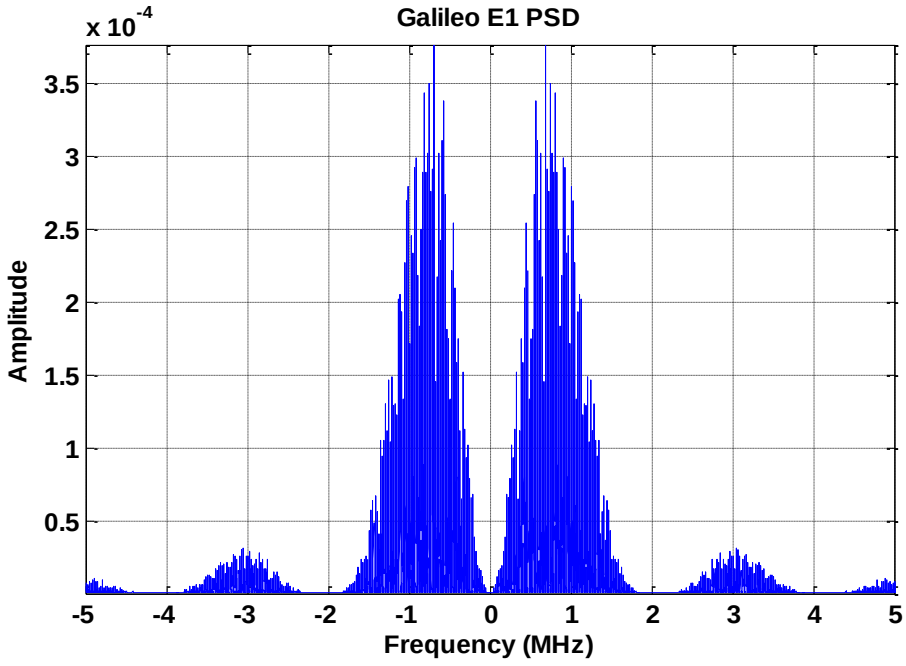

Figure 3.16: Base band Spectrum of the BOC(1,1) signal.

The fundamental principle of the heritage PSK GNSS receiver systems is to cross-correlate each input signal with a matching code, and look for a peak in the resulting correlation function. However, applying the same principle of cross correlation on BOC creates a multi-peaked function as mentioned earlier. The well-known difficulty is that there are secondary peaks onto which a correlating receiver (using a discriminator from early and late gates with feed back through a loop) may easily lock. This problem has been termed false node tracking [Fineet al., 1999]. Figure 3.17 shows the acquisition peaks of a BOC signal (PRN12). We can clearly see the sub-peak in the correlation results.

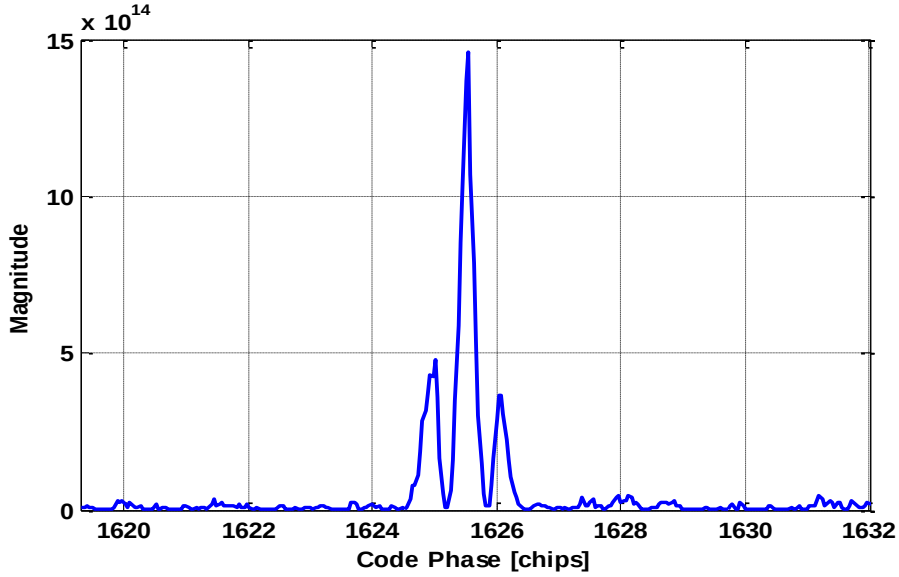

Figure 3.17: Multiple peaks in BOC signal acquisition.

There are several methods proposed to resolve the false node tracking problem. One recently proposed method called bump-jumping method[Fineet al., 1999], where the additional very-early (VE) and very-late (VL) gates are used to monitor the amplitude of adjacent peaks in auto-correlation results. If a comparison with amplitude on the prompt gate

(P) indicates that there is wrongly a higher amplitude on either VE or VL then a condition of false lock is judged to exist and the receiver must make the appropriate jump of either $+T_S$ or T_S towards the correct peak. The bump-jumping method suffers several disadvantages in practical applications.

This method is subject to the fact that the receiver is essentially blind. It must be in a false lock condition before it knows that it is in this condition. The bump-jumping method provides degraded performance for weak signal scenarios as the difference between the main peak and the side peaks is small and is difficult to differentiate. Besides, it can only move one sub-chip step at a time, and also evaluation of relative amplitudes takes time. More practical difficulties, multi-path and all kinds of group delay distortions tend to degrade the essential requirement that the amplitude of the nearest secondary peaks should be significantly less than the amplitude of the main peak. There are other more subtle difficulties [Hodgart al., 2010].

In the paper, a double DLL (or dual DLLs) were used for BOC tracking which automatically realizes the full potential capture range, without losing the potential accuracy of BOC. In this method, a code replica tracks the code component of the signal in a delay locked loop (DLL) while another DLL tracks the sub-carrier component of the signal. Two independent delay estimates are created by the two inter-dependent loops. A local sub-carrier replica is generated to match the incoming signal. After the removal of the sub-carrier, the effective correlation driving the ranging code DLL is exactly the same with PSK-GPS, risk free of false lock. The diagram double DLL tracking loop is provided in figure 3.18 below:

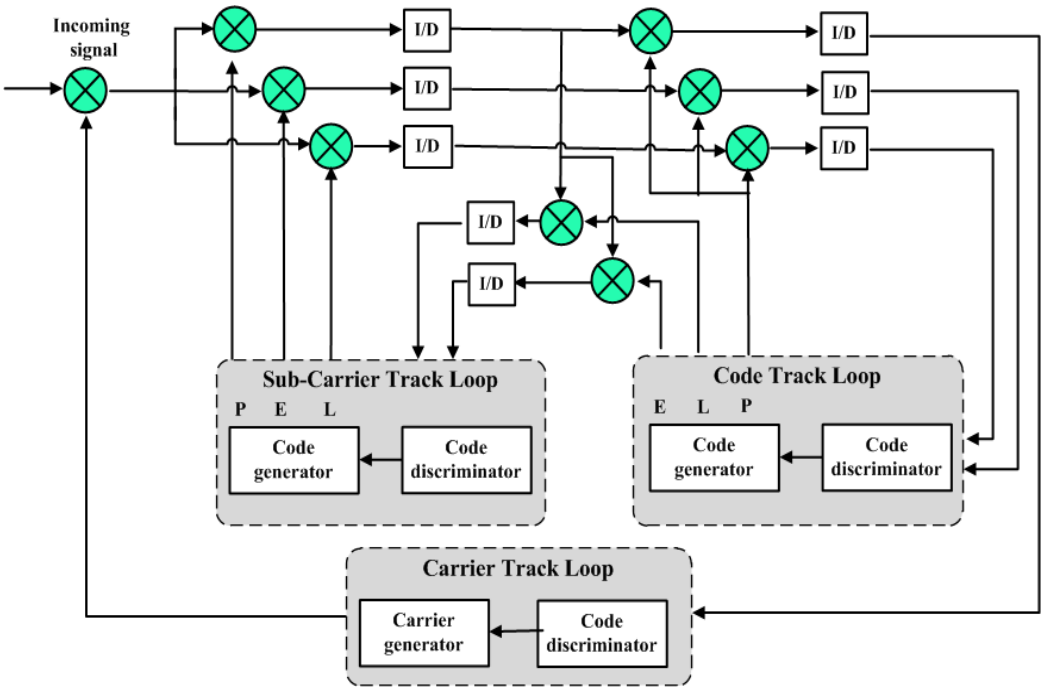

Figure 3.18: Diagram of a double DLL.

The operation of the DLL for sub-carrier (SDLL) is similar to the ranging code except for the chip spacing. Since the sub-carrier is cyclical and with a period equal to one sub-chip width T_S, a reasonable chip spacing of $T_S/2$ is chosen for the DLL. The error signal i.e. discriminator derived from the correlation drives the DLL loop to converge to an independent sub-carrier estimate.

This code phase estimation of the sub-carrier is more accurate than the ranging code estimation but contains ambiguity of nT_S caused by sub peaks in the acquisition results. Fortunately, this error won't have any impacts on the ranging code tracking loop because a separate loop is used. After removal of sub-carrier, the process of the range code is exactly the same with the C/A code. Let the real time delay of the incoming signal be τ,the DLL of the range code estimation to be $\widehat{\tau} \simeq \tau$; the SDLL estimation to be $\tau^{\star} \simeq \tau + nT_S$. At last, the

SDLL estimation can be used to generate an unambiguous single estimation of τ^+ whose accuracy fully exploits the benefit of sub-carrier modulation characteristic of BOC.

$$\tau^+ = \tau^\star + round(\frac{\widehat{\tau} - \tau^\star}{T_S}) \times T_S \tag{3.27}$$

A data set from the Galelio was collected at 2012-6-10, 1:26AM. Figure 3.19 shows the tracking results for this satellite for the E1-B signal. The PRN number of this satellite is number 12.

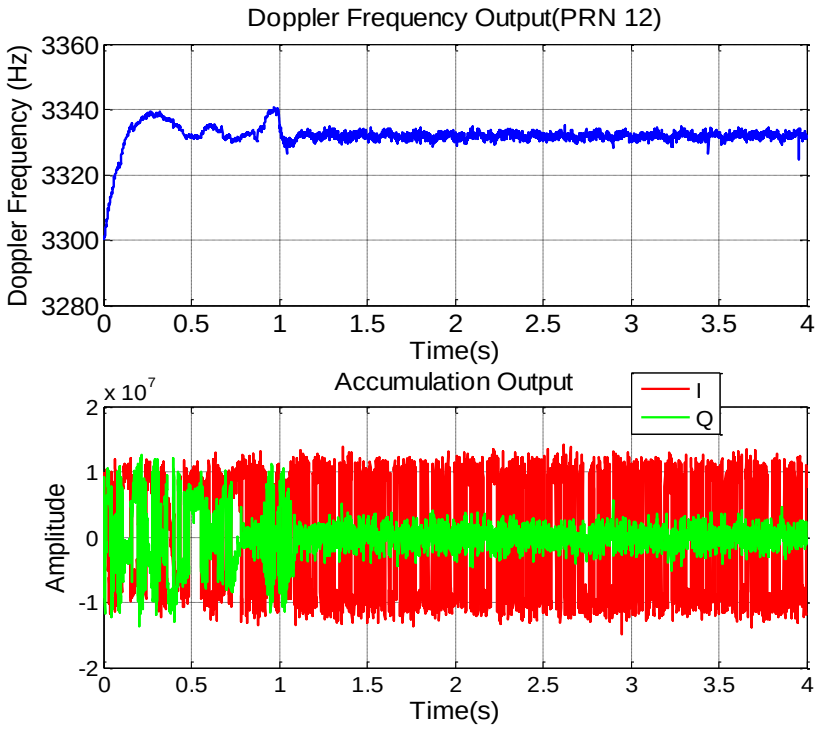

Figure 3.19: Tracking results for E1 CBOC signal.

the properties of BOC(m,n) signal are summarize here:

- the PRN range code rate $f_c = n \times 1.023e^6 cps$;
- sub chip rate per range chip $M = 2m/n$;

- spread of center frequency $\Delta f = m \times 1.023e^6$;
- the total number of sub-peaks of auto-correlation is $2M - 1$;
- the correlation chip width is $1/n$ of range code length;

Chapter 4

GNSS Scintillation Monitoring Setup

4.1 Chapter Overview

Ionosphere scintillations can cause significant phase and/or amplitude fluctuations of GNSS signals, thereby potentially degrading GNSS receiver performance [Datta-Barua et al., 2008; Humphreys et al., 2010a;Pullen et al., 2009]. Improvements of GNSS receiver robustness under these circumstances require a thorough understanding of the scintillations and their impact on GNSS signal propagation.

Commercial GNSS receivers are not designed to handle the combined amplitude fading and phase fluctuations of more severe scintillations. Therefore, these receivers have difficulty generating useful data under strong scintillations. Furthermore, proprietary tracking loop implementations can introduce artifacts in the receiver outputs, making them potentially erroneous indicators of the scintillation parameters. To circumvent these shortcomings, high quality raw RF GNSS scintillation data is needed. This will allow more accurate scintillation signal parameter estimation and characterization, and the development of ro-

bust GNSS receiver algorithms, capable to operate under more challenging scintillation conditions.

In order to accommodate the GNSS ionosphere scintillation research, a high-end GNSS receiver setup has been installed in summer 2009 at the High-Frequency Active Auroral Research Program (HAARP) in Alaska [Pelgrum et al., 2011]. This facility can locally heat-up specific layers of the ionosphere with 3.6 MW of HF radiation controlled by a 180-element phased array antenna. Next to the ability of controlled scintillation experiments by artificial heating, the high-latitude location of the HAARP facility (latitude 62.39^0N, longitude 145.15^0W) places it in the aurora zone, which is known to have frequent natural scintillation events.

The GNSS scintillation monitoring setup has undergone several iterations since its first installation in 2009. Reference [Pelgrum et al., 2011] describes the various iterations and the obtained results over the time frame August 2009 ~ December 2010: The initial Phase-1 installation consisted of a 4 GPS antenna array, 4 NovAtel OEM-V3 L1-L2 GPS receivers, a GPS L1-L2 22 MHz wideband RF data collection system, and a 4 channel GPS-L1 2.2 MHz narrow band RF data collection setup [Gunawardena et al., 2008]. This system was a temporary installation to support the August 2009 HAARP summer student research campaign. In October 2009, the Phase-2 setup was installed at a permanent location. This setup comprises 2 GNSS antennas on a 75m-baseline, connected to two NovAtel OEM-V3 receivers and a 2-channel GPS-L1 narrow band RF data recorder.

The setup was upgraded to Phase-3 to initially support the July 2010 Polar Aeronomy Summer Program (PARS) student campaign and has been maintained as an active data collection and monitoring facility since then. Phase-3 added an additional antenna at a 240m-baseline, a GSV4004B GPS scintillation receiver, and an L1-L2C narrow-band RF

data collection system instead of the 2-channel L1 system of Phase-2. Furthermore, an USRP2-based RF data recorder capable of recording GPS L5 and GLONASS [Peng et al., 2011] was added to the setup. Triggering algorithms based on the output of the GSV4004B enables event-driven RF data recording, resulting in a number of recorded weak to moderate scintillations.

4.2 Scintillation Monitoring System Setup

The GNSS scintillation monitoring setup has evolved four phases since 2008. This Section describes its phase of 2010: Phase-4, and details the update comparing to the Phase-3, which is described in detail in [Pelgrum et al., 2011]. Figure 4.1 shows an aerial view of the HAARP facility and the location of the GNSS monitoring antennas. The GNSS monitoring equipment is situated in a shelter on Science Pad 3. Antennas 1 and 2 are mounted to the corner fence posts of the science pad and form a 75 meter north-south baseline. Antenna 3 is situated 240m west of antenna 1. The new added antenna 4 is mounted on a private residence about 3 miles due South of antenna 1.

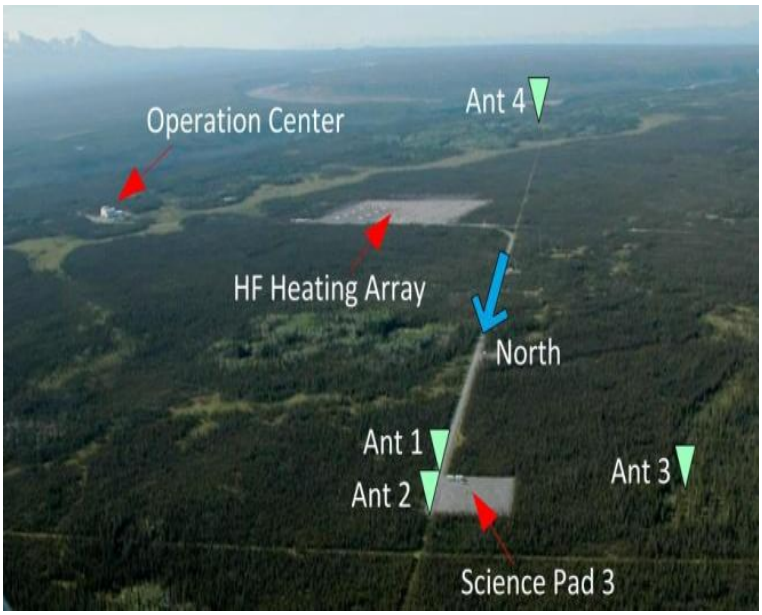

Figure 4.1: Site aerial photograph with the phase-4 GNSS Ionosphere Monitoring setup [Pelgrum et al., 2011].

New to the setup is the Septentrio PolaRxS scintillation receiver which now feeds the triggering algorithm for the event-based data recording [Vikram 2011]. The PolaRxS receiver is capable of simultaneously tracking GPS (L1C/A, L1P(Y), L2P(Y), L2C, L5), GLONASS (L1C/A, L2C/A), Galileo (L1,E6,E5), and SBAS (L1C/A). The PolaRxS receiver provides 100 Hz post-correlator I and Q measurements, which can be used to quantify amplitude scintillations by calculating the S_4 scintillation index. Phase scintillation levels are determined by the $\Delta\phi$ parameter based on the 100 Hz de-trended carrier phase data that is available for all tracked carriers. Currently, the PolaRxS is operated in parallel with the GSV4004 scintillation receiver until the setup and associated algorithms have been proven robust. The phase-4 GNSS Ionosphere Monitoring setup is shown in figure 4.2[Pelgrum et al., 2011]. Except for scintillation monitoring, the PolaRxS is also used to monitor the spectrum for potential interference.

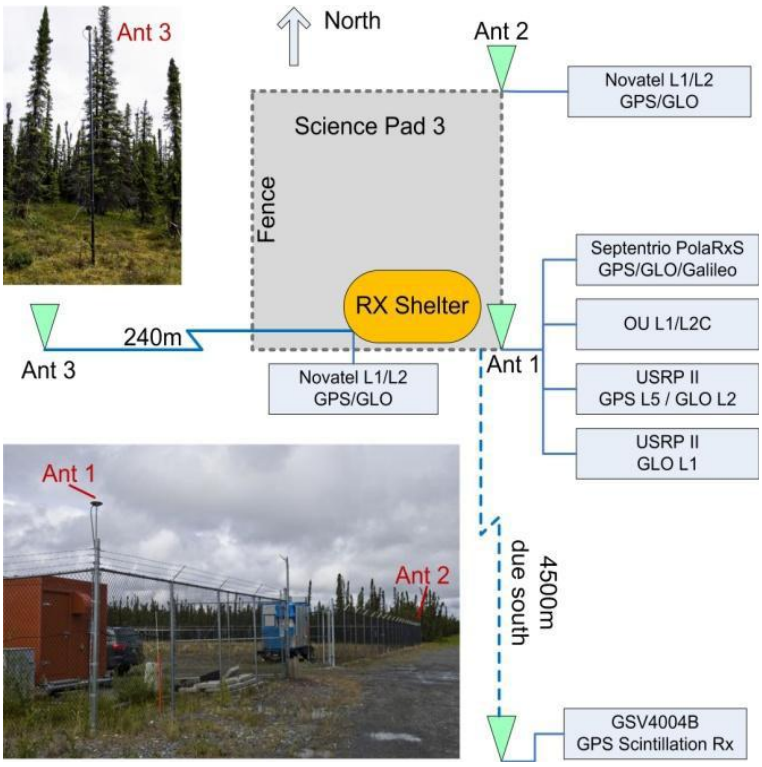

Figure 4.2: Phase 4 Data Collection System Layout - operational since July 2011 HAARP heating experimental campaign [Pelgrum et al., 2011].

High quality raw RF GNSS scintillation data recording is essential for accurate scintillation signal parameter estimation and characterization, and the development of robust GNSS receiver algorithms. In the Phase-4 setup, multi-constellation and multi-band GNSS RF data recordings are facilitated by four separate systems. First, L1 and L2C RF signals are recorded by a 16-bit narrow-band (5 MHz) data collection setup, custom built by Ohio University [Gunawardena et al., 2008].

Next, GPS L5 or GLONASS L2 are recorded by a re-configurable USRP2 software-defined radio front end. By default, this system is configured for GLONASS L2 but is automatically switched to an L5 configuration in the event of a scintillation trigger by an L5-equipped GPS satellite.

New to Phase-4 is the GLONASS L1 RF recording using a second USRP2 system. With the addition of the PolaRxS scintillation receiver and the second USRP2, the GNSS monitoring capabilities of the Phase-4 setup have been significantly enhanced. Finally, a location has been surveyed for a fourth GNSS antenna. The chosen location is about 3 miles due south from the other antennas. This provides an extended baseline which will facilitate in the tomography analysis of the ionosphere disturbances. The GSV4004B scintillation receiver will be connected to antenna 4 in next campaign.

4.3 GLONASS Data Collection

With the addition of the second USRP2 front end and the Septentrio PolaRxS multi-constellation scintillation receiver, the Phase-4 setup now has full GLONASS monitoring and event-driven RF recording capabilities. The addition of GLONASS is a significant enhancement to the overall monitoring potential. First, the total number of GNSS satellites is doubled. Furthermore, the GLONASS constellation has the benefit of a higher inclination compared to GPS (64.8^0 inclination for GLONASS versus 55^0 for GPS). As shown in Figure 4.3 [Wang et al., 2011], this higher inclination provides better coverage just north of local magnetic zenith (MZ), which is an area of great interest for ionosphere scintillation research.

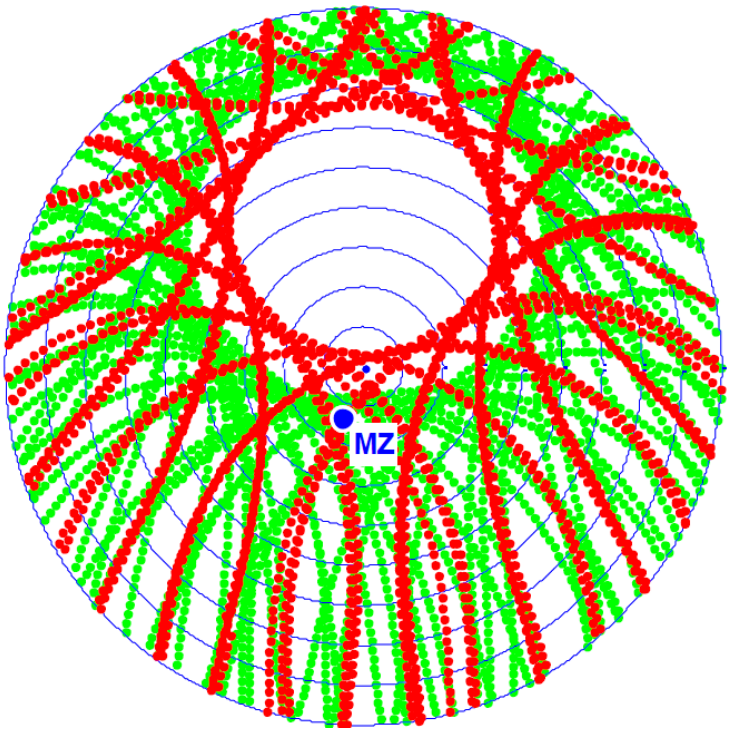

Figure 4.3: Sky plot of GPS (green) and GLONASS (red) tracks (24 hours, October 5, 2010) [Pelgrum et al., 2011].

4.4 Automatic Event Monitoring and Triggering

Long-duration continuous RF data recording is cumbersome because of the high data rates involved. For example, the L1-L2C narrow-band (5 MHz) RF data collection setup discussed earlier in this paper samples 2 channels at 5 MS/s, with a 16 bit resolution. This results in a data rate of 80 MB/s. Such high data rates overwhelm storage and post-processing capability for data collections of extensive periods of time. Since controlled heating experiments are relative short in duration (hours at most) and at known times, manual control of the RF recordings is feasible. Natural scintillations, however, are relatively short lasting as

well, and spatially and temporally sporadic phenomena. In order to capture natural scintillations, an event-driven data collection system is needed, see figure 4.4 [Pelgrum et al., 2011].

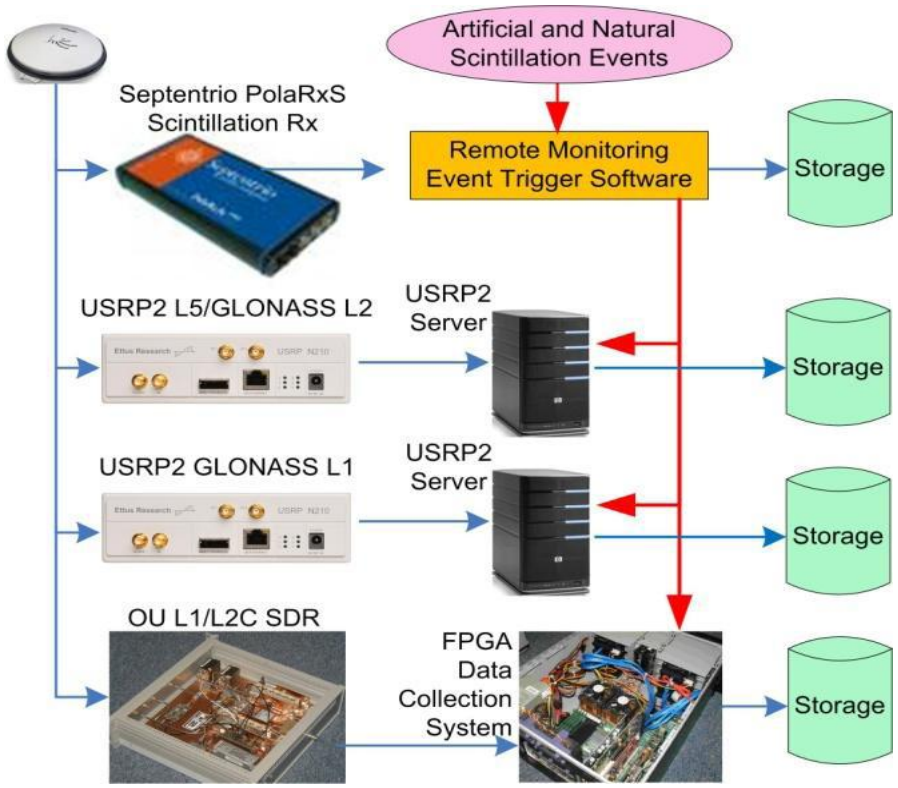

Figure 4.4: Event-Driven GNSS multi-band multi-constellation RF recording [Pelgrum et al., 2011].

In August 2010, an triggering algorithm was developed based on the statistics of a couple of days of recorded receiver data. The resulting algorithm only monitored potential amplitude scintillations by observing S_4, and an S_4 trigger threshold based on signal C/N_0 is calculated. To prevent a high false alarm rate due to multi-path, the threshold was chosen rather conservatively [Vikram 2011]. Numerous natural scintillations have been detected and analyzed in next chapter, but many more potentially interesting events remained unnoticed

due to the limited observability (only S_4, no $\Delta\phi$) and the conservatism of the algorithm.

Recent efforts [Vikram 2011] have led to an improved triggering algorithm. This algorithm observes both the S_4 (derived from the GSV4004B 50Hz Signal Intensity or the PolaRxS 100 Hz IQ data) and the $\Delta\phi$ (derived from the GSV4004B 50 Hz or the PolaRxS 100 Hz carrier phase data.) A major challenge, especially for the signal strength-based trigger (S_4), is the difficulty in separating the effects of true ionosphere scintillations from that of the environment multi-path. The trigger design presented in [Vikram 2011] utilizes a sky map of S_4 index and $\Delta\phi$ distributions for the satellites based on an extensive set of data collected by a commercial receiver at the receiver site. The sky map is divided into grid cells, with threshold values for each grid cell based on the distributions of nominal (non-scintillation) data collected at that elevation and azimuth. This sky map will be updated automatically on a regular basis.

4.5 Transform-domain Instrumentation GPS Receiver (TRIGR) front end

Scintillation research capabilities are maximized when using data from instrumentation grade GNSS RF front-ends. In summary, an instrumentation grade RF front-end is characterized by the following attributes. A detailed description can be found in [Peng et al., 2011]: High dynamic range: the front-end should support the ability to capture strong in-band signals (i.e. interference and jamming) with high fidelity and without AGC, maximizing options for follow-on processing. Wide bandwidth: Ideally the front-end should have the same bandwidth as the broadcast signal (i.e. 24 MHz for GPS). At a minimum,

it should be able to process all signal modulations, i.e. C/A code, L2-C, P(Y) and L5-code. Hence, it should support at least a 20 MHz bandwidth. Exceptionally good reference clocks and low phase noise oscillators help to provide carrier phase tracking residuals that are close to the thermal noise.

Figure 4.5 shows the block diagram and frequency plan of the 4-channel front-end. The front-end follows the same overall frequency plan that was used in WBDFFE [Gunawardena et al., 2008]. Specifically, the RF signal is down-converted to a first IF of 70 MHz and then band-pass sampled at 56.32 MHz to yield base-band samples with a center frequency (digital IF) of 13.68 MHz. In order to use readily available IF filters and to simplify the signal processing of the sampled signals, the front-end uses the same down conversion and sampling plan for all GPS frequencies. The overall noise figure of the TRIGR front end is around 4dB, and a highly stable OCXO ($\leq 0.001 ppm$) is used as common reference for all four channels [Gunawardena et al., 2008]. The TRIGR also provide a flexible data bit length of 1,2,4 and 8 options.

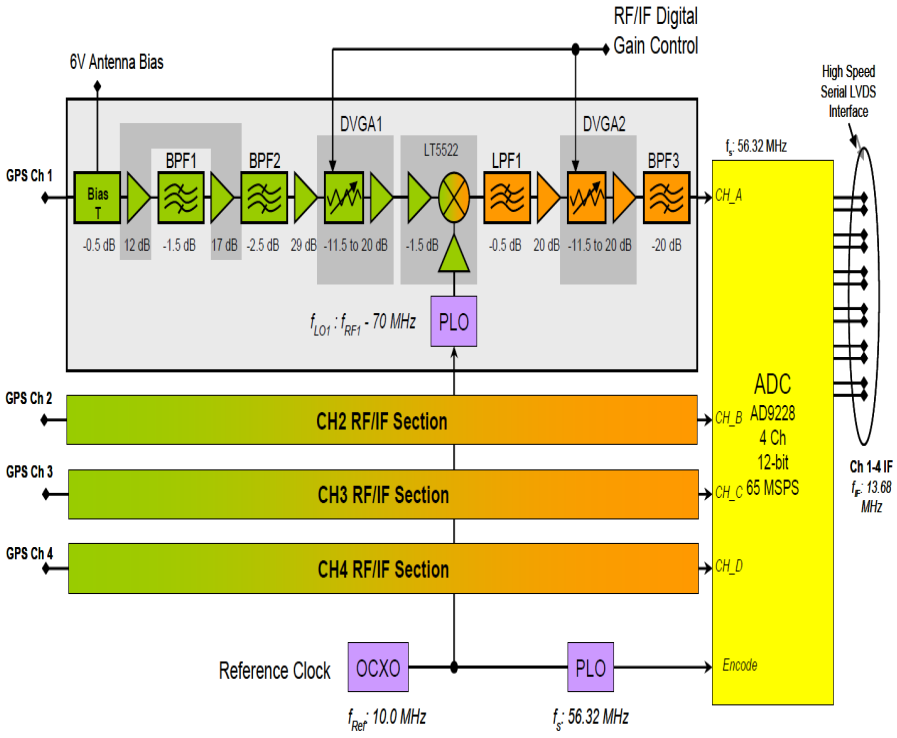

Figure 4.5: Block diagram and frequency plan of the 4-channel TRIGR front-end.

Chapter 5

The USRP2 Front End Performance Evaluation

5.1 Chapter Overview

A typical Global Navigation Satellite Systems (GNSS) receiver is composed of three major functional components: radio frequency (RF) front end, receiver signal processing, and navigation signal processing. The RF front end filters and amplifies the input RF signal and down-converts it to an intermediate frequency (IF) before an analog-to-digital converter (ADC) samples the signal for further processing. The RF front end is traditionally implemented in analog circuits. The receiver signal processing unit demodulates the signal to extract range and carrier phase measurements and navigation data messages which will be combined in the navigation signal processing stage to generate position, velocity, and timing solutions. A software-based GNSS receiver performs the demodulation function through software implementations on general purpose processors or FPGAs, while

the traditional hardware-based receiver processing implements its functions on application specifics integrated circuits (ASIC). Compared to the hardware-based receivers, a software-based receiver offers more flexibility and allows more complicated algorithm implementations. As a result, software-defined GNSS receivers have gained much attention from both research and development communities in recent years [Akos 1997; Tsui 2004]. The focus is the realization and performance evaluation of a flexible GNSS receiver RF front end using a general purpose universal software radio peripheral (USRP) device for ionosphere scintillation data collection [Peng et al., 2011].

USRP is a low IF architecture radio designed to allow general purpose computers or digital signal processors (DSP) to function as high bandwidth communication devices. In recent years, the low IF architecture has gained much attention due to the demand for integratable and flexible wide-band low-cost receiver platforms that enables developers to build a wide range of communication systems with minimum cost and effort. With a maximum sampling frequency of 50MHz and operating frequencies ranging from DC to 5.9GHz, a properly configured USRP2 is capable of capturing all L band GNSS signals. Additionally, the device is equipped with a flexible data and control interface through a gigabit Ethernet port, making it ideal for field data collection and remote monitoring applications.

The USRP2-based GNSS RF front end is a very attractive option as we enter a new era of satellite-based navigation with the recent GPS modernization that includes L2C, L5, and the planned L1C signals [Braschak et al. 2010], the increasing number of Russians GLONASS satellites and reformed signals [Revnivykh et al. 2010], the emergence of Europeans Galileo [Hein et al. 2005] and Chinas Compass constellations [Cao et al. 2008], and a multitude of regional and spaced-based augmentation systems. The multi-constellation systems offer diverse signal structures over a wide span of frequencies and improve the

spatial coverage at nearly every geographical location on the surface and in the near space of the Earth. In addition to enhanced continuity, availability, and integrity of navigation and timing solutions, the system will enable unprecedented scientific research of the dynamic atmosphere on a global scale.

The USRP2-based software receiver presented is for the latter purpose. Specifically, we aim to establish an array of GNSS receivers at locations where GNSS signals traversing the ionosphere frequently experience scintillation. Existing deployment of ionosphere scintillation monitoring systems are limited to single frequency GPS receivers or at most dual frequency GPS receivers operating at the L1 and L2 bands [Groves et al. 2000; van Dierendonck et al. 1993; van Dierendonck et al. 2004; Skone et al. 2008; O Hanlon et al. 2011]. The USRP2-based software receiver offers many advantages over these systems. First, GPS satellites have limited coverage at the high latitude regions where scintillations frequently occur. GNSS satellites such as those in the GLONASS offer more high latitude coverage and can be used to fill the GPS void [Wang et al. 2011]. Second, the sheer number of combined satellites in all available constellations will increase the spatial resolution of the ionosphere tomography derived from a fixed size ground-based GNSS receiver array. Third, no field study has been conducted on the effect of ionosphere scintillation on the new GPS L5, GLONASS, Galileo, and Compass satellite signals. There is an urgent need to gain an understanding of the spatial correlation among the satellites and the frequency correlation among different signals under ionosphere scintillations [Seo et al. 2009; Seo et al. 2011; El-Arini et al. 2009]. The USRP2 offers a flexible and re-configurable platform for these studies. In our first phase of investigation, we have successfully developed and implemented software that controls the data collection system [Peng et al. 2010]. A user can specify the USRP2 front end center frequency, receiver sampling frequency, and output

data format through a software user interface. A First In First Out (FIFO) buffer is allocated to store the incoming IF data. The data collection system and control software have been successfully tested and collected GPS L1, L2, and L5 and GLONASS L1 and L2 signals [Peng et al. 2010].

5.2 RF Front End Architecture

5.2.1 The Superheterodyne Receiver

The superheterodyne receiver is a popular receiver design architecture because of its high selectivity and sensitivity. Figure 5.1 shows a typical one-stage superheterodyne receiver signal processing block diagram. The incoming signal is first filtered by a channel selective band pass filter (BPF1), amplified by a low noise amplifier (LNA), and then further filtered by an image rejection filter (BPF2). The resulting signal is down converted to intermediate frequency (IF) by mixing with the output of a local oscillator (LO). A third band pass filter (BPF3) or a low pass filter is used to remove the high frequency portion of the mixer outputs. The combined processes as described above comprise a single stage of a superheterodyne receiver. Multiple stages maybe used to step the input signal from a high RF frequency to a low IF frequency. At the very last stage, the filtered outputs are sampled by an analog-to-digital (ADC) converter for further digital receiver signal processing.

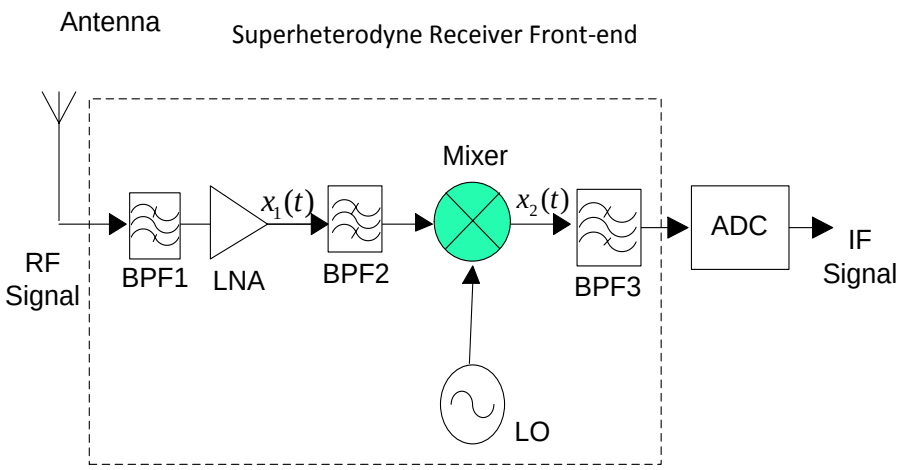

Figure 5.1: Block diagram of a one-stage superheterodyne receiver front end.

The image rejection filter (BPF2) plays a key role in the superheterodyne receiver. Figure 5.2 illustrates the effect of image rejection filter on the signal spectrum. Assuming the incoming signal of at the BPF2 can be modeled as:

$$x_1(t) = S(t)cos((\omega_{IF} + \omega_{LO})t) + I(t)cos((\omega_{IF} - \omega_{Lo})t) + N(t) \tag{5.1}$$

where $f_{RF} = f_{IF} - f_{LO}$ is the center frequency of the incoming signal, f_{LO} is the local oscillator frequency, $S(t)cos((\omega_{IF} + \omega_{Lo})t)$ is the incoming signal, $N(t)$ is the noise. We also assumed that there is an interference source $I(t)cos((\omega_{IF} - \omega_{Lo})t)$. The interference source is located at the mirror frequency of the input signal with the mirror located at ω_{LO} as shown in figure 5.2. For such mirror interference, the mixing operation down converts the signal and the interference spectrum to the same IF frequency:

$$\begin{aligned} x_2(t) = x_1(1)cos((\omega_{LO})t) = \frac{1}{2}[S(t) + I(t)]cos((\omega_{IF})t) \\ + \frac{1}{2}[S(t)cos((2\omega_{LO} + \omega_{IF})t) + I(t)cos((2\omega_{LO} - \omega_{IF})t)] + N(t)cos((\omega_{LO})t) \end{aligned} \tag{5.2}$$

In order to make sure the interference does not overlap with the input signal spectrum at the output of the mixer, BPF2 must be used to suppress the interference before the signal enters the mixer.

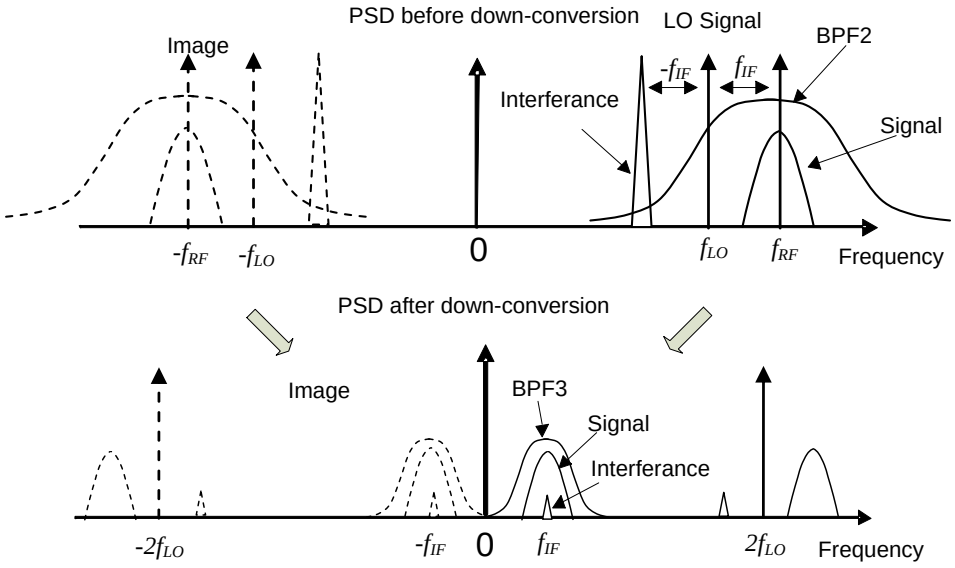

Figure 5.2: Illustration of mixing operation on signal and its mirror image interference spectrum folding.

The second term in equation 5.2 includes high frequency components which can be eliminated by the channel selective filter BPF3. The choice of BPF3 is a trade off between the image rejection and the adjacent channel selection. For a given Q factor of BPF2, if the IF is relatively high, the interference will be effectively suppressed as its spectrum may be far away from the wanted signal. However, larger IF means more costly design for the BPF3. If a low IF is used, then the BPF3 bandwidth can be reduced. More out-of-band interference can be rejected by BPF3. On the other hand, the mirror interference will be lo-

cated closer to the f_{LO} and filtering by BPF2 will be less effective. As a result, more mirror interference will be folded over the signal spectrum after the mixing. One solution for this problem is to use multiple down-conversion stages with succeeding decreasing f_{IF} values. At the first stage, a large f_{IF} value will lead to effective suppressing of potential mirror interference. Succeeding stages with smaller f_{IF} can be implemented with narrower BPF2 and BPF3 bandwidth, further reducing in-band interference and noise. Typical multi-stage low-IF receiver consists of 3 stages [Razavi 1997]. The disadvantages of the superheterodyne implementation are the increased cost, RF front end size, and power consumption. Another important drawback of the superheterodyne receiver is that the image rejection filter is too complicated and impractical to be implemented by an integrated circuit (IC). The normal solution is to use a bulky and expensive surface acoustic wave (SAW) filter [Abidi,1995].

5.2.2 Direct Complex Down-Conversion Architecture

In the direct complex down-conversion architecture, the signal is directly down converted to zero base-band frequency as show in figure 5.3.

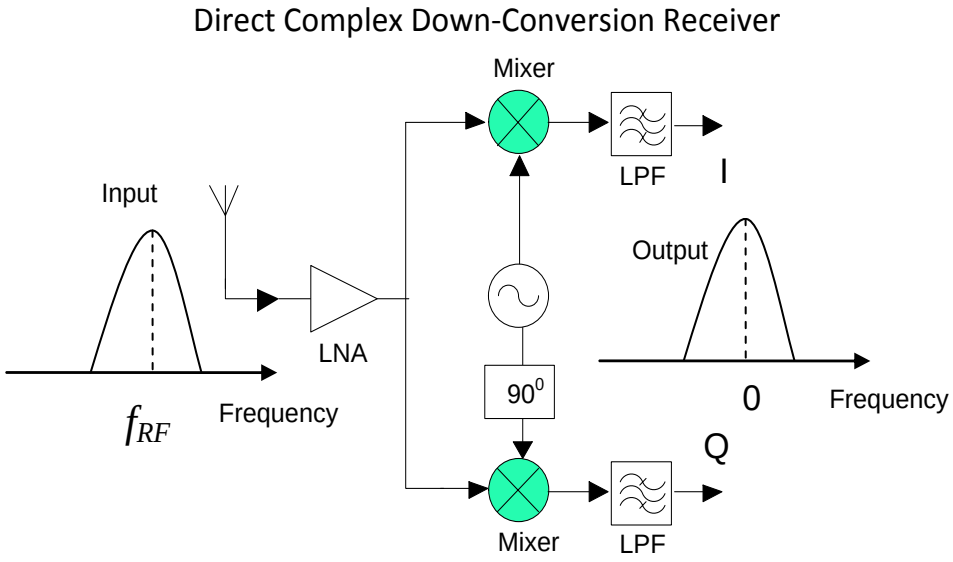

Figure 5.3: Direct complex down-conversion architecture.

The low pass filters suppress the out-of-band noise and the high frequency components of the mixer outputs. Since the in-phase and quadrature components are orthogonal to each other, we use complex signal processing to describe the direct complex down-conversion. Let the incoming signal be $x(t)$ and the output of the complex mixer be $y(t)$, and the local oscillator frequency is f_{RF}:

$$y(t) = x(t)e^{j\omega_{RF}t} \tag{5.3}$$

$$Y(\omega) = X(\omega - \omega_{RF}) \tag{5.4}$$

Where, $X(\omega)$ and $Y(\omega)$ are the frequency domain representation of $x(t)$ and $y(t)$. Unlike the real down-conversion in the superheterodyne receiver architecture described in the previous sub-section where the signal spectrum shifts towards both high and low frequencies, the complex mixer shift the incoming signal spectrum in one direction only as shown in figure 5.4. There is no image folding occurring. The LPF can easily reject the down-converted interference. No image rejection filter is needed. The expensive SAW filter used

in the superheterodyne architecture is replaced by a low cost LPF which can provide better integration.

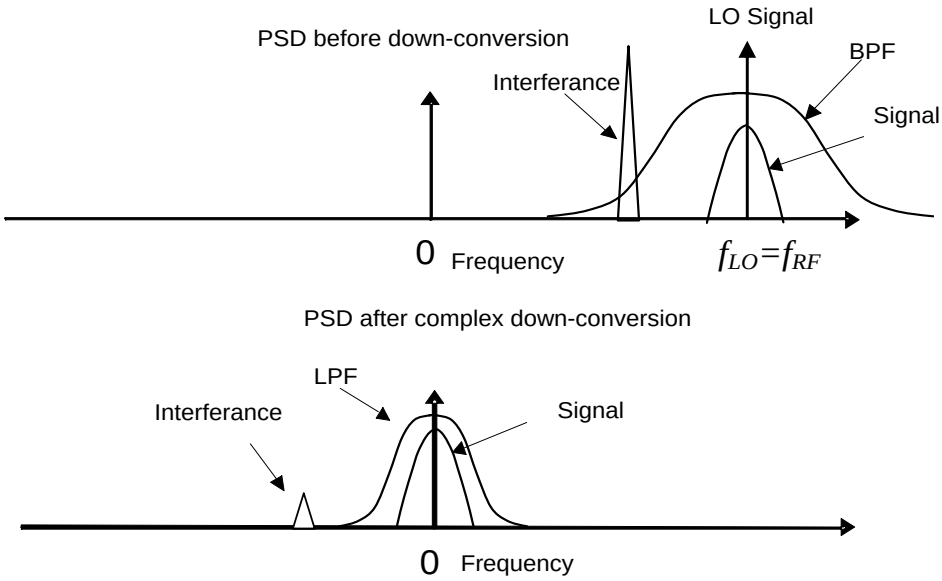

Figure 5.4: Image rejetion of the direct complex down-conversion architecture.

Although the direct complex down-conversion architecture is superior to the superheterodyne architecture in image rejection, but it suffers several drawbacks such as DC offset, I/Q mismatch, even order distortion etc [Razavi 1997]. Among these issues, the DC offset is the most serious one because it may lead to saturation of the subsequent circuits. Figure 5.5 shows the three main sources of the DC offset, all of them are results of leakage from the LO itself. The first source is due to the leakage from circuit components between the antenna and the mixer. The signal reflected from these circuit component will enter the mixer itself, leading to self-mixing as shown in path A. The second source is contribution from the antenna. In the direct complex down-conversion scheme, the LO has the same center frequency as the incoming signal. When any LO leakage reached the antenna, the antenna pass-band will allow the leakage to pass back to the circuit and the returned leak-

age will be further amplified by the LNA as shown in path B. The third source includes the LO leakage of the circuit to the environment. Reflection by all other potential objects in the environment may be intercepted by the antenna and feedback to the circuit as shown in path C. This scenario is similar to that of multipath effects [Abidi 1995]. Methods have been developed to improve performance by lowering the DC offset to an acceptable level [Yoshida et al., 2008;Sampei et al., 1997]. For example, [Yoshida et al., 2008] developed a feedback loop to decrease the DC offset digitally. This method, however, increases the complexity of the circuit and may cause other problems when the DC offset is not constant [Sampei et al., 1997].

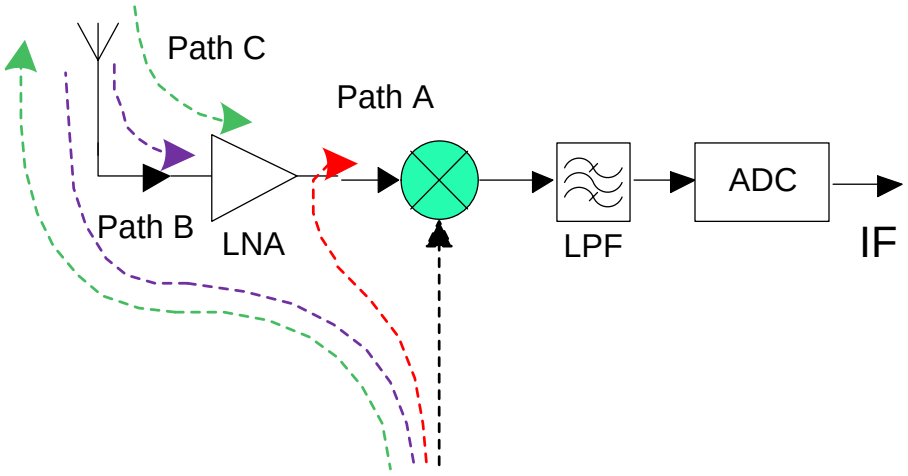

Figure 5.5: Self mixing of the local oscillator.

5.2.3 Low IF Receiver

The low IF receiver combines the advantages of the direct complex down-conversion receiver and the superheterodyne receiver. A typical low IF receiver has two stages as shown

in figure 5.6. The first stage is the traditional complex mixer similar to that of the complex direct down-conversion scheme. It translates the RF signal to a low IF which is less than half of ADC sampling frequency. The BPFs after the mixer are centered at the IF to filter out unwanted signals. The second stage is used to further down covert the low IF signal to zero center frequency in the digital domain and suppresses the image interference. Similar to the complex direct down-conversion, filtering of the unwanted interferes can be implemented at a low IF frequency. As a result, the structures of the filter components are simplified. In the mean time, the signal is down-converted to low IF instead of zero frequency as in the direct down-conversion receiver, so the problem of DC offset is avoided in the low IF receiver. This architecture, however, still suffers the I/Q mismatch problem and extra computation is demanded in the digital complex mixer [Crols et al., 1998]. The performance of the low IF receiver is still not as good as that of the superheterodyne receiver, but the high flexibility, high integration rate, and low cost RF systems make it an attractive option in research communities [Crols et al., 1995, Rudell et al., 1997].

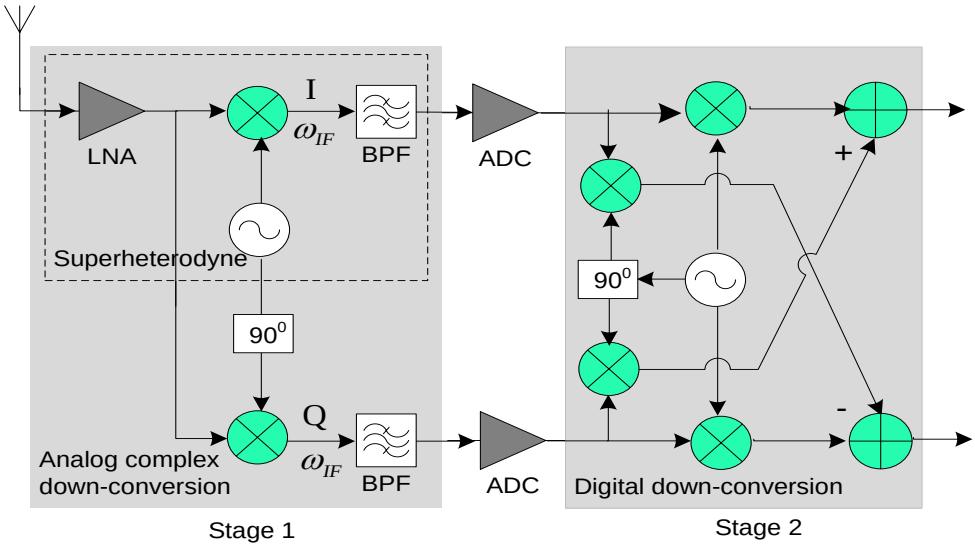

Figure 5.6: The low IF receiver architecture.

5.3 USRP2 RF Front End

The RF front end used in this software receiver system is the second generation of Universal Software Radio Peripheral (USRP) which is developed based on the low IF architecture. The USRP functions as a hardware radio platform that provides RF signal reception and conditioning over a broad range of radio frequencies. Additionally, it also allows developers to implement and test software radio systems at a low price. The latest product USRP2 offers higher speed and better performance as well as increased flexibility compare to the first generation USRP [Peng et al., 2012]. At the heart of the USRP2 is a FPGA which allows for processing of complex waveforms at high sampling rates. The USRP2 is also equipped with high speed and high precision ADCs and DACs for wide band signal processing and conditioning. With a maximum sampling frequency of 25MHz for both in-phase and quadrature components and a gigabit Ethernet interface, the USRP2 is suitable for collecting raw data for wide band GNSS signals. A Multiple-Input-Multiple-Output (MIMO) system can be built by synchronizing several USRP2 boards with a common pulse per second (PPS) timing control. The Universal Hardware Driver (UHD) which is supported on both Linux and Windows operating systems shall become the official driver for the USRP2. Currently,the GNU Radio is still the most popular software for the USRP family. For this project, both UHD and GNU Radio were successfully installed and working properly on the Ubuntu 10.4 Linux operating system. Table 5.1 highlights some comparisons between the USRP2 and USRP.

Several daughter boards are available to perform signal conditioning and tuning of the

Table 5.1: Key components for USRP2 and USRP.

Component	USRP2	USRP
RF Range	0~5.9GHz	
FPGA	Altera Cyclone	Xilinx Spartan-3 XC3S
DACs	Two 400MS/s 16-bit	Four 128 MS/s 14-bit
ADCs	Two 100MS/s 14-bit	Four 64MS/s 12-bit
Max Sampling Freq.	50MHz	16MHz
PC Connection	Gigabit Ethernet	USB 2.0

Table 5.2: Daughter boards for GNSS receivers

Name	Type	Freq.Range (GHz)	IF BW(MHz)
DBSRX	RX	0.8-2.4	4-33
RFX1200	TX/RX	1.15-1.4	20
RFX1800	TX/RX	1.5-2.1	20
WBX	TX/RX	0.05-2.2	40

RF inputs to a desired base-band frequency before the processed signal is fed to the USRP2 motherboard. With appropriately selected daughter boards, the USRP2 is capable of processing signals from DC to 5.9GHz. Table 5.2 lists the available daughter boards that can be used for satellite navigation signal processing. The DBSRX covers the full range of the L band navigation signals. It also provides an adjustable RF bandwidth between 4 and 33MHz, thus making it suitable for processing both the narrow band GPS L1 and

L2C signals and the new wide-band GPS L5 signals. The RFX1200 covers the L2 and L5 band, while RFX1800 covers the L1 band. The schematics of the all daughter boards and the USRP2 main board are available from the Ettus website. It should be noted that the DBSRX daughter board need to be modified before it can work properly with the USRP2 [Peng et al., 2011].

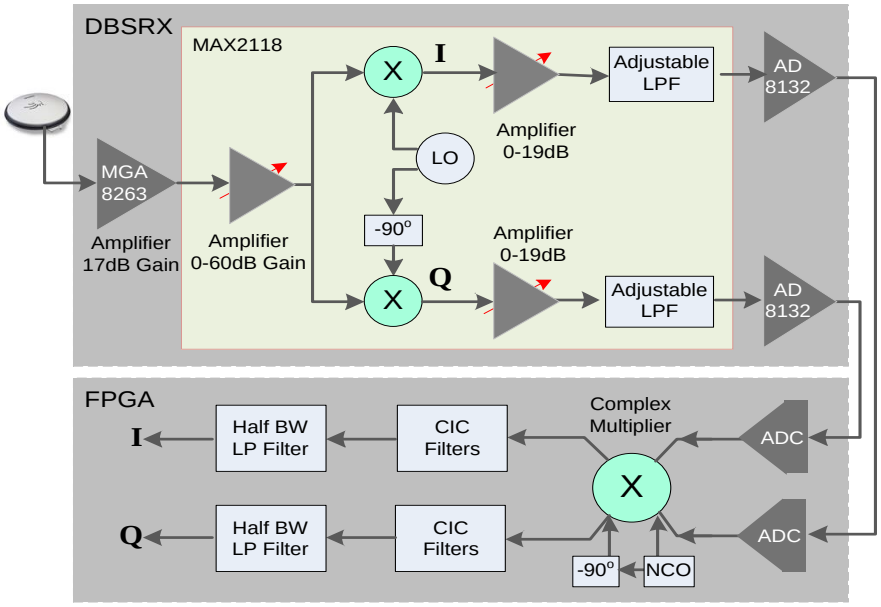

Figure 5.7: GNSS signal path schematics on the RF front end circuit.

Figure 5.7 shows the RF front end setup by using the DBSRX daughter board as an example. A GPS-703-GGG triple frequency antenna manufactured by NovAtel allows for combined GPS L1, L2, L5, GLONASS, and Galileo signal reception. The antenna is connected to the DBSRX daughter board through a SMA connector. The DBSRX consists of three major components: the MGA8263 amplifier, the MAX2118 chip, and the AD8132 chip. The analog signals from the antenna are first amplified by the MGA8263 wideband amplifier with a 17dB fixed gain. The MAX2118 which provides an operational frequency range between 925MHz and 2175MHz [Peng et al., 2012] converts the incoming L-band

signals to low IF or baseband using a broadband I/Q down converter. The I and Q channel each include a linear amplifier with variable gain control, a down conversion mixer, and a low pass filter with both gain and cutoff frequency controls. The RF and baseband variable gain amplifiers together provide 79dB flexible gain control range. The low pass filters have adjustable bandwidth between 4 to 33MHz.

The RFX boards have similar block diagrams as that of the DBSRX. The main difference is that the MAX2118 in the DBSRX is replaced with the AD8347 chip from ANALOG DEVICES in the RFX boards. The AD8347 chip performs similar signal processing tasks as that of the MAX2118. The AD8347 has a maximum noise figure of 11dB while the MAX2118 noise figure is between 10 to 11.5dB, depending on the environment temperature. Both AD8347 and MAX2118 provide adjustable pass band bandwidth. The AD8347 is driven by an external oscillator while the MAX2118 has an integrated local oscillator.

The filtered signals are further amplified by the AD8132 differential amplifier before being digitized by the high speed ADCs at $100 Msamples/s$ on the USRP2 main board. The center part of the USRP2 board is the FPGA which performs the high sampling rate data processing. The standard FPGA configuration in the receiver signal path includes complex mixing which down converts the baseband signal to zero center frequency, decimators that down-samples the signals by a factor of K, and half-bandwidth low-pass filters that further reduce the signal spectral bandwidth by half. The mixer or the complex multiplier multiplies the input signal by a locally generated sinusoid to shift the spectrum of the signal to be centered near zero frequency. A typical implementation uses two multipliers, one each for the I and Q channels. The on board numerically controlled oscillator (NCO) is responsible for generating the sampled digital sinusoid. The decimators are implemented using a four-stage cascaded integrator-comb (CIC) filter. Figure 5.8 shows the schematics of the

CIC implementation. The CIC filter is highly computationally efficient by only using adds and delays and is widely used in decimation and interpolation [Hogenauer 22]. A 31-tap half-bandwidth filter for spectral shaping and out of band signal rejection is cascaded with the CIC decimator to form a complete multi-rate digital down conversion stage. The overall decimation rate is between 4 to 512. With the main ADC on the USRP2 sampling rate at $100MS/s$, the maximum output sample frequency that can be achieved is $25MHz$ for both in-phase and quadrature channels. The transmit circuit of the USRP2 is the reverse of that of the receiver. A digital up-converter which consists of a CIC interpolator, mixer, and NCO is implemented in the FPGA.

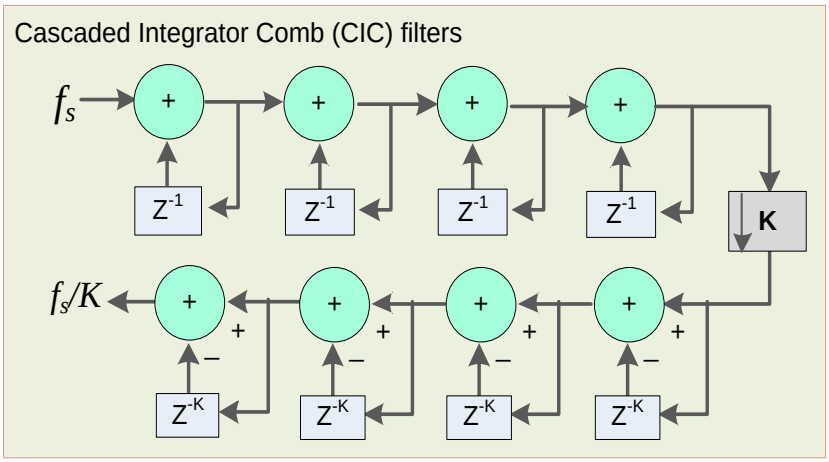

Figure 5.8: Four-stage cascaded integrator-comb (CIC) filter implementation architecture.

A major problem with the USRP2 is that its onboard oscillator is not stable in terms of frequency and phase. The temperature stability of the TCXO on the RFX board is about 2.5 ppm which would cause a frequency offset about $4,000Hz(2.5e^{-6} \times 1.57e^{9})$ at GPS L1 band. This large frequency offset cannot be differentiated from the scintillation impacts. The frequency offset also changes rapidly which results in loss lock of the carrier tracking

loop. One solution to this problem is to use a high-quality external oscillator. A small Wenzel 10-MHz OCXO oscillator is used as an external clock in our experiments. This oscillator has a specified temperature stability of 0.0015-0.005 ppm and a reasonably low phase noise at 10 MHz. The OCXO can reduce the frequency offset of the carrier to the level of few hertz. In the following section, we describe the detailed data collection system setup and receiver signal processing algorithms used to track the GNSS signals for USRP2 performance evaluations.

5.4 Data Collection System Setup

A common antenna and local oscillator are shared among several receivers in two configurations, as shown in Figure 5.9, to evaluate the USRP2 front end performance for GPS (switch position 1) and GLONASS (switch position 2) signals, respectively. In switch position 1 configuration, a custom instrumentation quality three-frequency GPS receiver RF front end data collection system TRIGR [Gunawardena et al. 2008], a NovAtel Propak dual frequency (GPS L1 and legacy L2 signal) receiver, and two USRP2 front ends split inputs from the same Novatel GPS-703-GGG wide-band antenna. A low noise OCXO clock is used to drive the TRIGR and two USRP2 RF front ends. The same receiver processing algorithms are applied to the collected GPS L1, L2C, and L5 data by the USRP2 and TRIGR front end. The NovAtel receiver is used to verify the GPS L1 signal processing results as it is not capable of processing the new L2C and L5 signals and the GLONASS signals. In switch position 2 configuration, a Septentrio PolaRxS receiver and two USRP2 front ends are tuned to collect GLONASS L1 and L2 signals, respectively. Our custom developed receiver signal processing algorithms are used to process the USRP2 IF samples, while

the Septentrio PolaRxS receiver tracking outputs for GLONASS L1 and L2 are generated using proprietary software.

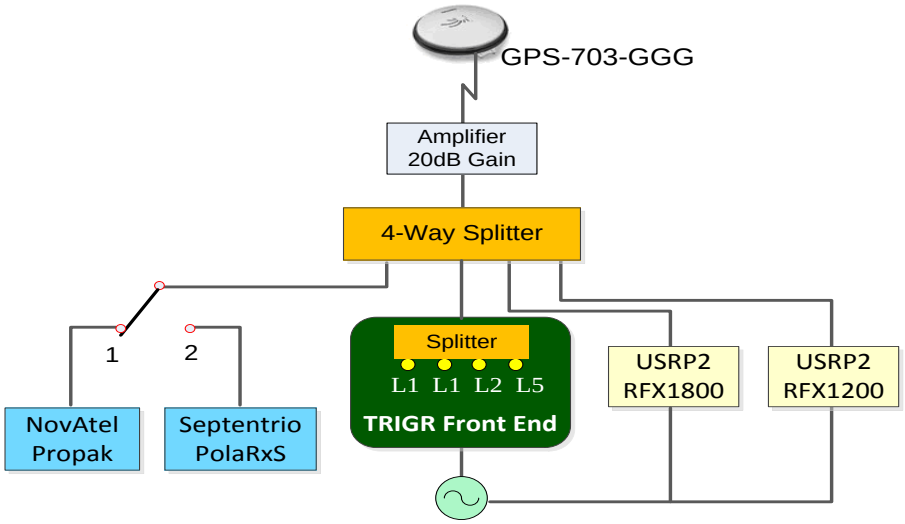

Figure 5.9: RF data collection setup at Miami University for USRP2 performance evaluation of GPS L1, L2, and L5 (switch position 1)GLONASS L1 and L2 (switch position 2) processing.

Two experimental setup configurations as shown in Figure 5.9 are used to collect data to evaluate the performance of the USRP2 as a flexible GNSS RF front end. The first configuration aims to collect GPS L1, L2, and L5 data while the second configuration is used to collect GLONASS L1 and L2 signals. In both configurations, a NovAtel GPS-703-GGG wide-band antenna is used to intercept signals for all of the receivers in each setup, and a common low noise OCXO oscillator provides timing signal to drive the three RF front ends. In the first configuration (switch at position 1), the antenna output passes a 4-way splitter to a TRIGR front end, a NovAtel OEM4 dual frequency receiver, and two USRP2 front ends. The TRIGR is a wideband instrumentation quality RF front end built at the Ohio Univer-

sity Avionics Engineering Center [Gunawardena et al. 2008]. It has four channels: two GPS L1s, one L2, and one L5. Each of the TRIGR front end channel has a fixed sampling frequency of 56.32MHz and IF frequency at 13.68MHz with configurable bit resolution at 2, 4, 8, and 16. In our experiment, we select the 8-bit resolution option. The NovAtel receiver is used as an additional reference to verify the acquisition and tracking results of GPS L1 signals generated by the USRP2 front end. The USRP2 sampling frequency is set to 5MHz and bit resolution is 16 bits for the narrowband GPS L1 and L2C signals. For the wide-band GPS L5 and GLONASS L1 and L2 signals, the USRP2 sampling frequency is 20MHz and bit resolution is 1 bit.

In the second configuration, the same antenna is connected through a 2-way splitter to two USRP front ends and a Septentrio PolaRxS receiver. This configuration is used to validate the GLONASS data collection and signal quality from the USRP2 front end against the commercial receiver outputs. Two daughter boards were used in the USRP2 data collection experiments: RFX1200 for GPS L2 and L5 and GLONASS L2, and RFX1800 for GPS L1 and GLONASS L1. Although the DBSRX board offers coverage of all GNSS signal spectrum, it has sub-optimal performance compared to the RFX series [Peng et al. 2010]. Therefore, it is not used in this study.

The ultimate performance evaluation for the USRP2 front end as an ionosphere scintillation monitoring device is the GNSS signal observables, such as the carrier to noise ratio C/N_0 and carrier phase noise [van Dierendonck 2005]. A complete suite of C++ based post processing algorithms has been developed to acquire and track GPS L1, L2C, L5, and GLONASS L1 and L2 signals. Acquisition of GPS signals are initiated with a FFT-based two dimensional search of the L1 signal CA code phase and carrier Doppler frequencies [Tsui 2004]. As three GPS channels (L1, L2C and L5) are synchronized in the TRIGR

front end, the L1 C/A code phase is used to initialize tracking for L2C (CM, CL) and L5(I, Q). The initial Doppler shift frequencies for L2C and L5 are derived from the Doppler shift frequency of L1. The acquisitions of GPS L1, L2C, and L5 signals from the IF data collected by USRP2 are done separately with 10ms of coherent integration as signals from two USRP2 boards are not synchronized in the experiments.

5.5 Ionosphere Scintillation Receiver Performance Requirements

The purpose of this work is to examine whether the USRP2 front end is suitable for collecting GPS and GLONASS data for ionosphere scintillation studies. Ionosphere scintillations cause carrier phase fluctuation and signal amplitude fading. A suitable receiver for ionosphere scintillation studies need to be able to minimize or limit thermal noise, local oscillator phase noise, and out-of-band interference contributions to the carrier phase and signal intensity measurements. Failure to understand the limitation of the instrument may lead to misleading scintillation results [van Dierendonck 2005]. The important qualities of a typical receiver for scintillation studies are: (1) the clock phase noise of the RF front end, (2) the receiver noise figure, and (3) the performance of the carrier tracking loop.

It is difficult to separate the clock phase noise caused by the RF front from the fluctuations caused by phase scintillation. The clock phase noise of a RF front end mainly consists of contributions from the reference oscillator, the voltage-controlled oscillator (VCO), and frequency synthesizers. The magnitude of the phase noise of a TCXO is much larger than typical weak phase scintillation effects, while the phase noise of an OCXO can be smaller

than the scintillation effects. A practical way to estimate the GPS carrier phase fluctuation caused by the oscillator and the VCO is to measure the detrended phase output of the receiver. [Fremouw et al. 1978] reported weak phase scintillations with magnitude around 0.086 radians. Recent studies of high-latitude scintillations have shown many scintillation activities with phase scintillations with magnitude in similar or even smaller values [Vikram 2011]. In order to detect weak scintillation events, the reference oscillator, the VCO, and associated frequency synthesizer generated phase noise needs to be minimized.

The noise figure of the receiver is another important quality of a scintillation receiver. A large noise figure will result in degraded C/N_0 performance and less accuracy in signal intensity measurements. At the L band, strong scintillations may cause deep amplitude fading ($> 20dB$) associated with rapid phase changes [Humphreys et al. 2010a; Zhang et al. 2010]. Such signal dynamics causes cycle slips or even loss lock of the carrier tracking loop [Humphreys et al. 2010b]. A GPS receiver with low-noise figure can help to improve the tracking loop stability during strong scintillation events and reduce the phase error cause by the carrier tracking loop since the phase noise standard deviation caused by a PLL is related to C/N_0 by [Kaplan et al. 2005]:

$$\delta_{PLL} = \frac{360}{2\pi}\sqrt{\frac{B_N}{C/N_O}(1+\frac{1}{2TC/N_0})} \tag{5.5}$$

where B_N is the PLL loop noise bandwidth, T is the coherent integration time, and C/N_0 is the carrier-to-noise ratio. Quantitative analysis of USRP2 front end noise figure and the phase noise is presented in a later section.

Robust tracking loop design is needed to maintain tracking of the signal during deep amplitude fading. Several methods can be used to achieve this purpose: extended integration time, adaptive approaches with adjustable tracking loop parameters, and pure

PLL/FLL. A pure PLL/FLL can track the signals with an additional 6-dB gain compared to the conventional PLL/FLL [Kaplan et al. 2005]. For dataless pilot signals such as L2CL and L5Q signals, the pure PLL/ FLL approach can be implemented for real-time applications. For applications only requiring post processing, navigation messages can be decoded in advance and removed from the data-modulated signals before a pure PLL/FLL can be applied. Vector-based tracking loops make use of information from healthy satellites to assist the tracking of satellite signals experiencing scintillation, significantly improve the tracking loop performance. An extended Kalman filter-based vector tracking loop has been developed [Peng et al. 2012] and tested with strong scintillation data collected during last solar maximum [Zhang et al. 2010].

5.6 USRP2 Performance Analysis

A quick time series analysis of the USRP2 outputs is presented here to demonstrate the basic validity of its measurements. It is commonly accepted that the output of a properly designed and constructed RF front with antenna disconnected should be normally distributed. Figure 5.10 shows the sample distribution of USRP2 output is well fitted with an ideal zero mean Gaussian distribution.

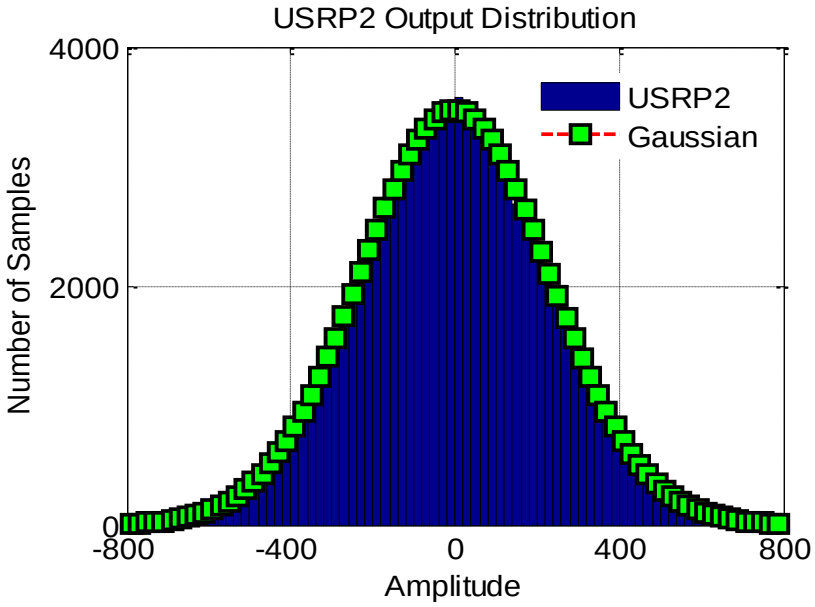

Figure 5.10: Distribution of the USRP2 outputs of the GPS L1 signals.

To further verify the randomness of the RF data, the collected data sample auto-correlation coefficients are calculated:

$$r_k = \sum_{t=1}^{N-k}(x_t - \overline{x})(x_{t+k} - \overline{x}) / \sum_{t=1}^{N}(x_t - \overline{x})^2 \tag{5.6}$$

where x_t represents the output samples, k is the lag between samples, and $N = 10^6$ is the total number of samples. Figure 5.11 shows the plot of the first 100 correlation coefficients. Small correlations exist at various lags which indicate that the RF data are not completely random.

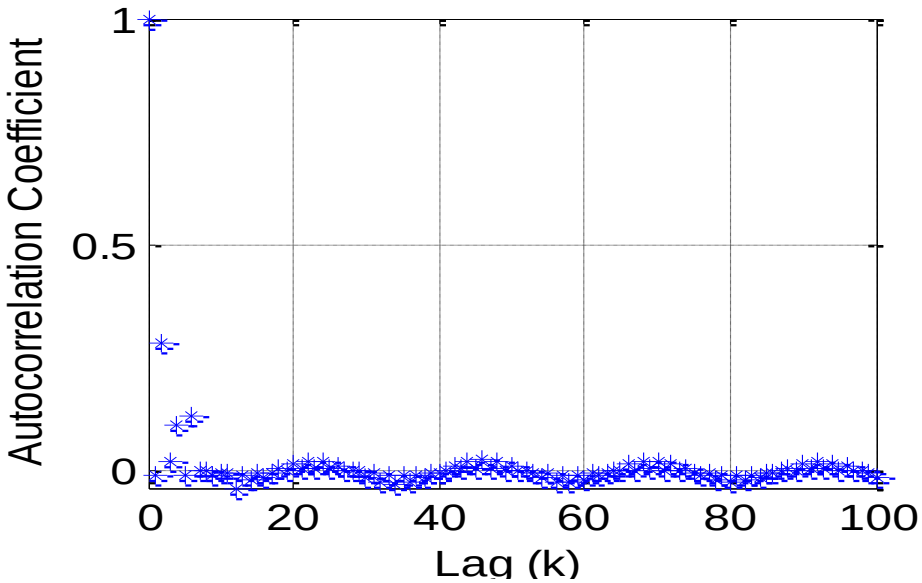

Figure 5.11: Auto-correlation of the USRP2 outputs.

The GPS L1 signal spectrum from outputs of the USRP2 and the TRIGR front end collected using the setup in Fig. 5.9 are shown in Figure 5.12. The small peak at the center is the result of all combined visible satellite GPS L1 C/A code energy. The spectrum of the USRP2 is not as clean as that of the TRIGR front end. The spectral spikes contained in the USRP2 outputs may result in degraded performance. Performance comparisons will be presented at a later section.

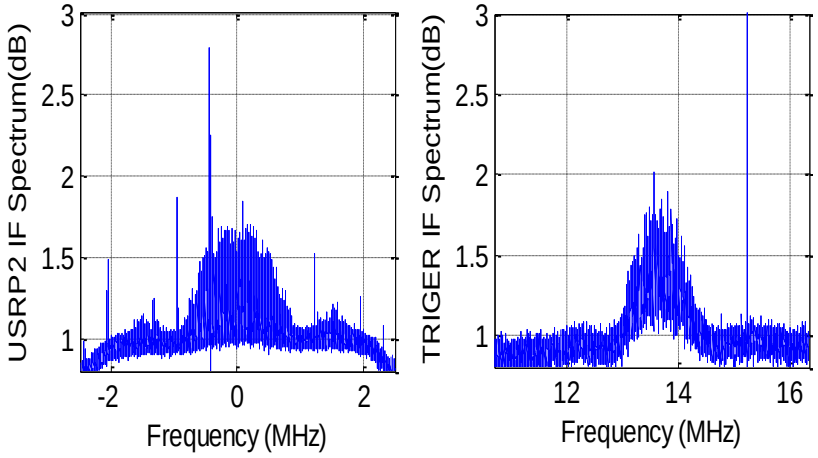

Figure 5.12: IF spectrum of the USRP2 (left) and TRIGR (right) outputs of the GPS L1 signals.

For this study, our performance evaluations are focused on the C/N_0 and carrier phase measurements. As only two USRP2 boards were available during the data collection experiments, the triple frequency GPS RF data were collected at two different time intervals, each lasting 6 min. The L2C and L5 data were simultaneously collected by the two USRP2 boards and the TRIGR front end on 1/13/2011, 20:22:00 EST. The GPS L1 data were collected on 3/31/ 2011 at 11:37:42 EST by one USRP2, the TRIGR front end, and the NovAtel receiver. For GLONASS data collection, two USRP2s and a Septentrio PolaRxS receiver collected GLONASS L1 and L2 on 1/15/2011 at 22:07:39 EST. Figure 5.13 shows the satellite sky plots during the GPS L1 and GLONASS L1 and L2 data collection. The following subsections discuss the performance evaluations based on these measurements.

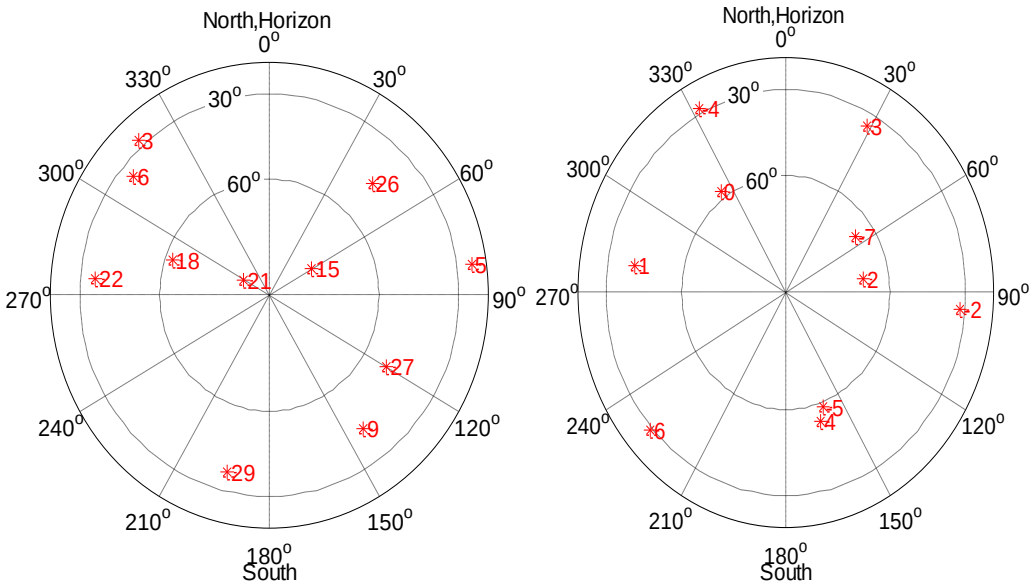

(a) GPS Sky plot (1/13/2011, 20:22 EST)

(b) GLONASS Sky plot (1/15/2011, 22:07:39 EST)

Figure 5.13: Satellite path sky plots at Oxford, Ohio during data collection experiments. a GPS Sky plot (1/13/2011, 20:22:00 EST) b GLONASS Sky plot (1/15/2011, 22:07:39 EST).

5.6.1 C/N_0 Measurement Performance

The following equations are used to compute the C/N_0 using the I and Q channel correlator outputs for the USRP2 and TRIGR front end [van Dierendonck et al. 1996]:

$$WBP_j = (\sum_{i=1}^{M}(I_i^2 + Q_i^2))_j \tag{5.7}$$

$$NBP_j = (\sum_{i=1}^{M}(I_i^2))_j^2 + (\sum_{i=1}^{M}(I_i^2))_j^2 \tag{5.8}$$

$$NP_j = \frac{WBP_j}{NBP_j}, \widehat{\mu}_{UP} = \frac{1}{j}\sum_{i=1}^{M}(NP_j) \tag{5.9}$$

$$C/N_0 = 10log(\frac{1}{T}\frac{\widehat{\mu}-1}{M-\widehat{\mu}}) \tag{5.10}$$

where WBP and NBP are the so-called wide-band and narrow-band signal power measurements, respectively, and T is the correlator integration time. In this work, we used $T = 1ms$, $M = 20$, and $K = 50$ in our calculations. We compared the performance of the USRP2 for all eleven satellites in view with the NovAtel receiver outputs and the TRIGR front end during the same experiment time period. The average and standard deviations of the L1 signal C/N_0 values for the eleven satellites during the 6-min data collection period are plotted in figure 5.14. The results show that USRP2 C/N_0 is typically about $1 \sim 2$ and $1 \sim 3dB$ lower than that of the NovAtel receiver and the TRIGR front end, respectively. The C/N_0 standard deviations from USRP2, TRIGR, and NovAtel are comparable within a fraction of a dB. The standard deviations of the NovAtel receiver are slightly less than the two RF front end outputs as different tracking algorithms and filter parameters may be used in the NovAtel receiver. We can also see that satellites with low elevation angles, such as PRN 3 and 5, have larger amplitude fluctuations, while satellites with high elevations, such as PRN 15 and 21, have larger C/N_0 and smaller standard deviation, as expected. The software receiver processing results of GPS L2CM and L5I from USRP2 and TRIGR front end are plotted in figure 5.15. PRN 25 was the only satellite broadcasting L5 signals during the data collection time. We can also see that USRP2 C/N_0 is typically about $1 \sim 3dB$ lower than that of the TRIGR front end.

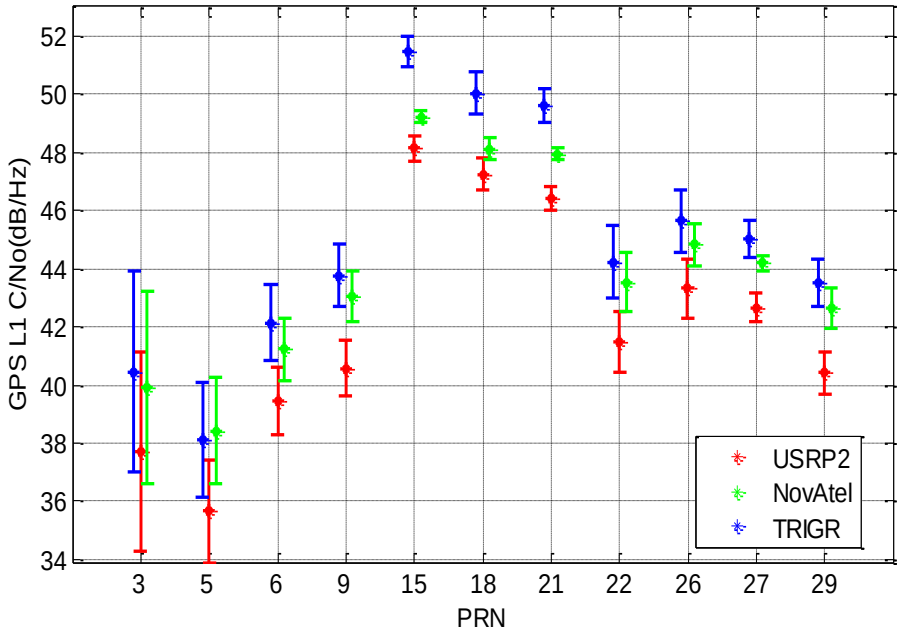

Figure 5.14: Average and standard deviations of GPS L1 signal C/N0 from USRP2, TRIGR front end, and NovAtel receiver for all GPS satellites in view during a 6-min experiment.

Figure 5.16 compares the average GLONASS L1 and L2 C/N_0 values obtained using the USRP2 and Septentrio PolaRxS over 6 min taken on January 15, 2011, starting at 22:07:39EST. With the exception of channel-4 that is ruled as unhealthy during the data collection experiment and hence was not tracked by the PolaRxS, both receivers show comparable measures at both L1 and L2 for all remaining 9 SVs. The results also show that the C/N_0 standard deviations are also of comparable values for both receivers.

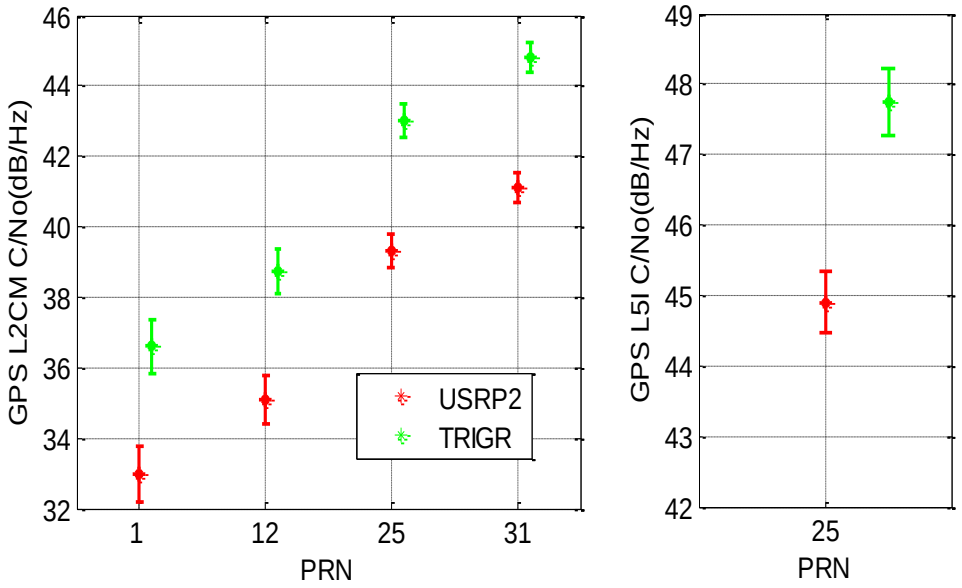

Figure 5.15: Average and standard deviations of GPS L2 and L5 signal C/N_0 from USRP2 and a Novatel receiver.

5.6.2 Carrier Phase Measurements

Carrier phase fluctuation is another important measure of ionosphere scintillation. When there is no scintillation, the output of the carrier phase tracking loop for a receiver with a low-phase-noise OCXO clock on a stationary platform is dominated by the satellite-receiver Doppler frequency and Doppler rate [Razavi et al. 2008], which can be adequately represented by a fourth-order polynomial [Peng et al. 2010]. The remaining high-frequency components of the phase variations are due to RF front end noise and possible RF interference. These components are the limiting factors in the receivers ability to detect ionosphere scintillations, if the low-frequency components can be effectively removed. The conventional approaches include a fourthorder polynomial fitting and a sixth-order Butterworth filter to remove the satellite-receiver dynamics and other slowly changing errors. Differ-

encing between two signals from different band (such as L1 and L2) of the same satellite can also remove satellite-receiver dynamics and oscillator effects [Wang et al. 2012], if the same front end is used to collect and process both signals. In our experiment, two separate USRP2s are used to collect L1 and L2 signals, and the L5 signal is collected at a different time. Therefore, this option is not applicable. A sixth-order Butterworth high pass filter with 0.1-Hz cutoff frequency has been used in [van Dierendonck et al. 1996] for detrending of the 50-Hz phase outputs, while a fifteenth-order Butterworth filter with 0.1-Hz cutoff frequency has been used in [Zhang et al. 2010] for 1,000-Hz phase outputs. The filter used in [Zhang et al. 2010] takes a few minutes before convergence occurs, so a fourth-order polynomial fitting is used in this work for de-trending the 1,000-Hz carrier phase outputs of the software receiver. The detrended outputs from both USRP2 and TRIGR for the L1, L2CM, and L5I on PRN 25 are shown in Figure 5.17. The figure shows that USRP2's carrier phase noise is slightly higher than that of the TRIGR for this satellite on all three bands.

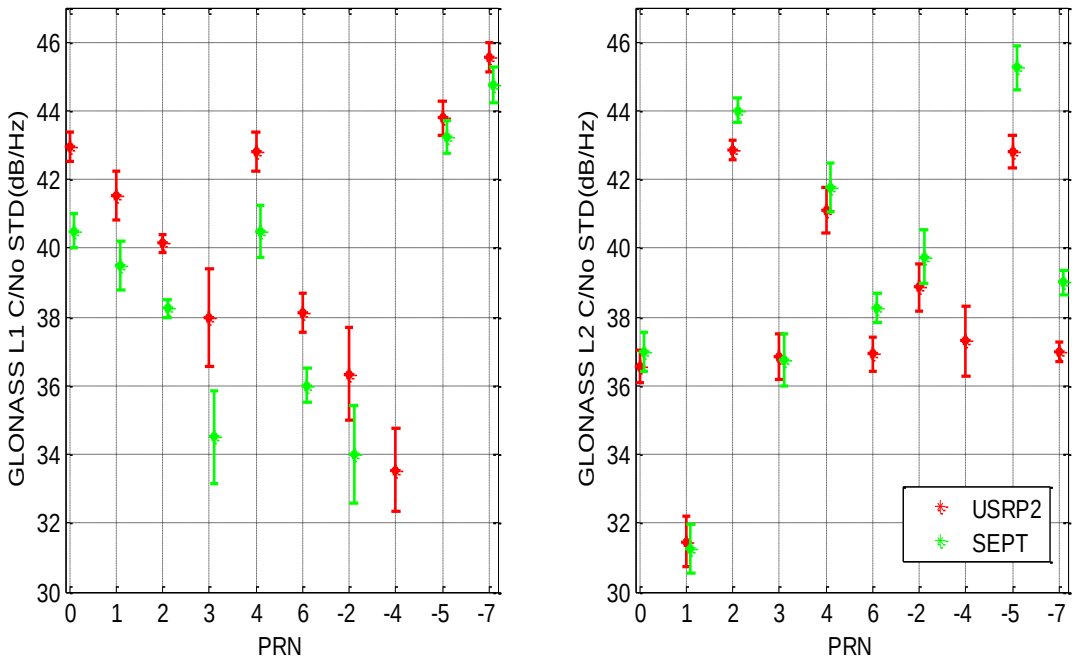

Figure 5.16: Average and standard deviation of C/N_0 generated from USRP2 and Septentrio PolaRxS for GLONASS L1 and L2.

Figure 5.18 shows the carrier phase standard deviations for all GPS satellites in view during the experiments. At L1, the USRP2 and TRIGR carrier phase standard deviations are comparable to within 0.1 degrees. At L2CM, USRP2 carrier phase standard deviation is consistently larger than that of the TRIGR. The difference may exceed 1 degree. At L5, we only have one SV signal which shows that USRP2 underperforms TRIGR by a fraction of a degree.

The more useful signals for ionosphere scintillation studies are the L2CL and L5Q, as they do not have data modulation on them. As a result, a longer coherent integration interval can be applied and a pure PLL based tracking loop can be used to improve the signal tracking threshold. More importantly, strong ionosphere scintillations may be accompanied by sudden 180 degree phase changes that may be difficult to distinguish from data bit transitions [Humphreys et al. 2010a]. Our results show that the performance of L2CL and L5Q signals under the benign condition of the test data presented are very similar to L2CM and L5I, respectively. Therefore, in the analysis presented so far, only L2CM and L5I signals are presented.

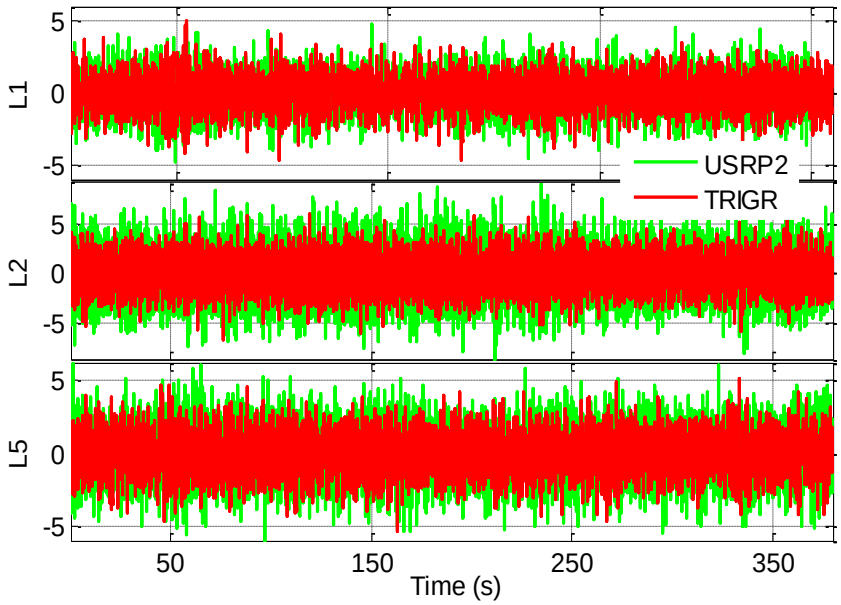

Figure 5.17: Detrended PRN25 carrier phase measurement comparison between USRP2 and TRIGR front end.

Figure 5.19 shows the detrended carrier phase standard deviations for GLONASS L1 and L2 satellites signals captured during the experiment using the USRP2 and the Septentrio receiver. While the USRP2 carrier standard deviation appears to be slightly lower than that of the Septentrio for GLONASS L1, the opposite is true for GLONASS L2. Overall, the two receivers yield similar performances with the differences being limited to less than a small fraction of a degree. By comparing Figs. 16 and 17, we can see that the GLONASS satellite signals carrier phase measurements are much noisier than those of GPS satellite signals. The relatively large phase fluctuations on both the USRP2 front end and the Septentrio receiver appear to indicate that these fluctuations are intrinsic to the signals themselves. These fluctuations make the GLONASS signals less suitable for ionosphere scintillation studies because it will be difficult to separate true scintillation events from these non-scintillation effects.

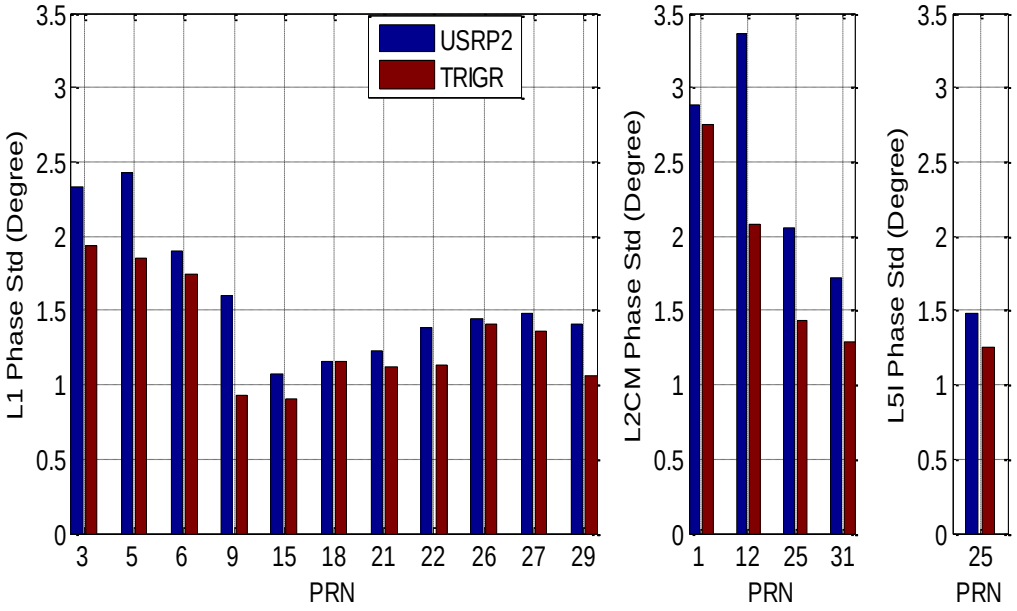

Figure 5.18: Detrended carrier phase standard deviation comparison between USRP2 and TRIGR front end for GPS L1, L2CM, and L5I.

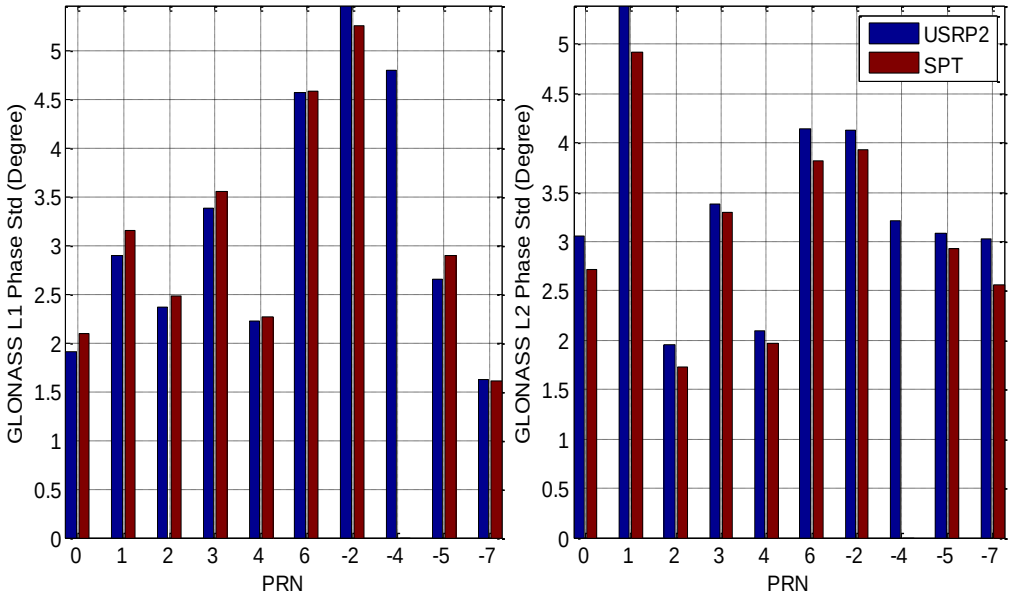

Figure 5.19: Detrended GLONASS L1 and L2 carrier phase standard deviations.

5.6.3 Analysis of The Front End Performances

Possible causes of the C/N_0 difference between the TRIGR front end and the USRP2 board are the receiver front end noise figures, VCO and frequency synthesizer quality, and ADC bit resolutions. The noise figure of the USRP RFX daughter board is estimated using a GPS simulator with known input signal power levels. The noise figure is defined by:

$$F = \frac{S_i/N_i}{S_0/N_0} = \frac{N_0}{GkTB} \tag{5.11}$$

where $B = 2MHz$ at GPS L1 signal bandwidth, G is the receiver front end gain, T is the effective receiver input temperature $290K$, $k$is the Boltzmanns constant, and N_0 is the output noise power. From (5.11), we obtain the reference noise N_{0i} dependency on the noise figure F:

$$N_{0i} = N_0/G = FkTB \tag{5.12}$$

The reference noise can be computed with known input power S_i and estimated output SNR_{out}:

$$S_i/N_{0i} = SNR_{out} \tag{5.13}$$

Equation (5.12) and (5.13) are used to compute the noise figure F. A GPS simulator is used to generate a $-130dBm$ input and a $-140dBm$ input, respectively. Their corresponding output SNRs are estimated to be -10 and $-21dB$, respectively. So the noise figure for the RFX board used in the front end is around $-10dB$. A combined processing of the complex outputs of USRP2 would provide 3dB additional SNR improvement over using the real output only as is in the case of the TRIGR front end. The noise figure of the TRIGR front

end is around 4dB [Gunawardena et al. 2008]. So we expect the SNR or C/N_0 of the USRP2 is about 3 dB less than that of the TRIGR front end for the same L1 or L2 signal source. It should be noted that the measurement of one individual board may not be a good representation of noise figure of the all RFX series boards. The 1-bit re-quantization of the wideband GPS L5 and GLONASS signal may result in $1 \sim 2dB$ further signal power loss. A FPGA-based real-time raw RF data collection system is currently under development to increase the bit resolution of the wideband samples for the USRP2. The 5 $6dB$ C/N_0 difference between the L5I and L2CM tracking results in Fig. 13 is caused by the GPS satellite broadcasting power difference. The L2C is broadcasting at 2-dB power lower than L5I (GPS ICD- 705). Another 3-dB loss is expected with L2CM or L2CL tracking loop as the signal is time-multiplexed. So the total C/N_0 output for L2CM is about 5 dB less than for L5. The sub-optimal noise performance of the USRP2 can be compensated by better tracking loop design. For example, increasing the coherent integration time from 1 ms to 10 ms will result in a gain of 10 dB in SNR. The vector tracking loop developed for the USRP2 data processing can maintain lock of the GPS signal during canonical fade with signal intensity fading of more than 20 dB.

As shown in Fig. 15, the phase noise of the USRP2 is slightly larger than the TRIGR front end even with a common reference used. There are two major reasons that may cause this difference. The first reason is the lower C/N_0 output of the USRP2 that would cause larger phase noise by Eq. (5.5). The second cause is the integrated VCO/ synthesizer on board the RFX daughter board. A two-stage PLL frequency synthesizer is used to generate the reference carrier to down-convert the RF signal to IF in the TRIGR front end, while a one-stage synthesizer is used in the USRP RFX daughter board. The ADF4360-3 chip is used in the RFX1800 daughter board. These reference synthesizers introduce their own

phase noise to the IF samples. The phase noise of the synthesizer or the PLL is measured in terms of single-sideband (SSB) power density relative to the carrier in units of dBc/Hz. Table 2 summarizes the specifications of the synthesizers for the TRIGR and the RFX1800 daughter board. We can see that the synthesizer of the USRP2 board causes slightly larger phase noise than the TRIGR. For the GPS L1 signal with 2-MHz bandwidth, the noise cause by the VCO in the USRP2 board is about $-70dBc(133+10\times log_{10}(2M))$, while the TRIGR is about $-79dBc(133+10\times log_{10}(2M))$, both are insignificant. The differences in the carrier phase noise performance between the two front ends are also unsubstantial. Even through the phase stability of the USRP2 board is not as good as that of the TRIGR front end, the standard deviation of the USRP2 phase noise is quite adequate for scintillation researches.

Table 5.3: Daughter boards for GNSS receivers

Front end Type	TRIGR		USRP2(RFX1800)
Specification	PLL1	PLL2	ADF4360-3
SSB Phase Noise Density	-115dBc/Hz@1kHz	-111dBc/Hz@1 kHz	-110dBc/Hz@100 kHz
	-142dBc/Hz@1 MHz	-142dBc/Hz@1 MHz	-133dBc/Hz@1MHz

5.7 Conclusions

With appropriate daughter board configurations, the USRP2 front end can capture the entire GNSS family of signals. Our objective is to evaluate the performance of the USRP2 front end as an ionosphere scintillation monitoring device. For this purpose, we established

experimental setups that allow simultaneous data collection of the USRP2 front ends, an instrumentation quality custom GPS front end TRIGR, and two high end commercial GNSS receivers from the same antenna and driven by the same local oscillators. GPS L1, L2C, and L5 and GLONASS L1 and L2 raw IF samples were collected using the RF front ends, while the commercial receivers generated processed signal observables. The IF samples collected by the USRP2 front ends and the TRIGR front end were processed using the same software acquisition and tracking algorithms. The results show that USRP2 typically generates GPS C/N_0 at about $1 \sim 3$ dB below that of the TRIGR and $1 \sim 2$ dB less than that averaged output of NovAtel receiver. The carrier phase fluctuations generated by the two front ends are comparable, with the exception of one particular GPS L2C signal for which the USRP2 front end appears to have larger phase fluctuations (by no more than 1.5 degrees) compared to TRIGR. We do not have direct GLONASS signal IF processing results comparison between the USRP2 and the TRIGR front end as the latter is a dedicated GPS front end. The USRP2 GLONASS processing results are compared with the outputs generated by the Septentrio PolaRxS receiver, and their performances appear to be comparable. The results show that GLONASS signals have relatively large C/N_0 and carrier phase fluctuation which appear to be unrelated to the signal propagation environment. While the additional GLONASS satellite signals have great added benefits in applications, such as ionosphere tomography studies, these signal fluctuations make them less desirable.

Chapter 6

High Latitude Ionosphere Scintillations at L5 Band

6.1 Chapter Overview

The GPS L5 signal is transmitted at the protected ARNS and intended to provide better assurance for safety-of-life applications such as aviation. With a relatively low carrier frequency at 1.176GHz and a higher chipping rate at 10.23MHz, L5 is more susceptible to ionospheric scintillation compared to the other civilian signals in the L1 and L2 band. It is well documented that ionospheric scintillations cause increased carrier tracking error and may lead to receiver loss of lock under severe conditions [Zhang et al., 2010; Humphreys et al., 2010]. For aviation and other applications that require continuity and integrity, ionospheric scintillation poses a safety hazard. This is especially true as we enter a new solar maximum period when scintillation activities will increase in both frequency and intensity. The objective of this work is to investigate the impact of ionospheric scintillations on L5

signals. To achieve this objective and support ionospheric scintillation studies in general, an array of commercial GPS receivers and RF front ends GNSS data collection devices have been setup in Gokona, Alaska to collect ionospheric scintillation data as described in the previous chapter.

In this chapter, the scintillation impacts on GNSS signals are studied with available theoretical model and verified with real scintillation data. Specifically, the scintillation impact on GPS L5 is analyzed in details. Some preliminary results of the scintillation correlation among different frequency channels are provided. Further discussion about the problem of the current scintillation study methods are also considered and temporary solution is also suggested.

6.2 Channel Synchronization

The new L5 signal is part of the GPS modernization to improve GPS performance for civilian users. The performance of the L5 has been extensively evaluated [Tran 2004]. The code tracking error of L5 due to thermal noise and wide-band interference are lower than that on L1 signals. The carrier tracking of the L5 is much more robust than L1 with a tracking threshold improvement of 3.5 dB [Tran 2004]. The L5 code also provides better performance for longer delay multi-path as a smaller chip length is used in L5 than in L1. However, the real ionospheric scintillation impact on the L5 remains unknown as scintillation data on L5 is very scarce [Seo et al., 2011]. In the paper by [Kim et al., 2003], a frequency domain scintillation model is used to evaluate the performance of L5. But frequency correlation among L1, L2, and L5 were not discussed.

This work will analyze in detail the scintillation correlation on different bands using

triple frequency data collected at HAARP. As mentioned earlier, the wide-band L5 scintillation data is collected by the USRP2 while the narrow band (L1 and L2) RF data is collected by the TRIGR front end. Although the two front ends data collection processes are triggered by the same software and are driven by the same oscillator, they have different starting times and sampling frequencies as illustrated in figure 6.1.

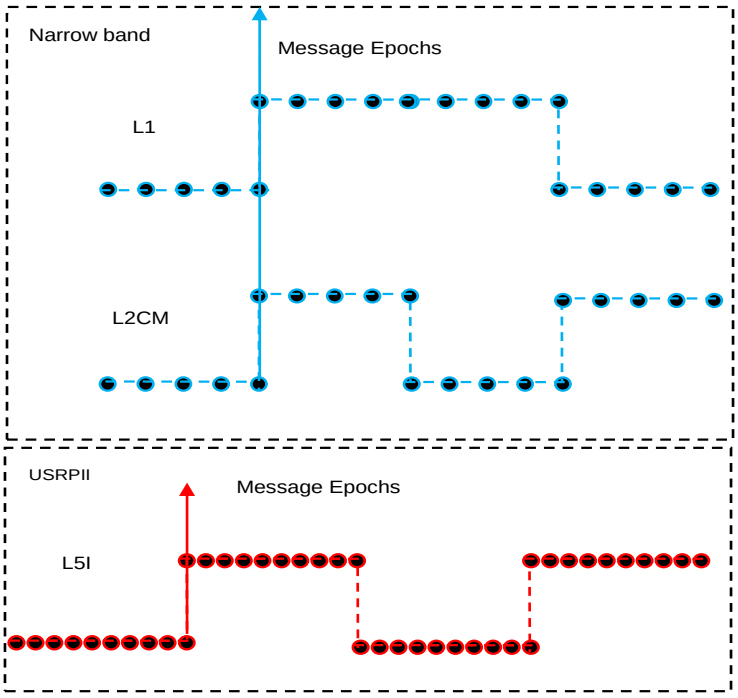

Figure 6.1: Synchronization between different front ends.

Since a major objective of this work is to determine the relative impact of scintillation on different bands, the scintillation data collected by different RF front ends must be aligned accurately. GPS signals are synchronized with message epochs when transmitted from GPS satellites. We can extract the messages and align data from different front ends based on decoded GPS time. Since the message on L1 is not encoded with an error correction code, it is quite straightforward to obtain the GPS time on L1. The message content and decoding

methods for L5 are described in chapter 3.

6.3 Scintillation Effects on GNSS Receiver

The scintillation effects on GPS receivers has been studied and well documented in number of studies [Humphreys et al. 2010a; Zhang et al. 2010]. [Rino 1979] shows that the scintillation effects can be modeled by inverse power law PSD for the amplitude and phase. [Fremouw et al., 1978] shows that the L-band scintillation can be modeled by zero mean Gaussian PDF for phase and Nakagami-m distribution for amplitude. The phase scintillation spectrum can be represents by the equation below [Rino 1979]:

$$S_\phi(f) = \frac{T}{(f_0^2 + f^2)^{p/2}} \tag{6.1}$$

Where T is the spectrum strength at 1Hz and f_o is the outer scale frequency which is also corresponding to the maximum irregularity size, and p is the spectral index. When $f \gg fo$, the PSD of phase can be simplified by:

$$S_\phi(f) = T f^{-p} \tag{6.2}$$

The phase scintillation index which is also the de-trended phase standard deviation is related to the phase PSD as:

$$\sigma_\phi^2 = \int_{-\infty}^{+\infty} S_\phi df \approx 2 \int_{f_c}^{+\infty} S_\phi df = 2 \int_{f_c}^{+\infty} \frac{T}{(f_0^2 + f^2)} df \tag{6.3}$$

The amplitude scintillation follows the similar relationship except that the amplitude spectrum is attenuated after a cut-off frequency which is also called the Fresnel frequency given by equation below.

$$f_F = \frac{V_{rel}}{d_F} = \frac{V_{rel}}{\sqrt{2\lambda z}} \tag{6.4}$$

Where V_{rel} is the relative velocity between the satellite and the irregularity, λ is the wavelength and z is the distance between the irregularity to the receiver. The S_4 index is generally used as the amplitude scintillation index. The S_4 index is derived by the normalized signal intensity as shown in equation:

$$S_4^2 = \frac{< I^2 > - < I >^2}{< I >^2} \tag{6.5}$$

where I is the received signal intensity. The received power is normally detrended by filtering the intensity measurements with a low-pass filter (sixth-order Butterworth with 0.1Hz cutoff frequency) and then the normalization is accomplished by dividing the raw signal intensity by the output of the low-pass filter [Van Dierendonck et al., 1997]. The correlation between the phase scintillation and the amplitude scintillation is still not well modeled as lack of real scintillation data. [Fremouw 1980] suggests a correlation value of -0.6 based on the early data processing results. The scintillation indices on GPS L2 and L5 can be derived on GPS L1 through equation [Van Dierendonck et al., 1996],

$$S_4(L_2) = S_4(L_1)\left(\frac{f_{L1}}{f_{L2}}\right)^{1.5} = 1.45 S_4(L_1) \tag{6.6}$$

$$S_4(L_5) = S_4(L_1)\left(\frac{f_{L1}}{f_{L5}}\right)^{1.5} = 1.55 S_4(L_1) \tag{6.7}$$

$$\sigma_\phi(L_2) = \sigma_\phi(L_1)\left(\frac{f_{L1}}{f_{L2}}\right) = 1.28\sigma_\phi(L_1) \tag{6.8}$$

$$\sigma_\phi(L_5) = \sigma_\phi(L_1)\left(\frac{f_{L1}}{f_{L5}}\right) = 1.34\sigma_\phi(L_1) \tag{6.9}$$

$$S_I = T f^{-p} \tag{6.10}$$

Where $f_{L1} = 1575.42MHZ$, $f_{L2} = 1227.6MHz$, $f_{L5} = 1176.45MHz$. Clearly, ionosphere scintillation has stronger impacts on the GPS L2 and L5 channels. However the scintillation indices only represent the severity of the scintillation, the rate of the fluctuation and the

fading interval are also have strong impact on the performance of receiver tracking loop. A frequent phase fluctuation will results in the loss lock of the phase lock loop and long interval amplitude fading will also result in the failure of the code lock loop. The future dual frequency receiver (L1 and L5) can provide better estimation of the ionosphere delay and results in better PVT solutions. The correlation of scintillation impacts on GPS L1 and L5 play an important role for the availability of future dual frequency applications. A high correlation coefficient means loss lock of one frequency might loss lock of the other one. The later part of the paper presents of the software receiver processing results of several recorded scintillation events observed on L5. The correlation coefficients of L1 and L5 are also computed.

6.4 Scintillation Events Observed

Since August 2010, 20 scintillation event IF samples have been recorded at HAARP. Table 6.1 lists scintillation events recorded by the RF front ends from July 2010 to May 2011. Only 4 scintillation events are associated with PRN 25 which carries all three GPS signals (shown in red color). The event on 2010-07-19 is an artificially controlled scintillation, while the three events on 2011-03-01 are natural events associated with a geomagnetic storm. Figure 6.2 shows the magnetometer outputs at HAARP on 2011-03-01. The three scintillation events occurred near the peak magnetic variations. Figure 6.3 plots the azimuth and elevation angles of the satellite experiencing scintillations. Note that nearly all scintillation events are close to the local magnetic zenith, which verifies that scintillations at high latitude are associated with geomagnetic activities.

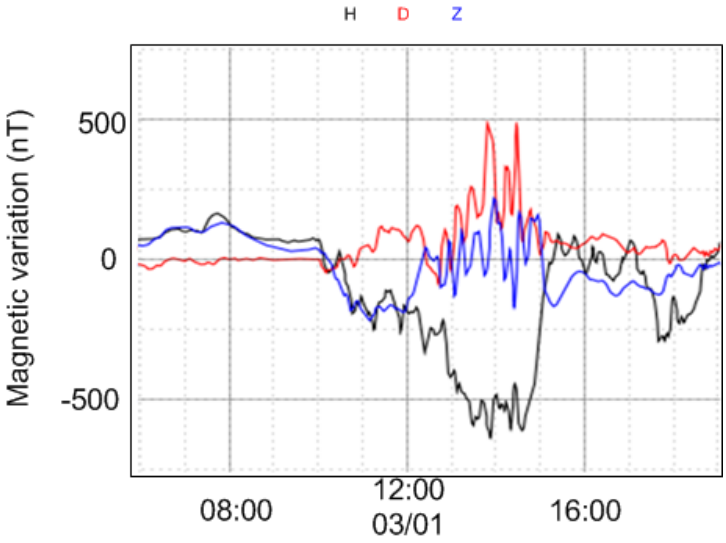

Figure 6.2: Magnetic variation on 03/01/2011.

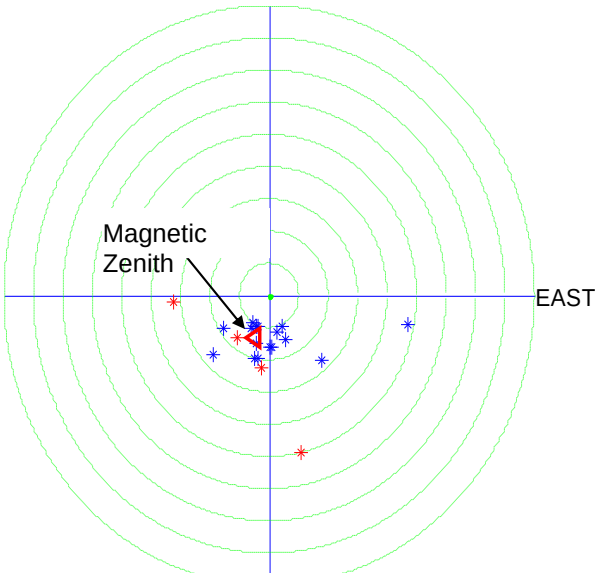

Figure 6.3: Sky plot of scintillation events.

The two commonly used indicators for amplitude and phase scintillations are the S_4 index and the de-trended carrier phase standard deviations. The peak L1 signal S_4 and σ_ϕ values

for each of the identified scintillation events are also listed in Table 6.1. Equations (6.6)-(6.9) were used to distinguish true scintillation events from other abnormal signal behavior caused by multi-path, interference, etc. For example, figure 6.4 plots the S_4 values and detrended phase of L1, L2, and L5 signals at 14:08 UTC on 03/01/2011. As we expected, the S_4 values on L2 and L5 are approximately 1.4 times of that on L1. Table 6.2 lists detailed parameter values for this event at all three bands. Clearly, scintillation has stronger impacts on the GPS L5 and L2 bands. The next section will provide further analysis based all recorded events to explore the characteristics of scintillation impacts on L5 and correlations between different frequency channels.

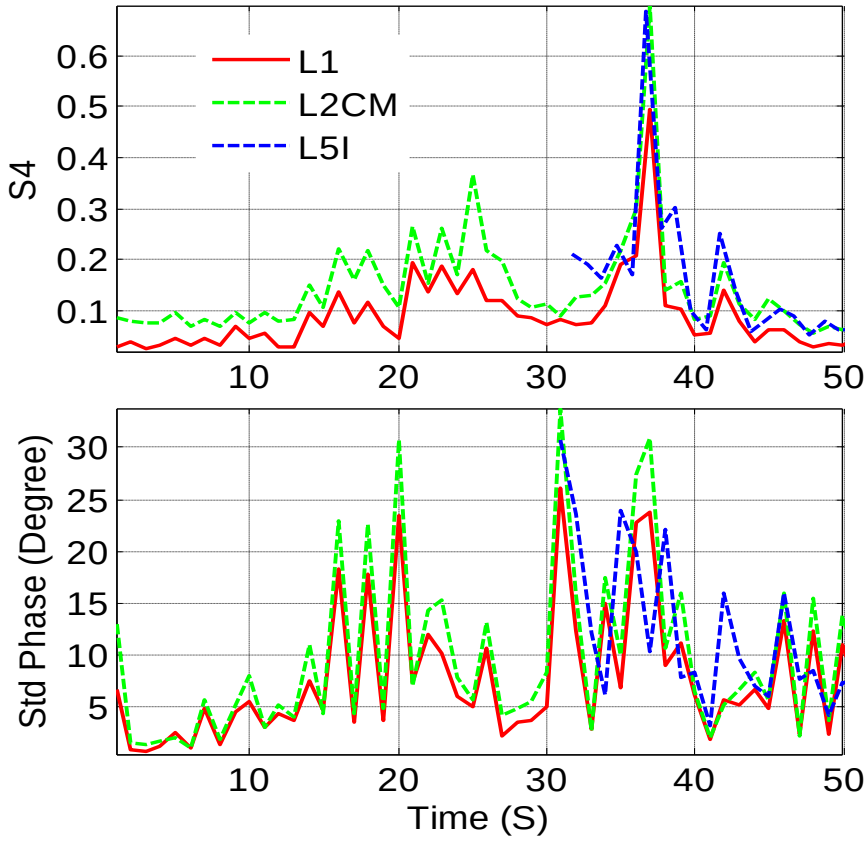

Figure 6.4: S_4 and detrended phase of a scintillation event on 03/01/2011, 14:08:48 UTC.

6.5 High Latitude Scintillation Events Analysis

The data-less GPS L5I and L2CL signals can be tracked using the four-quadrant arctan discriminator to provide more robust carrier tracking performance when deep fading and abrupt phase reversal occur during strong scintillations [Kaplan et al., 2005]. When the scintillation is weak to moderate, the atan discriminator will work and we expect the two L2C signals to have similar performances and the two L5 signals also have similar performances. This conclusion is validated by figures 6.5 and 6.6 which show the nearly identical normalized signal intensity and detrended carrier phase for L2CM and L2CL, and for L5I and L5Q respectively at 14:08:48 UTC on 03/01/2011. Although it is more beneficial to track L2CL and L5Q during scintillations, we will focus our analysis on the L2CM and L5I signals in this paper because of the near identical performance under weak to moderate scintillation scenarios for the data modulated and data-less signals, and because the messages on these the L2CM and L5I provide timing information.

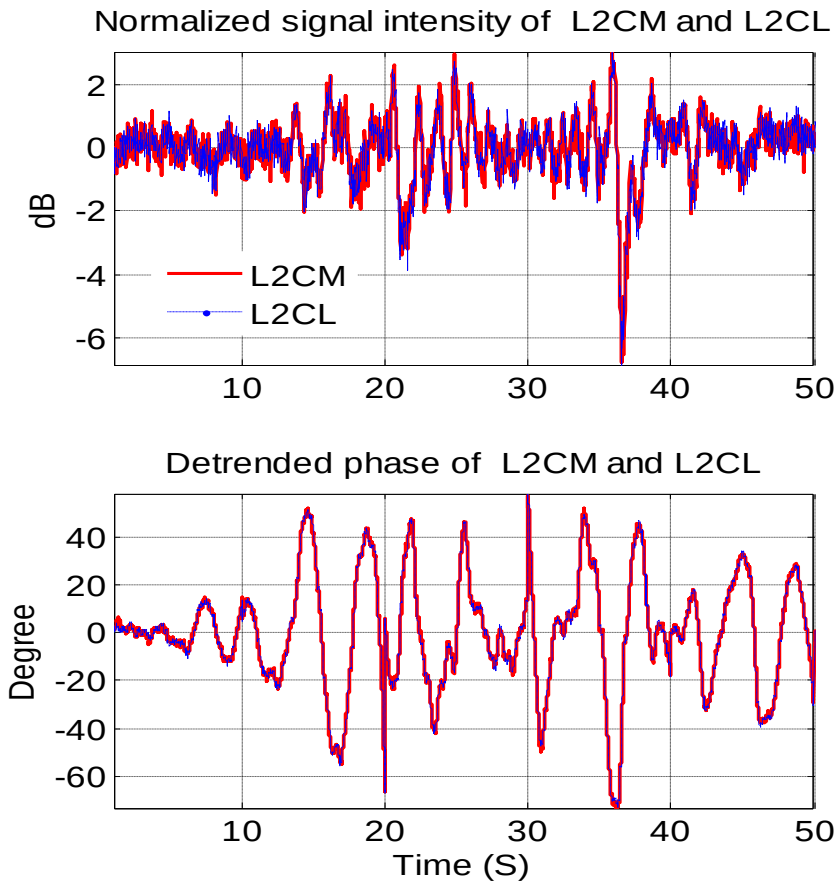

Figure 6.5: Amplitude and phase scintillation similarity on L2CM and L2CL.

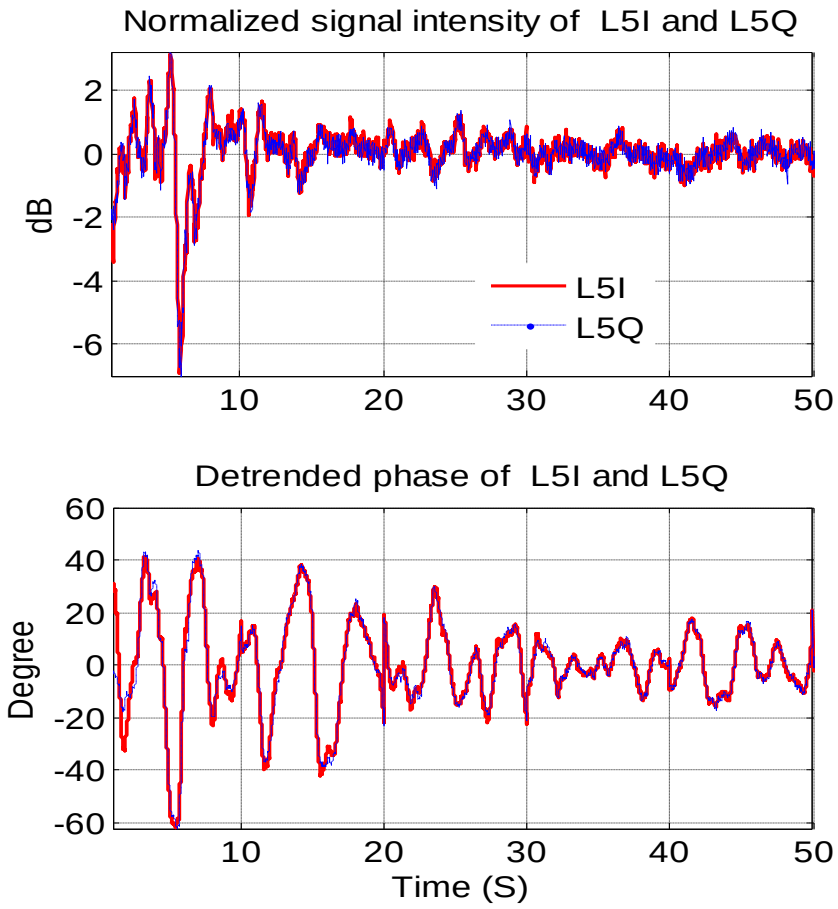

Figure 6.6: Amplitude and phase scintillation on L5I and L5Q.

Figure 6.7 shows the normalized signal intensity time history plot of the four scintillation events on PRN 25. The first three subplots are the results of natural scintillation events while the last subplot shows the artificial scintillation event. Figure 6.8 shows a zoomed in plot of the scintillation event at 14:08:48 on 03/01/2011. From figure 6.8 we can see that the amplitude fluctuation on GPS L2 and L5 are larger than L1 while the trend on all channels is very similar. Strong correlations among different frequency channels can be observed in all four scintillation events. The detrended carrier phase results are plotted in figure 6.9. A fourth order polynomial fitting is used for the carrier detrending [Peng et al.,

2010]. The similarity of phase scintillation among different channels is also evident in the first three natural scintillation events. The fourth subplot is the detrending results for the artificial scintillation which results in small phase scintillation, so the similarity is not clear in this case.

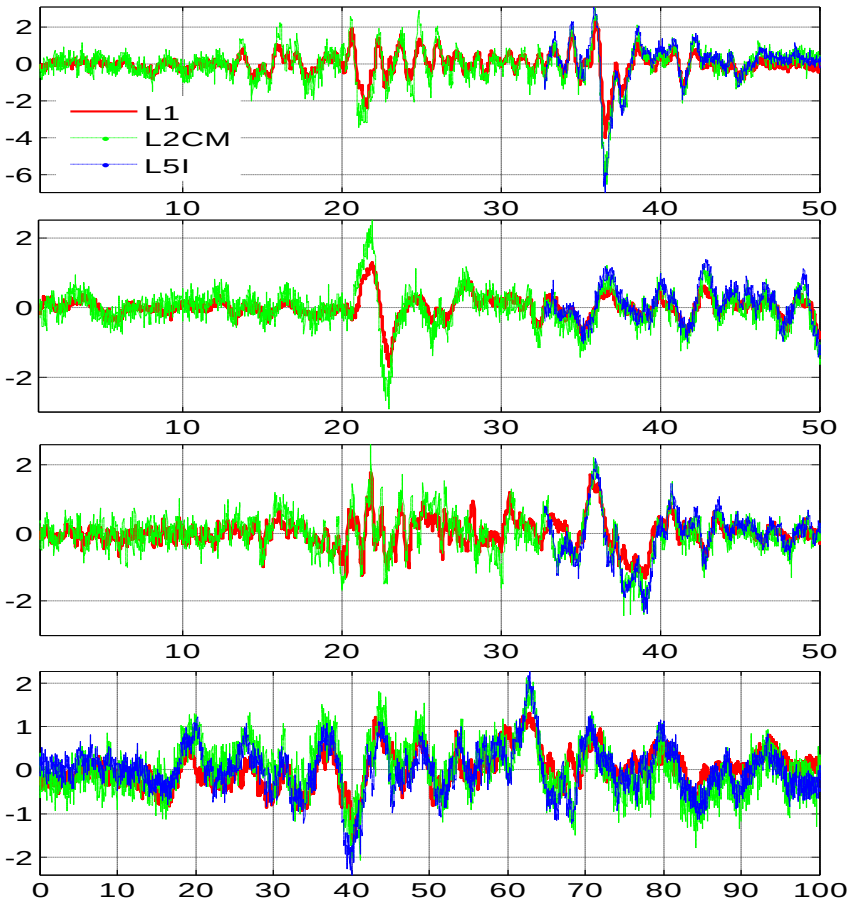

Figure 6.7: Amplitude scintillation on PRN 25.

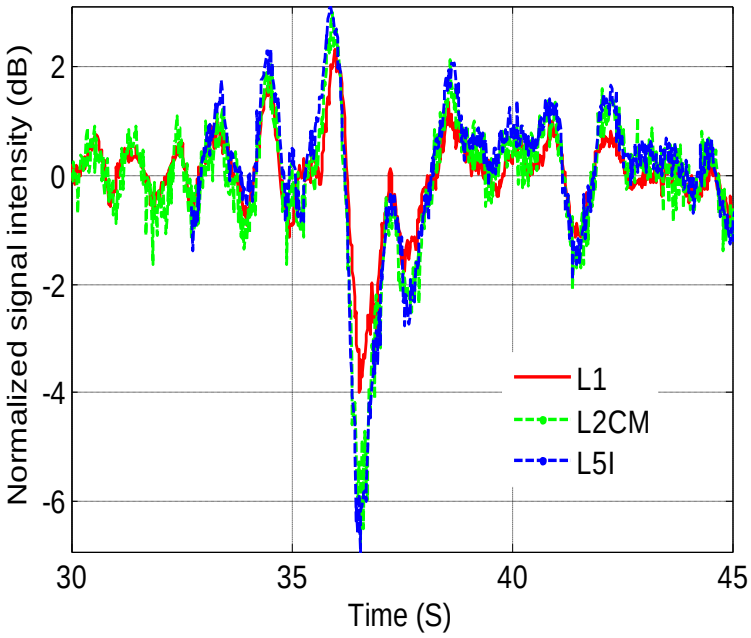

Figure 6.8: Enlarged amplitude scintillation on PRN 25 at UTC time: 03/01/2011, 14:8:48.

The correlation of scintillation among different frequencies is of great importance for future dual frequency (L1 and L5) GPS applications [Seo et al., 2009,2011]. [Seo et al. 2011; El-Arini et al., 2009] showed that deep fading on GPS L1 and L2 was observed by a hardware receiver on three events with a correlation coefficient around 0.7 but the phase scintillation correlation between different channels is unavailable. Highly correlated scintillation between different frequency channels means that the loss of L1 would certainly preceded by the loss of L2 and L5. We computed the correlation coefficient between different channels using the equation:

$$\rho(X, Y) = \frac{E(XY) - E(X)E(Y)}{\sigma_X \sigma_Y} \tag{6.11}$$

where X and Y are time series (could be signal intensity or detrended carrier phase) from two channels, E is the averaging operation, and σ represents the standard deviation of a time series. The correlation coefficients of the three natural scintillation events on PRN

25 captured on 03/01/2011 together with an additional three dual frequency scintillation events are computed and listed in Tables 3 and 4. The amplitude correlation coefficients for those events are near or above 0.7, while the phase scintillation correlation coefficient are above 0.9, indicating highly correlated responses among the three bands.

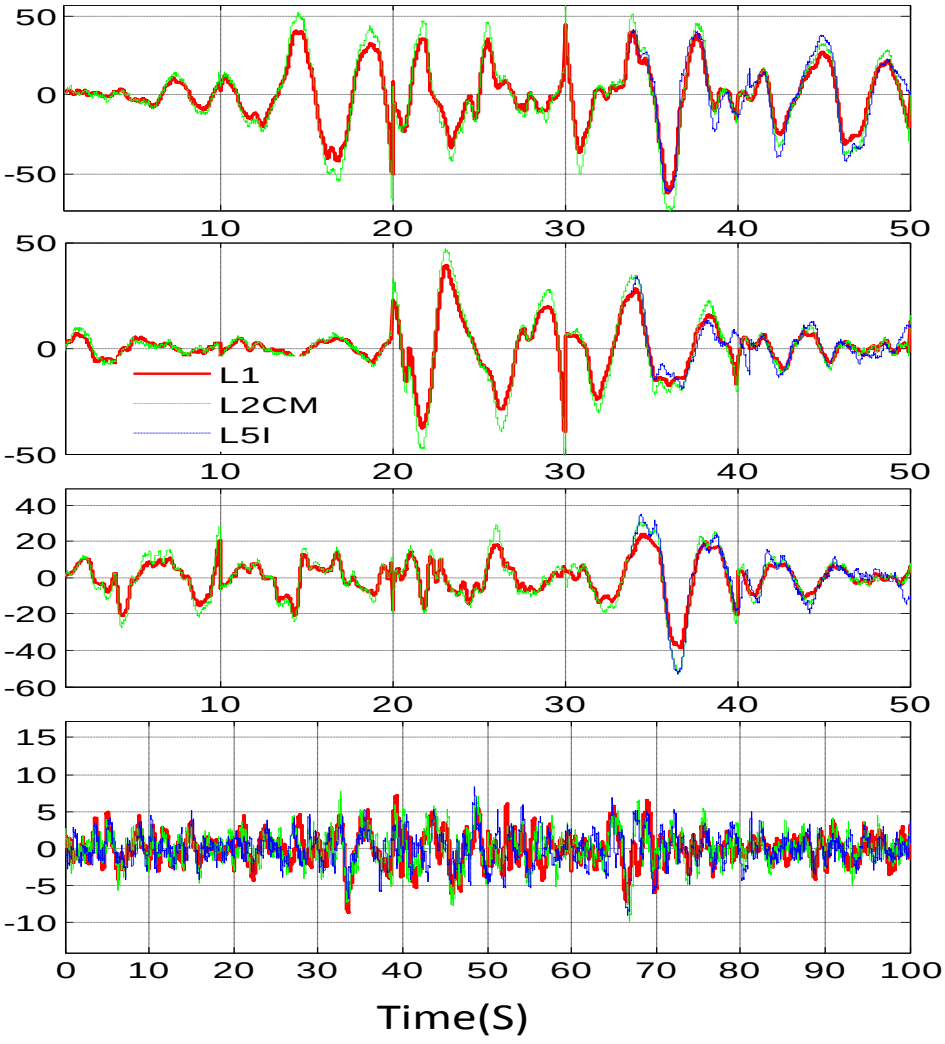

Figure 6.9: Phase scintillation on PRN 25.

The rate of fluctuation is another important scintillation parameter. A higher rate of phase fluctuation indicates larger signal dynamics and imposes a greater challenge on the

carrier phase tracking loop design. The rate of fluctuation can be characterized by the channel de-correlation time τ_0 as defined by the equation [Humphreys et al., 2010a]:

$$R(\tau_0)/R(0) = 1/e \tag{6.12}$$

where R is the auto-correlation of $x(t)$ which can be the signal intensity or the de-trended carrier phase.

Figure 6.10 shows the auto-correlation function for all three bands of PRN25 on 03/01/2011 at 14:08:48UTC. The function is computed using 200 seconds of data. The de-correlation times of the three signals for the three natural events are listed in Table 6.6. Smaller amplitude de-correlation time which indicates a faster fluctuation rate appear to be associated with a larger S_4 index. Although the amplitude de-correlation times on three bands are close to each other, the de-correlation time of L5 is slightly larger than L1 and L2 in all three events.

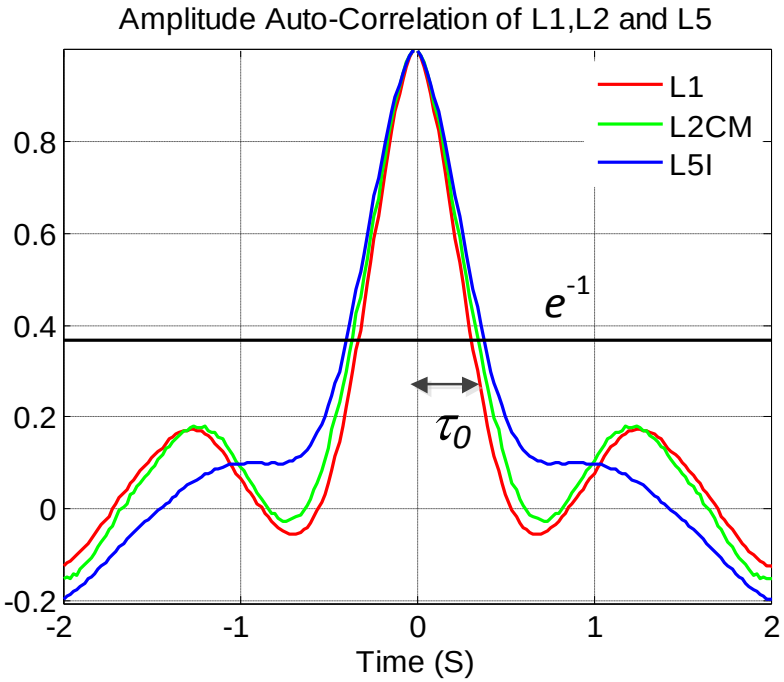

Figure 6.10: Amplitude auto-correlation on PRN 25 0n 03/01/2011, 14:08:48UTC.

Figure 6.11 shows the auto-correlation of the phase scintillation results. 200 seconds of data is used to compute the auto-correlation. Table 6.7 provides the de-correlation times for the three natural scintillation events. The de-correlation times of the three signals are quite close in all three events.

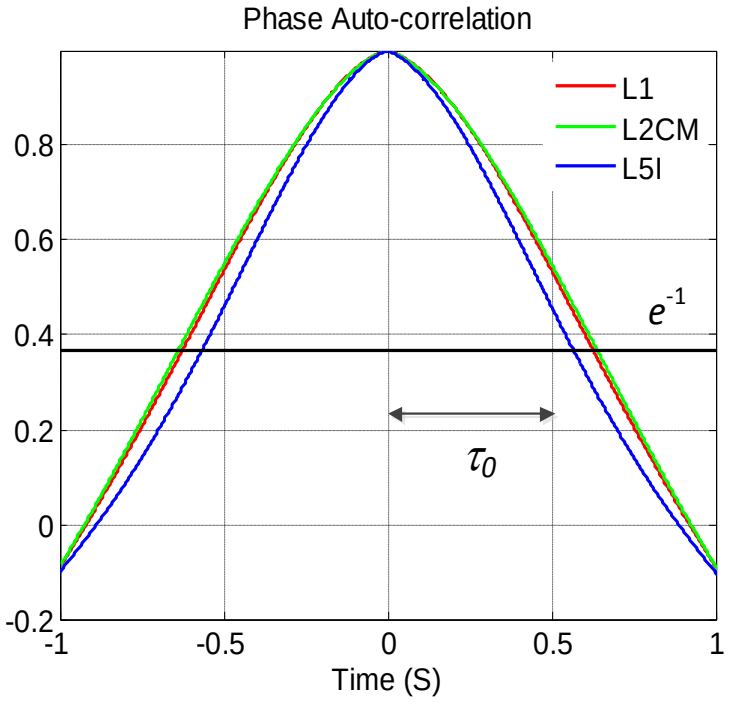

Figure 6.11: Amplitude auto-correlation on PRN 25 0n 03/01/2011, 14:08:48UTC.

In order to explore the scintillation time delay between different channels, the cross correlation between different channels are also computed for both phase and amplitude scintillations. Figure 6.12 shows the amplitude cross correlation between L1 and L2 and between L1 and L5. Figure 6.13 shows the cross correlation of phase scintillation between L1 and L2 and between L1 and L5. The peak values for both amplitude and phase scintillation

and among all channels occur near zero displacement time which means there is a nearly simultaneous amplitude and phase scintillation among L1, L2 and L5.

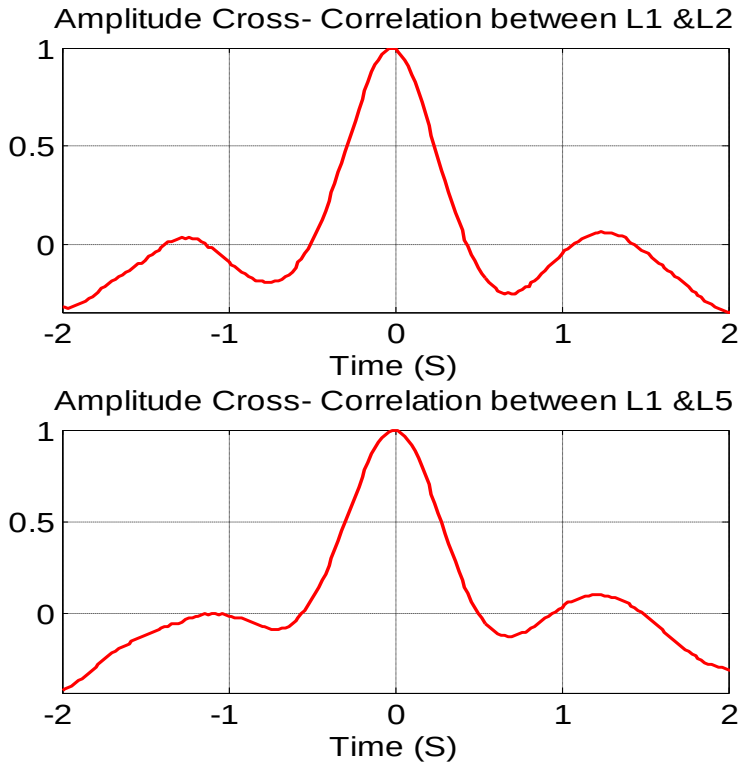

Figure 6.12: Amplitude cross-correlation on PRN 25 on 03/01/2011 at 14:08:48UTC.

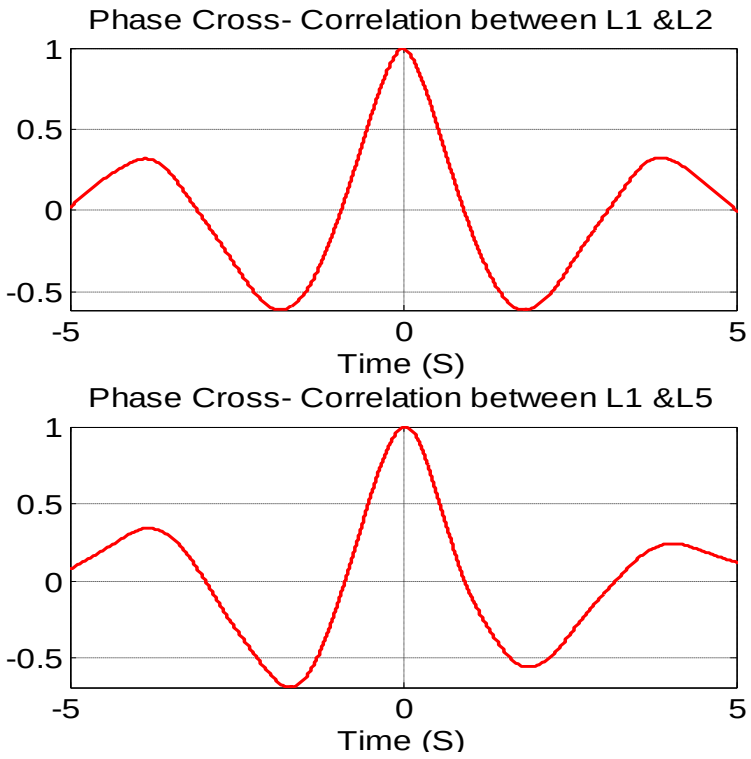

Figure 6.13: Phase cross-correlation on PRN 25 on 03/01/2011 at 14:08:48 UTC.

6.6 Consideration on Phase and Amplitude De-trend

The process of de-trending used in estimation of scintillation indices is to separate scintillation from noise, multi-path and other impacts. In recent years, researchers have discovered several significant problems in de-trending phase and amplitude data for GPS signals.

Forte [Forte et al., 2008] has shown the problem of using fix cut-off frequency filter in data de-trending can result in high phase scintillation with low intensity scintillation as the cut-off frequency is not appropriate to the actual plasma dynamics. He also shows a large decrease in the phase scintillation index by increasing the cut-off frequency from 0.1 to 0.3 Hz for a particular data set. In the paper by [Zhang et al., 2012], the effect of the

tracking loop to the phase scintillation is also analyzed which confirms that the filter used in the PLL may change the pattern of the phase scintillation. In the paper by [AJ], a phase compensation method is proposed to cancel out the impact of the PLL by combine the loops phase error with the carrier NCO output as shown in figure 6.14. However, the phase error of the tracking loop contains both scintillation information and the thermal noise. So this method would work for strong scintillation events, but the effect on the de-trending results is not clear for our data with median scintillation.

De-trending problems with signal intensity or the S_4 index have been detailed in[Materassi et al., 2007]. They point out that the current method to estimation S_4 index is valid only when the signal is stationary. In our case, a stationary antenna is used for the data collection. A high stability OCXO is also used as the reference for the USRP2 RF front end. The impact of the filter in the tracking loop is also minimized by using a wide-band filter with 15Hz noise bandwidth in the PLL. The satellite (PRN 25) was at high elevation angle during the data collection, so the impact of multi-path are also minimized in the analysis. As far as the current method is concerned, it is thought that there is not a problem with the method finding T and p.

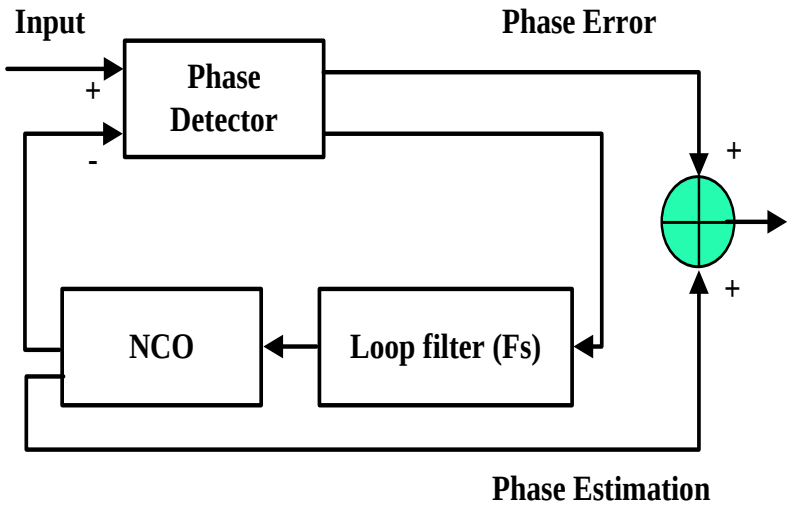

Figure 6.14: Phase compensation method for the PLL loop.

Table 6.1: Scintillation events with IF sample records Date UTC

Date	UTC	PRN	S4(L1)	C/No(dB-Hz)
2010-07-19	23:25:30	25	0.2	52
2011-02-14	23:10:16	32	0.3	52
2011-02-15	12:18:37	12	0.4	53
2011-02-05	01:25:58	20	0.4	50
2011-02-18	14:37:46	29	0.2	50
2011-02-18	09:55:52	27	0.3	52
2011-03-01	13:57:28	29	0.2	52
2011-03-01	14:08:48	25	0.5	50
2011-03-01	13:06:56	25	0.2	54
2011-03-01	12:42:29	25	0.2	55
2011-04-06	13:22:50	21	0.3	50
2011-04-06	13:35:46	21	0.3	50
2011-04-06	13:47:31	21	0.2	50
2011-04-06	15:24:38	21	0.5	49
2011-04-06	15:24:38	19	0.5	48
2011-04-12	10:07:40	25	0.5	55
2011-05-28	07:50:51	29	0.2	52
2011-05-28	08:07:47	29	0.3	52
2011-05-10	08:57:10	29	0.2	52
2011-05-10	11:18:52	21	0.2	50

Table 6.2: Scintillation at 14:08:48 UTC on 03/01/2011

Carrier	L1	L2	L5
S4	0.5	0.7	0.7
Max(signal fading)(dB)	4	6.8	7.1
Max(σ_ϕ)(degree)	26	33	30
5dB fading interval(s)	N/A	0.26	0.32

Table 6.3: Scintillation at 14:08:48 UTC on 03/01/2011

Carrier	L1	L2	L5
S4	0.5	0.7	0.7
Max(signal fading)(dB)	4	6.8	7.1
Max(σ_ϕ)(degree)	26	33	30
5dB fading interval(s)	N/A	0.26	0.32

Table 6.4: Amplitude scintillation correlation coefficients

Time (UTC)	PRN	S4(L1)	ρ(L1,L2)	ρ(L1,L5)
2011-03-01 14:08:48	25	0.5	0.74	0.72
2011-03-01 12:42:29	25	0.2	0.67	0.71
2011-03-01 13:06:56	25	0.2	0.72	0.67
2011-11-30 17:40:41	25	0.2	0.64	0.60
2011-02-18 14:37:46	29	0.2	0.83	N/A
2011-02-15 12:18:37	12	0.4	0.74	N/A
2011-4-12 10:07:40	25	0.5	0.79	N/A
2011-4-6 15:24:38	15	0.3	0.63	N/A

Table 6.5: Phase scintillation correlation coefficients

Time (UTC)	PRN	S4(L1)	ρ(L1,L2)	ρ(L1,L5)
2011-03-01 14:08:48	25	0.5	0.99	0.90
2011-03-01 12:42:29	25	0.2	0.96	0.86
2011-03-01 13:06:56	25	0.2	0.99	0.82
2011-11-30 17:40:41	25	0.2	0.80	0.78
2011-02-18 14:37:46	29	0.2	0.96	N/A
2011-02-15 12:18:37	12	0.4	0.91	N/A
2011-4-12 10:07:40	25	0.5	0.98	N/A
2011-4-6 15:24:38	15	0.3	0.99	N/A

Table 6.6: Amplitude de-correlation time

UTC	S4(L5)	τ_0(L1)(s)	τ_0(L2)(s)	τ_0(L5)(s)
14:08:48	0.7	0.31	0.34	0.38
12:42:29	0.2	0.36	0.40	0.49
13:06:56	0.17	0.52	0.54	0.60

Table 6.7: Phase de-correlation time

UTC	S4(L5)	τ_0(L1)(s)	τ_0(L2)(s)	τ_0(L5)(s)
14:08:48	0.7	0.62	0.64	0.57
12:42:29	0.2	0.61	0.60	0.57
13:06:56	0.17	0.69	0.70	0.69

Chapter 7

Robust GNSS Receiver Tracking Loop Design

7.1 Chapter Overview

The newly added GPS L5 and L2C civilian signals are parts of the modernization of the GPS system in order to satisfy the increasing demands for improved performance for civilian users. The new signals are designed to provide better interference protection, ionosphere delay correction, multi-access noise, multi-path performance, etc. However those new signals are broadcasting at lower center frequencies which result in stronger ionosphere scintillation impacts than on the L1 signals. It is well known that ionosphere scintillations cause increased carrier tracking error and may lead to receiver loss of lock under severe conditions [Zhang et al., 2010]. The demand for more robust tracking algorithms that mitigate the effects of scintillation is especially important as we enter a new solar maximum period. In addition to the naturally occurring interfering phenomena, the rapid

advancement of digital radio technologies and applications continuously push for spectrum resource competitions and lead to increased man made interference. Furthermore, the performance of GNSS degrades in physically challenged environments, such as urban areas and indoors, where only limited satellites maybe in direct view of a receiver. Collectively, these factors have motivated the development of a multiple-frequency, multi-constellation GNSS receiver with a robust vector-based tracking mechanism discussed in this paper.

GPS receiver and they are also the most vulnerable parts of a receiver. The traditional scalar tracking loop (STL) processes signals from each satellite separately. Specifically, a Delay Lock Loop (DLL) is used to track the code phase of the incoming pseudorandom code and a carrier tracking loop, such as a Frequency Lock Loop (FLL) or a Phase Lock Loop (PLL), is used to track the carrier frequency or phase. The tracking results from different channels are then combined to estimate the navigation solutions. The performance of a STL is limited by the filter coefficients, such as the orders and the noise bandwidths of the filters. A filter with wider noise bandwidth can provide better dynamic performance, but perform poorly with weak signals, while a narrow band filter works well for weak signals, but loses the dynamics and requires a reference clock with high stability. Another drawback of the STL is that it neglects the inherent relationship between the navigation solutions and the tracking loop status. In that sense, a STL is more like an open loop system and provides poor performance when scintillation, interference, or signal outages occur.

The vector tracking loop (VTL) provides a deep level of integration between signal tracking and navigation solutions in a GNSS receiver [Spilker 1996] and results in several important improvements over the traditional STL. The most notable advantage of the VTL is the increased interference immunity, and there are some other benefits, such as robust dynamic performance, the ability to operate at low signal power and bridge short

signal outages [Spilker 1996]. Several different implementation architectures of the VTL are given in [Lashley et al., 2009; So et al., 2010; Won et al., 2011]. In [Lashley et al., 2009], extensive testing has been done to verify that the VTL performs better than STL in environments with high dynamics and low signal power. In [So et al., 2010], another architecture of VTL is presented, and the results confirm improved performance for urban applications and the ability of VTL to bridge short time signal outages. Although the current VTL architectures provide several important advantages, they suffer some fundamental drawbacks. The most significant drawback is that failure of tracking in one channel may affect the entire system and lead to loss of lock on all satellites. The other drawback is that errors in the navigation solutions may degrade the accuracy of the tracking loop results.

The VTL implemented in this work contains a vector frequency lock loop (VFLL) and vector delay lock loop (VDLL). The VTL has several important differences compared to the architectures proposed in [Lashley et al., 2009; So et al., 2010; Won et al., 2011]. The first modification is that the VTL is used to assist the STL instead of completely replacing the STL, as in [So et al., 2010; Won et al., 2011]. The VTL is similar to the tightly coupled GPS/INS system, as the estimated platform dynamics are fed back to the tracking loop. The second modification is that a robust adaptive Kalman filter is used to improve the stability of the VTL. The third improvement of the VTL is that a real-time receiver autonomous integrity monitoring (RAIM) algorithm has been developed to prevent the error of one channel from spreading into the VTL. In this software based receiver, the RAIM is used to check the possible fault in the pseudorange, the pseudorange rate, and the signal amplitude. As a result, the VTL can prevent the failure of one channel from spreading into the entire tracking loop. In the meantime, fault channels can make use of information from all healthy channels. Therefore, this architecture combines the advantages of both VTL and STL.

The chapter presents the implementation of the new VTL algorithms in detail. Three different data sets are used to compare the performance of the VTL with STL: real GPS raw RF data with the signal of one satellite being masked for a long interval, 45 minutes of strong scintillation RF data collected at Ascension Island during the last solar maximum, and high dynamic data collected from the GPS simulator with long intervals of signal outage. The results confirm that the new VTL provides an improved tracking performance over the STL under strong scintillation and signal outages. The VTL can keep lock on the signal within a maximum of two hours of signal outage if the position of the receiver can be estimated with an accuracy of less than 300 meters (one C/A code chip).

7.2 STL Based Tracking Loop

The down converted GPS signal from a satellite can be represented by the following equation:

$$s(t) = \sqrt{2P_s}C(t-\tau)D(t-\tau)\cos[2\pi \times (f_{IF} + f_D)t + \phi_0] \tag{7.1}$$

where P_S is the signal power, $C(t)$ is the pseudorandom code, $D(t)$ is the navigation message data bits, τ is the propagation time from the satellite to the receiver, f_{IF} is the nominal intermediate frequency, f_D is the Doppler frequency,and ϕ_0 is the initial carrier phase.

The main task of the receiver is to demodulate the navigation messages from the signal and compute the position, velocity, and time (PVT) solutions of the receiver. To achieve this objective, a typical GNSS receiver makes use of a DLL to estimate the code phase of the incoming signal in order to generate a locate replica to remove the pseudorandom code. Carrier tracking loops are implemented to keep tracking the carrier of the incoming signal.

The measurement from the code tracking loop provides the pseudorange information,while the measurement from the carrier tracking loop provides the pseudorange rate information or the change of pseudorange. The tracking results of all satellites are then combined to estimate the user PVT solutions. A typical STL receiver structure is shown in figure 7.1.

Traditionally, the tracking loops of all satellites are working separately and the navigation solutions are only based on current measurements. So the traditional STL acts more like an open loop system as the navigation results are not fed back to the input of the tracking loop. The information from other satellites is not taken into account in the tracking loop. As a result, the STL provides poor performance because of interference and signal outages. The GPS civilian signals are vulnerable because of its low signal power, short wavelength and open signal structure. A robust receiver architecture is of practical importance to the wider application of GPS system, especially in regard to life-saving applications.

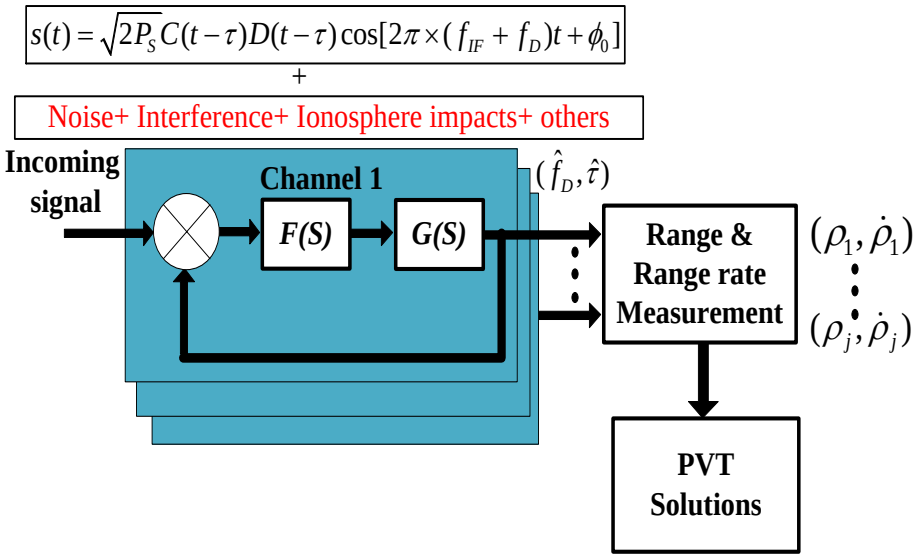

Figure 7.1: STL based receiver architecture.

7.3 VTL Architecture

The VTL differs from the traditional STL in that the task of navigation solutions, code tracking and carrier tracking loops for all satellites are combined into one loop. The center part of a VTL is the Kalman filter which provides an optimal estimation of signal parameters for all satellites in view and user PVT solutions based on both current and previous measurements from all satellites.

The concept of VTL was first described in [Spilker 1996], where a vector DLL algorithm is proposed which combines channel tracking and navigation solutions. Theoretical derivation of the noise performance and improvements and other advantages are also addressed. A more detailed implementation of the VTL can be found in [Lashley et al., 2009] which further verified that VTL provides better performance for weak signals and improves the dynamic performance of GPS receivers. [Won et al., 2011] verified the VTL implementation benefits in the interference environment over that of a traditional architecture. [So et al., 2011] details the implementation of VTL in a pseudolite system. Another implementation for the VTL is described in [Won et al., 2011]. All current results show that VTL can improve the performance of GPS receivers.

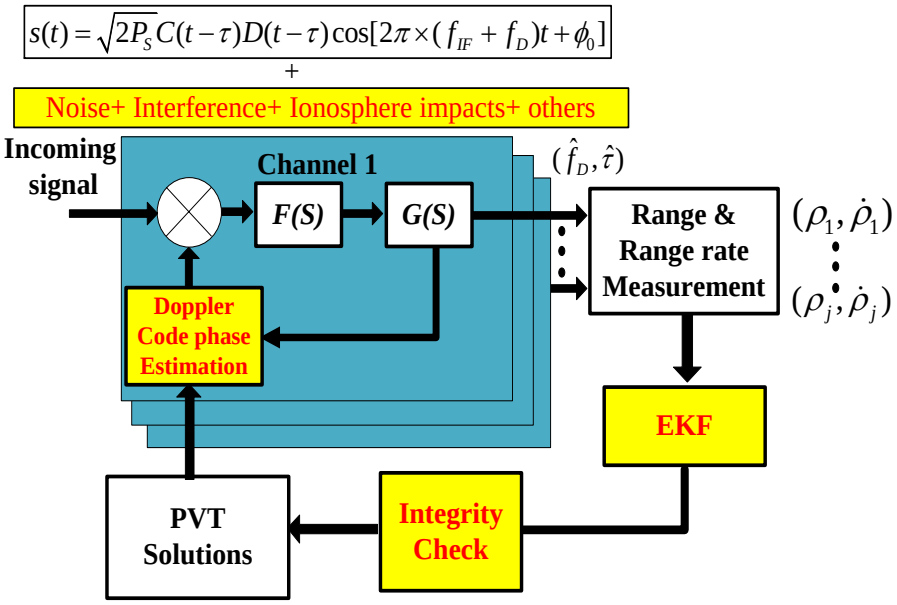

Figure 7.2: VTL assisted tracking loop.

The implementation of the VTL presented in this paper is different from the VTL implemented in [Lashley et al., 2009; So et al., 2010; Won et al., 2011] in several aspects. In this work, the VTL is used to assist the STL, similar to a tightly coupled GPS/INS system, while in the work [Lashley et al., 2009], the VTL is fully responsible for the code phase and Doppler estimation. The state vector of this VTL is different from the VTL [Lashley et al., 2009] as well. The PVT states of the receiver are used as the state vector of the Kalman filter, while in [Lashley et al., 2009], the error of the PVT states are used. The gist of the VTL is an extended Kalman filter (EKF) which estimates the PVT of the receiver. The Doppler frequency can be estimated by the relative motion between the receiver and user, while the code phase can be estimated by the distance between the receiver and user. The error in the pseudorange measurement can be modeled as a Gaussian distribution with a mean between -5m and 5m [Parkinson et al., 1988]. So small time varying errors exist in the estimated Doppler frequency and code phase of the VTL. The STL is then used to track

the small residual errors between the outputs of the VTL and the incoming signal. Because the dominant dynamic component of the receiver is estimated by the VTL, the STL can provide an improved performance compared to that of the STL. When one channel experiences interference or signal outages in the VTL, the information from other satellites can be used estimate the status of this channel. The integrity check algorithms are used to detect the possible error in each channel to prevent the spreading of the error into the rest of the VTL. Figure 7.2 shows the structure of the VTL assisted STL.

7.3.1 Summary of Kalman Fitler Based PVT Solutions

The VTL is implemented in a multi-frequency software based receiver [Peng et al., 2010]. All satellites are tracked in parallel and the results from all satellites in view are processed together with the EKF filter. However, in the work by [Lashley et al., 2009], the results from different satellites are processed sequentially. The PVT estimations of the receiver are used as the states of the Kalman filter. The position and velocities are in a ECEF coordinate frame.

The discrete time Kalman filter provides estimation of the states of a linear system based on both current and previously observed measurements. Given a system dynamic equation, the state space equation of the system is modelled as:

$$X_{k+1} = \Phi X_k + w_k \tag{7.2}$$

$$Z_{k+1} = H X_k + v_k \tag{7.3}$$

where k: is the current step; $X_k \in \mathbb{R}^n$; $w_k \in \mathbb{R}^n$; $Z_k \in \mathbb{R}^m$; $v_k \in \mathbb{R}^m$;

A nonlinear system defined below can be linearized around the current estimation:

$$X_{k+1} = f(X_k) + w_k \tag{7.4}$$

$$Z_{k+1} = h(X_{k+1}) + v_{k_1} \tag{7.5}$$

The transformation matrix can be computed based on the Jacobian matrix:

$$\Phi(i, j) = \frac{\partial f_i}{\partial x_j} \tag{7.6}$$

$$H(i, j) = \frac{\partial h_i}{\partial x_j} \tag{7.7}$$

The Kalman filter algorithms used in the linear system can be extended to the nonlinear system via the extended Kalman fitler (EKF) approach [Brown et al., 1997].

The GPS receiver system is a nonlinear system and can be represented by equations (7.4) and (7.5). A linearized second order system is used in this paper. We define the states of the GPS receiver measurements as:

$$X = [x \quad \dot{x} \quad y \quad \dot{y} \quad z \quad \dot{z} \quad \tau \quad \dot{\tau}]^T \tag{7.8}$$

$[x, y, z]$: receiver position in ECEF;

$[\dot{x}, \dot{y}, \dot{z}]$: receiver velocity in ECEF;

$[\tau, \dot{\tau}]$: receiver clock bias and drift;

The state transformation matrix is defined as:

$$\begin{pmatrix} \Gamma & 0_{2\times2} & 0_{2\times2} & 0_{2\times2} \\ 0_{2\times2} & \Gamma & 0_{2\times2} & 0_{2\times2} \\ 0_{2\times2} & 0_{2\times2} & \Gamma & 0_{2\times2} \\ 0_{2\times2} & 0_{2\times2} & 0_{2\times2} & \Gamma \end{pmatrix}_{8\times8}, \Gamma = \begin{bmatrix} 1 & T \\ 0 & 1 \end{bmatrix} \tag{7.9}$$

where T is the time interval between two adjacent navigation solutions. The receiver state values are initialized using reasonable estimates. The measurement states of the EKF are the pseudoranges and pseudorange rates of all satellites in view:

$$Z = [\rho^1 \dot{\rho}^1 \ldots \rho^N \dot{\rho}^N]^T \tag{7.10}$$

where N is the total number of satellites in view. The pseudorange between the user and the kth satellite is:

$$\begin{aligned} \rho^k(t) &= \sqrt{(x^k(t) - x_u(t)) + (y^k(t) - y_u(t)) + (z^k(t) - z_u(t))} \\ &+ C(\delta_u(t) - \delta^k(t)) + I^k(t) + T^k(t) + \varepsilon^k(t) \end{aligned} \tag{7.11}$$

where: $\delta_u(t)$ is the user clock, $\delta^k(t))$ is the satellite clock error, $I^k(t)$ is ionosphere error , $T^k(t)$ is the troposphere error, and $\varepsilon^k(t)$ is the error of all other factors.

The pseudorange rate can be obtained by taking the derivative of the pseudorange equation. We can get:

$$\begin{aligned} \dot{\rho}^k(t) &= (V^k - V_u) \bullet G + C \times (\dot{\delta}_u(t) - \dot{\delta}^k(t)) \\ &+ \dot{I}^k(t) + \dot{T}^k(t) + \dot{\varepsilon}^k(t) \end{aligned} \tag{7.12}$$

where

V^k : is the speed vector if kth satellite in ECEF frame;

V_u : is the user speed vector in ECEF frame;

G : is the satellite geometry vector;

The observation matrix is obtained by linearizing equations (7.11) and (7.12). The

measurement equation is then given by

$$Z = \bar{Z} + H \times (X - \bar{X}) \tag{7.13}$$

$$H_{2N\times 8} = \begin{bmatrix} h_1^x & 0 & h_1^y & 0 & h_1^z & 0 & -1 & 0 \\ 0 & h_1^x & 0 & h_1^y & 0 & h_1^z & 0 & -1 \\ \vdots & & & \vdots & & & \vdots & \\ & h_N^x & & h_N^x & & h_N^x & 0 & -1 \end{bmatrix} \tag{7.14}$$

where

$\bar{Z}$: is the estimation of Z and $\bar{Z} = h(\bar{X})$;

$\bar{X}$: is the estimation of X;

$h_k^x = -(x^k - x_u)/r, \quad h_k^y = -(y^k - y_u)/r, \quad h_k^z = -(z^k - z_u)/r,$

and $r = \sqrt{(x^k(t) - x_u(t)) + (y^k(t) - y_u(t)) + (z^k(t) - z_u(t))}$, which is the real range between the satellites and user.

Equation (7.13) provides the relationship between the measurement errors of Z with the estimation errors of X. The measurement errors are used in the measurement update step of the EKF to refine the estimation of X [Bar-Shalom et al., 2001]. Assuming measurement errors for signals from different satellites are uncorrelated, the measurement error covariance matrix is then given by:

$$R = \begin{bmatrix} \delta_1 & 0 & 0 \\ 0 & \vdots & 0 \\ 0 & 0 & \delta_n \end{bmatrix}_{2n\times 2n}, \qquad \delta_n = \begin{bmatrix} \delta\rho_n^2 & 0 \\ 0 & \delta\dot{\rho}_n^2 \end{bmatrix} \tag{7.15}$$

where

N: is the number of satellites in view;

$\delta\rho_n^2$: is the variance of pseudorange;

$\delta\dot{\rho}_n^2$: is the variance of pseudorange rate;

$$
\begin{aligned}
Q &= \begin{bmatrix} u & 0_{2\times2} & 0_{2\times2} & 0_{2\times2} \\ 0_{2\times2} & u & 0_{2\times2} & 0_{2\times2} \\ 0_{2\times2} & 0_{2\times2} & u & 0_{2\times2} \\ 0_{2\times2} & 0_{2\times2} & 0_{2\times2} & \beta \end{bmatrix}_{8\times8} \\
u &= \begin{bmatrix} S_p\frac{T^3}{3} & S_p\frac{T^2}{2} \\ S_p\frac{T^2}{2} & S_pT \end{bmatrix}, \quad \beta = \begin{bmatrix} S_c\frac{T^3}{3} & S_c\frac{T^2}{2} \\ S_c\frac{T^2}{2} & S_cT \end{bmatrix}
\end{aligned} \tag{7.16}
$$

where

S_P: is the position noise spectrum density;

S_C: is the clock noise spectrum density;

The initial estimation error matrix is defined:

$$
\begin{aligned}
\bar{P}_0 &= \begin{bmatrix} \delta X & 0_{2\times2} & 0_{2\times2} & 0_{2\times2} \\ 0_{2\times2} & \delta Y & 0_{2\times2} & 0_{2\times2} \\ 0_{2\times2} & 0_{2\times2} & \delta Z & 0_{2\times2} \\ 0_{2\times2} & 0_{2\times2} & 0_{2\times2} & \delta\tau \end{bmatrix}_{8\times8} \\
\delta X &= \begin{bmatrix} \delta X^2 & 0 \\ 0 & \delta\dot{X}^2 \end{bmatrix}, \delta Y = \begin{bmatrix} \delta Y^2 & 0 \\ 0 & \delta\dot{Y}^2 \end{bmatrix}, \delta Z = \begin{bmatrix} \delta Z^2 & 0 \\ 0 & \delta\dot{Z}^2 \end{bmatrix}, \delta t = \begin{bmatrix} \delta t^2 & 0 \\ 0 & \delta\dot{t}^2 \end{bmatrix}
\end{aligned} \tag{7.17}
$$

where

$\delta X, \delta Y, \delta Z$: standard deviation of initial position error;

$\delta\dot{X}, \delta\dot{Y}, \delta\dot{Z}$: standard deviation of initial speed error;

$\delta t, \delta\dot{t}$: standard deviation of initial clock and clock drift error.

A flowchart of the implementation of the EKF-based vector tracking algorithms is also included in appendix. The loop starts by an initial estimation of the user PVT solutions.

The PVT states are updated by the pseudorange and pseudorange rate measurements. The EKF estimates navigation solutions based on both the previous and current measurements.

7.3.2 Adaptive Kalman Filter Based VTL

The limitation in applying the Kalman filter for practical problems is that the prior statistics [LaViola 2003; Hide et al., 2003; Jwo et al., 2008] of the dynamic system and measurement model are assumed to be available. However, this assumption is not always the case as the GPS navigation system is a dynamic system. The accuracy of navigation solutions are affected by the ionosphere, interference, multipath, satellite geometry, etc. If the initial values of the system do not reflect the real model, the Kalman filter estimation results may not be reliable and divergence may occur. So it is desirable to estimate the covariance matrices adaptively. Both unscented Kalman filter (UKF) [LaViola 2003] and the adaptive Kalman filter (AKF)[Hide et al., 2003; Jwo et al., 2008] are variations of EKF filters which estimate the covariance matrices adaptively during run time.

One of the most important advantages of the UKF is that the computation of Jacobian matrix is avoided. However, the parameters in the UKF still require the prior knowledge of the system [LaViola 2003]. For that reason, we will focus on adaptive KF approach in this paper.

The adaptive Kalman filter is another promising method for dynamically adjusting the parameters of the Kalman filter. The basic idea of the AKF is that the expected covariance and the measured covariance of the system parameters should be equal when the Kalman filter estimates are optimal. So the AKF is used to dynamically adjust the covariance matrices of the EKF filter and the covariance matrices are estimated by averaging the real

observations.

Defining the residual of the measurement:

$$r_k = Z_k - H\hat{X}_k = H(X_k - \hat{X}_k) + v_k \tag{7.18}$$

$$E(r_k r_k^T) = HP_kH^T + R \tag{7.19}$$

$$\bar{r} = \frac{1}{N}\sum_{k=1}^{N} r_k \tag{7.20}$$

the measurement noise can be estimated by:

$$\hat{R} = \frac{1}{N-1}\sum_{k=1}^{n}\{(r_k - \bar{r})(r_k - \bar{r})^T - \frac{N-1}{N}H\bar{P}_{k+1}H^T\} \tag{7.21}$$

The estimation of disturbance bias is conducted similarly:

$$X_{k+1} = \Phi X_k + w_k, \quad E(w_k) = 0 \tag{7.22}$$

In defining:

$$q_k = X_{k+1} - \Phi\hat{X}_k = \Phi(X_k - \hat{X}_k) + w_k \tag{7.23}$$

$$\bar{q} = \frac{1}{N}\sum_{k=1}^{N} q_k, \tag{7.24}$$

the estimation of disturbance covariance matrix is:

$$\hat{Q} = \frac{1}{N-1}\sum_{k=1}^{N}\{(q_k - \bar{q})(q_k - \bar{q})^T - \frac{N-1}{N}\Phi\bar{P}_{k+1}\Phi^T\} \tag{7.25}$$

In the EKF, the estimation covariance P matrix is initialized with heuristic estimations. The propagation of the P matrix is independent of the dynamics of the system. The performance of the EKF is significantly dependent on the accuracy of the a posteriori estimation covariance P matrix. As the GPS receiver system is a dynamic system, an adaptive estimation of the P matrix would be preferable to the heuristic approach. In the AKF, the P matrix

is dynamically adjusted based on the measurement outputs. Defining:

$$E(r_k r_k^T) = HP_kH^T + R = C_r \tag{7.26}$$

$$\hat{C}_R = \frac{1}{N}\sum_{k=1}^{N}(r_k r_k^T) \tag{7.27}$$

If P_k provides a good estimation of current covariance, then we should get $\hat{C}_R$ close to C_R. A scale factor for the P_k matrix is defined by (7.28):

$$P_k = \lambda_p \times P_k, \tag{7.28}$$

where $\lambda_p = diag[\lambda_1, \lambda_2, \ldots, \lambda_{2N}]$.

The scale factor of the P_k matrix can be computed by:

$$(\lambda_p)_{ii} = \max\left(1, \frac{tr(\hat{C}_R)}{tr(C_R)}\right) \tag{7.29}$$

$$\bar{P}_{k+1} = \lambda_p(\Phi P_k \Phi + \hat{Q}) \tag{7.30}$$

When $\lambda_p > 1$, which means the current sate error covariance is larger than the expected values, so the values of P matrix need to be increased. When $\lambda_p = 1$, the adaptive Kalman filter deteriorate to the Kalman filter.

The AKF combines the task of navigation solutions and signal tracking. The predicted PVT solutions for next step can be computed by the time update equation based on current state estimations. The tracking loop parameters (Doppler frequency, code phase, and code rate) can be computed based on the relative motion between the satellites and the user and their relative geometric relationships. The user PVT solutions can be computed from equations (7.12)(7.13). The predict user PVT solution is estimated by equation (7.2). In the meantime, the positions of satellites are computed accurately by the broadcasted ephemerides, and the velocity of a satellite is computed by the first order derivatives of

their ephemerides [Zhang et al., 2006]. With all this available information (Doppler frequency, code phase, and code rate), the expected pseudorange and pseudorange rate can be estimated. The pseudorange estimation has a standard deviation of a few meters, so a Hatch filter is used to smooth the pseudorange measurements by incorporating the carrier phase measurement.

Figure 7.3 shows the comparison of the AKF Doppler frequency results with a FLL tracking loop for a nominal satellite during a scintillation event occurring at Ascension Island during the last solar max [Zhang et al., 2010]. This satellite was not affected by scintillation, while several other satellites were affected. We can see that the results of the AKF tracking loop are noisy compared to the scalar FLL tracking loop for this channel. For GPS L1 only receivers, the PVT solutions may contain a large ionosphere delay error and a troposphere error. The error from one satellite will spread into other channels in the VTL loop. The traditional STL provides higher accuracy than the VTL when there is no signal outage. This is because a VTL utilizes information from other satellites to correct the error caused by interference or signal outage in one satellite. In the case shown in Figure 7.3, the majority of the channels are under sub-optimal signal conditions due to the occurrence of a severe scintillation event. These sub-optimal channels lead to larger errors in the overall system estimations, which spilled over to individual channel estimations. Therefore, in order for a VTL to outperform a traditional STL under these types of circumstance, integrity check algorithms are necessary to detect the possible error in a scalar channel. Once an error is detected in a scalar loop, the Doppler and code information from VTL are be used to correct the error in this scalar loop. For other health channels, only the results from the scalar loop are used.

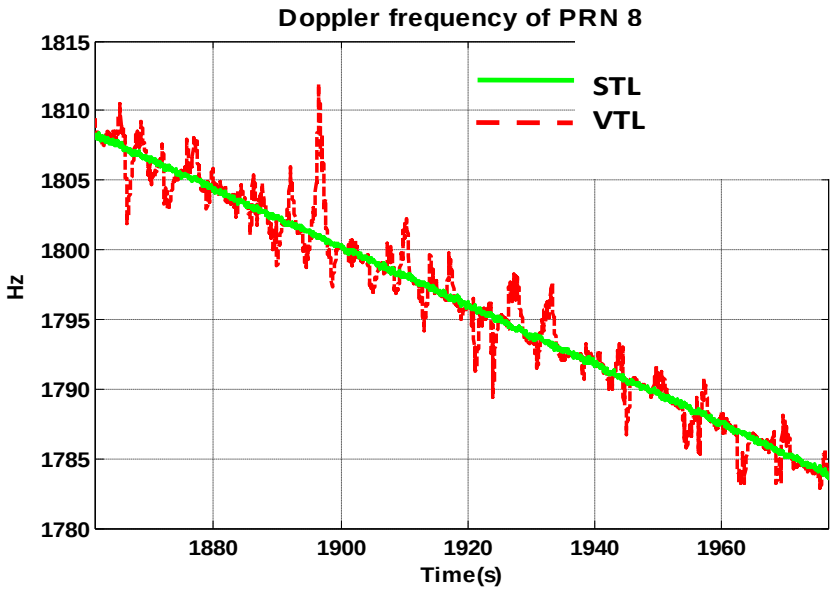

Figure 7.3: AKF-based Doppler frequency estimation from a VTL underperforms a traditional FLL because errors from poor quality channels will affect the signal tracking in an otherwise well-conditioned channel.

7.4 Real-time Receiver Autonomous Integrity Monitoring (RAIM)

The integrity monitoring algorithms implemented in this work deals with the integrity of the tracking loops. The purpose of this work is to handle issues related to interference or GPS signal outage instead of satellite failure or ephemerides error. Here we make the assumption that all satellites are healthy and ephemerides are accurate.

The performance of the VTL strongly depends on the (RAIM) algorithms. When a failure or error is detected in a certain channel, the VTL outputs are used to assist the STL. If the VTL estimation results are in the pull-in range of the STL, the STL can lock the

signal again after the outage and the most computationally expensive re-acquisition can be avoided. Available RAIM approaches can be mainly categorized into two types: the range comparison method (RCM) and the position comparison method (PCM) [Brown et al., 1997]. RCM compares the measured pseudorange with predicted pseudorange, while PCM method compares the position solution based on measurements from all satellites with the solutions obtained from subsets of satellites. In our case, we are focusing on the status of the tracking loop outputs, which are directly related to the pseudorange measurements. Therefore, RCM is selected in this work.

In the RCM method, the range residual is computed by the difference between the pseudorange and the range computed from the user position and the satellite position. The range residual parameter rp is defined as [Parkinson et al., 1988]:

$$r_p = \frac{s\sigma}{\sqrt{N-4}} \tag{7.31}$$

where

s : the sum of squared pseudorange errors(SSE);

σ : the standard deviation of the pseudorange errors;

N : the number of satellites in view;

The suggested threshold based on Monte Carlo simulation for the error detection is $r_D = 8m$, while the isolation threshold is $r_I = 10m$ [Parkinson et al., 1988]. In addition to the pseudorange measurements, the pseudorange rates also contain valuable information for integrity monitoring. As the number of GPS satellites in view is normally around 8 to10, and $\sigma = 0.4$ is suggested in the work for the GPS system [Parkinson et al., 1988]. So we can assume that the pseudorange error s is around 50 meters when the isolation

threshold $r_I = 10m$ by equation (7.31). A fixed value 50m is used as the isolation threshold for pseudorange error.

The second index for the integrity check is the pseudorange rate residual, which is defined by the equation:

$$\triangle\dot{\rho}^k(t) = (V^k - V_u) \bullet G - \hat{f}_D\lambda, \tag{7.32}$$

where

$\hat{f}_D$: is the estimated Doppler frequencey;

λ : is the wavelength;

V^k : is the speed vector if kth satellite in ECEF frame;

V_u : is the user speed vector in ECEF frame;

G : is the normalized direction vector between the user and the satellite;

The receiver tracking loop provides very accurate estimation of Doppler frequency, but it is vulnerable and sensitive to signal outages or interference. So the pseudorange rate residual information can also be useful for receiver integrity monitoring. The analysis of the pseudorange rate residual can be derived from the pseudorange residual analysis directly [Parkinson et al., 1988]. The distribution of the pseudorange rate residuals can be modeled as a distribution with $N-4$ degrees offreedom, where N is the number of satellites in view. The pseudorange rate residuals thresholds are computed from the pseudorange thresholds divided by the carrier wavelength.

$$\begin{aligned} f_D &= r_D/\lambda = 40Hz \\ f_I &= r_I/\lambda = 50Hz \end{aligned} \tag{7.33}$$

In addition to pseudorange and pseudorange rate measurements, a C/N_0 based integrity monitoring method is implemented as well to detect sudden signal outages. The amplitude

of the incoming signal can be estimated by the accumulated results of the tracking loop as the carrier and code are removed. The accumulation of noise results in large variations or standard deviation of the amplitude estimation. So the C/N_0 estimation would be more stable than the amplitude estimation. The algorithms used to compute the C/N_0 is the same as in [Peng et al., 2010]. Based on experience, a value of 25dB-Hz is used as the isolation threshold. If the C/N_0 of a channel is below this value, this channel is then excluded from navigation solution estimation. The results from the VTL are used assist the tracking of this channel.

The VTL(VFLL/VDLL) implemented here is designed to deal with a long interval signal anomaly within the time interval of two hours, which is equal to the ephemerides effective period. As mentioned before, the major drawback of the VTL is that the carrier phase and code phase are dependent on the accuracy of navigation solution. For a GPS L1 only receiver, the magnitude of position estimation error can be as much as tens meters. The accumulation of the estimation error can be molded as a Brownian-motion process [Brown et al., 1997]. The standard deviation of the accumulated error increases linearly with the accumulation time. The accumulation of 50Hz data rate outputs in one second may result in an error in the range of hundred of meters. A large accumulated phase error would not impact the performance of the VFLL as VFLL only tracks the frequency of the signal and neglects the initial phase error. However, the VDLL is very sensitive to the accumulated error. A code phase error of more than one chip would result in no correlation between the local reference PRN code and the incoming signals. The equivalent range error of one chip is around 300 meters for GPS L1 signals. In order to develop a VTL which has the capability to deal with long interval signal outages, code phase estimation within the range of less than one chip code phase error is required.

Fortunately, the error in the accumulated code phase can be corrected by the geometric relationship between the satellites and the receiver if accurate ephemerides are available. Figure 7.4 illustrates the scenario where the signal from one satellite is blocked during time T to $T + \triangle T$, where $\triangle T$ is a large time interval but less than two hours. Assuming at time T, the receiver received a signal from the satellite at time $T - \triangle t_1$, where $\triangle t_1$ is the signal propagation time delay and it is computed accurately by the code tracking loop. After time $\triangle T$, the user should receive a signal from the satellite with time delay $\triangle t_2$ as shown in figure 7.4.

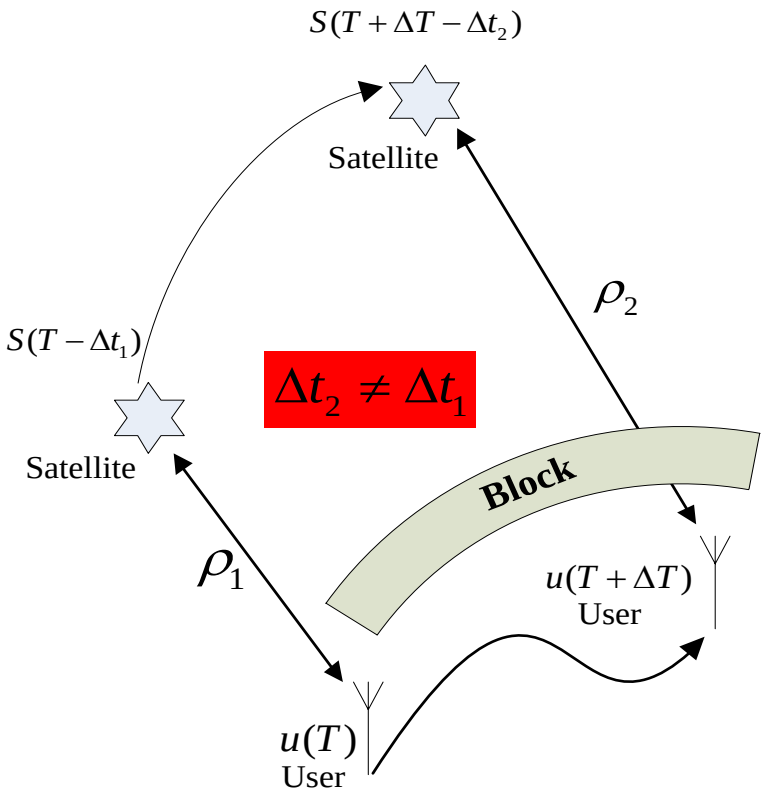

Figure 7.4: Code phase estimation for the VTL.

We should note here that $\triangle t_1$ and $\triangle t_2$ are not equal because the pseudorange between the user and the satellite has changed during this large time interval. The accurate position

of the satellite during this time interval can be computed accurately by the ephemerides. If the user position during this time can be estimated by other satellites or by an inertial system with an accuracy within one C/A code chip (300 meters), then the time delay $\triangle t_2$ can also be estimated to the same level of accuracy. This time delay then can be used to correct the possible accumulated error in the VDLL. The time delay $\triangle t_2$ is computed by solving the nonlinear equation:

$$(S_{[T+\triangle T-\triangle t_2]} - U_{[T+\triangle T]}) \bullet G = C \times \triangle t_2 \tag{7.34}$$

where

$S_{[T+\triangle T-\triangle t_2]}$: satellite position at time $T + \triangle T - \triangle t_2$;

$U_{[T+\triangle T]}$: estimated receiver position at time $T + \triangle T$;

G : is the satellite geometry vector;

C : speed of light;

With accurate estimation of code phase, Doppler frequency and code frequency from the VTL, the tracking loop of the receiver can re-lock onto the incoming signal automatically when the signal outage is over. The remaining part of the paper presents the VTL performance.

7.5 VTL Performance Test

7.5.1 Stationary Receiver With Signal Outages

The first test data set is a GPS L1 data collected with 5MHz sampling frequency using a USRP2 board [Peng et al., 2010]. The data is first processed by the software-based GPS receiver to estimate the signal amplitude, C/A code and carrier information of each satellite

in view. The sudden block of one channel of GPS signal can be achieved by subtracting the tracked signal from the input. In this test, a data set of a 400s interval is collected. The signal on PRN2 is removed during time 100s to 180s and 200s to 250s and 280s to 300s, as shown in the top panel of the figure 7.5.

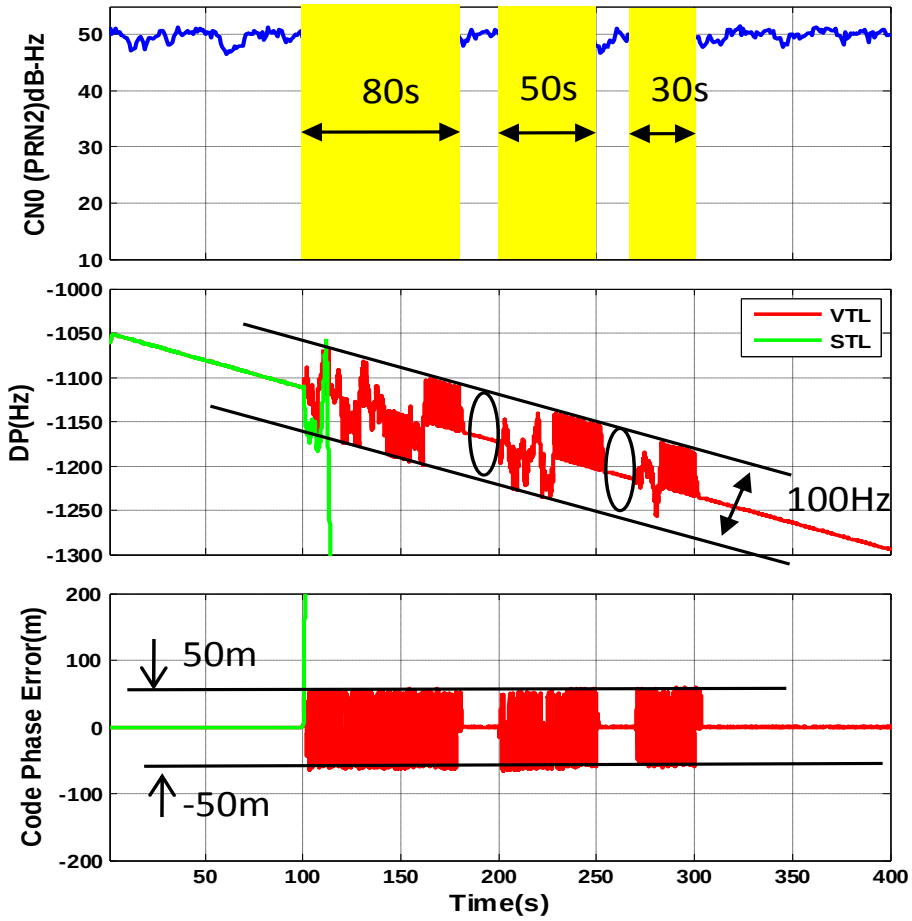

Figure 7.5: Comparisons between VTL and STL performance during multiple signal outages in real data experiment.

The FLL and DLL implemented in the STL have noise bandwidths of 5Hz and 0.1Hz respectively. The coherent integration time is 1ms and the FLL and DLL are updated at a 1000Hz rate. Figure 7.5 plots the corresponding phase and Doppler error. From the

results, we can see that the scalar FLL lost lock of the incoming signal after about 15 seconds of signal outage, while the DLL lost lock in about two seconds. The VTL is used to assist the STL when this satellite is isolated from navigation solution by the integrity check algorithms. As the error of the VTL for both code phase and Doppler frequency are within the pull-in range, the signal is re-locked again automatically when the outages are over, as shown in the figure 7.5. So no signal re-acquisition is needed in the VTL.

7.5.2 Strong Scintillation Data

Ionosphere scintillation has strong impacts on GPS navigation signals propagating through the disturbed medium. The rapid fluctuation of the carrier phase and deep fading of signal amplitude stress the tracking loop of the GPS receiver. Events of receiver loss of lock of GPS signals have been reported in many publications during strong scintillation events [Humphreys et al., 2010].

The raw intermediate frequency (IF) data was collected using a NAVSYS DSR-100 receiver with a Rubidium frequency reference at Ascension Island in the South Atlantic Ocean from 8:45PM to 9:30PM on March 18, 2001 [Zhang et al., 2010]. This 45 minutes of data contains a strong scintillation event with S4 index higher than 1 and signal fading of more than 20 dB. The performance of STL of these signals has be thoroughly studied in the work by [Zhang et al., 2010], which shows loss lock of signals for PRN 4 and PRN 11 which were affected by strong scintillation impacts at low elevation angles.

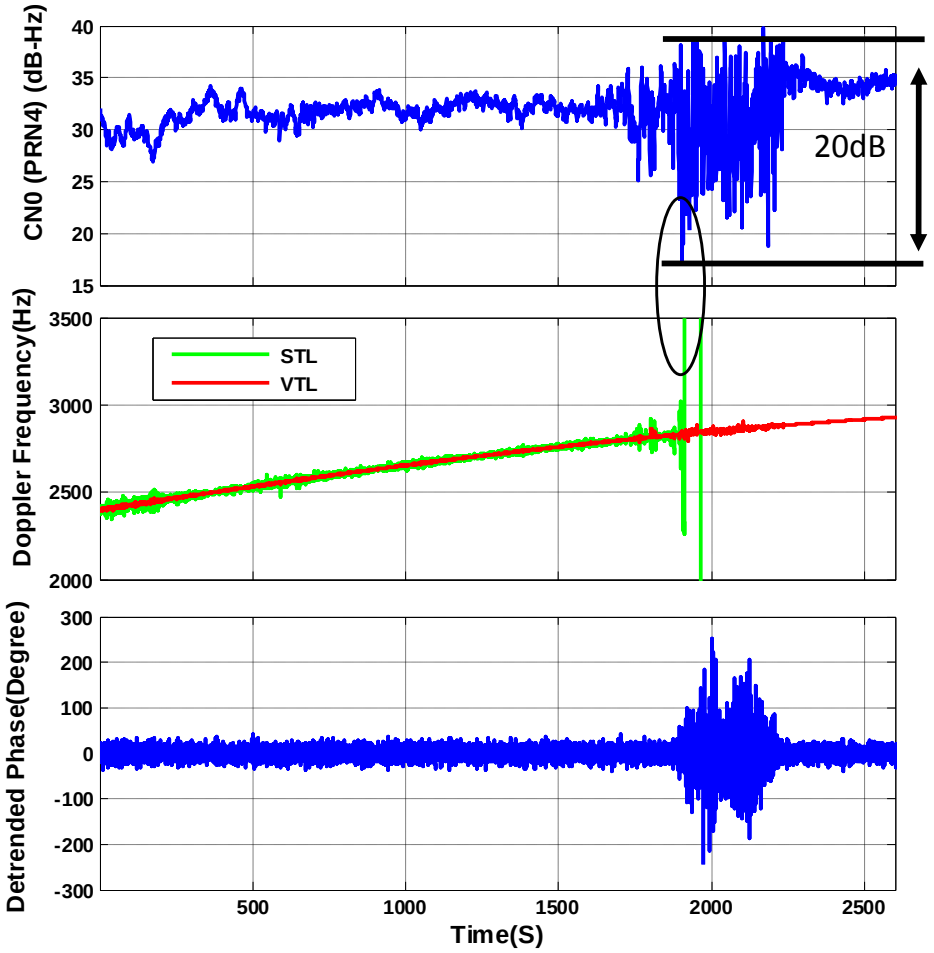

Figure 7.6: Scintillation tracking results of PRN4 using VTL and STL.

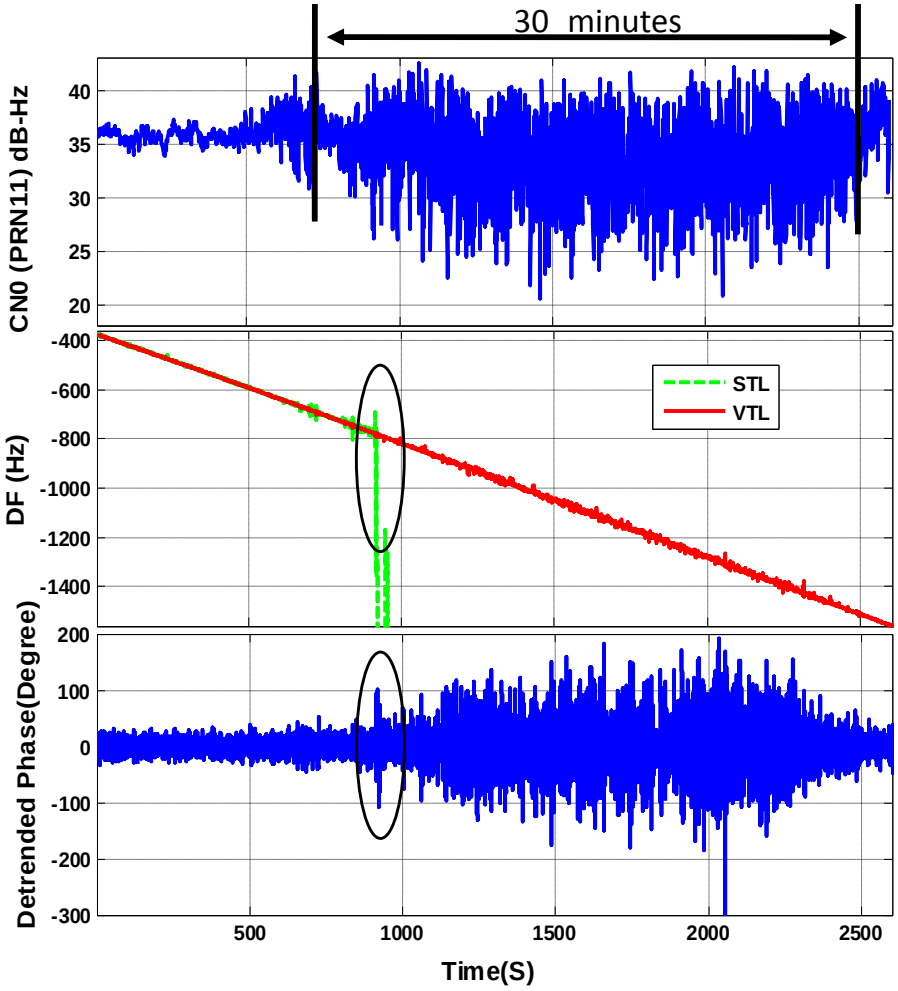

Figure 7.7: Tracking results comparison for PRN11 with VTL and STL.

Figures 7.6 and 7.7 show the C/N_0 and Doppler frequency for both satellites using STL and VTL. PRN4 experienced about 15 dB amplitude fading for about 300s, while PRN11 amplitude fading is about half. The fading of signal amplitude together with the fluctuation of the carrier phase results in loss lock of the tracking loop. Signal re-acquisition is also difficult because of the low C/N_0. The VTL make use of information from other healthy satellites to provide an optimal estimation of the states of satellites with scintillation impacts. The VTL maintains the locking of signals smoothly during the strong scintillation

event. Because of the sparse distribution of the GPS constellation, the scintillation on different satellites is often different in time and level, the VTL provides an excellent solution to withstand scintillation impacts by making use of redundant information.

7.5.3 High Dynamic Scenario With Signal Outages

The previous performance test are based on data collected by stationary receivers. The dynamic performance of the VTL is tested using data generated by a GPS simulator. The GPS simulator simulates a scenario of aircraft which performs an 8g turn together with signal outage on one satellite. The sampling frequency of the raw RF data is set at 5MHz. Figure 7.8 plots the VTL tracking results of the Doppler frequency on all eight satellites in view with one satellite experiencing signal outage (PRN6). The first 100 seconds shows a highly dynamic scenario which results in a rapid change in the Doppler frequency. A STL-based on narrow noise bandwidth loses lock of the signal quickly. A wide band noise filter provides good tracking performance, but the tracking results are contaminated by noise. The VTL provides a good choice for highly dynamic receivers. The dynamic of the platform can be estimated by the VTL; the STL only needs to estimate the residual Doppler frequency.

Figure 7.9 shows signal outages of more than 200s on one satellite. During the signal outage, the STL is assisted by the VTL, so the frequency error is maintained in a small range even when the aircraft is still moving quickly. The VTL tracking loop locked the signal again when the outages have passed.

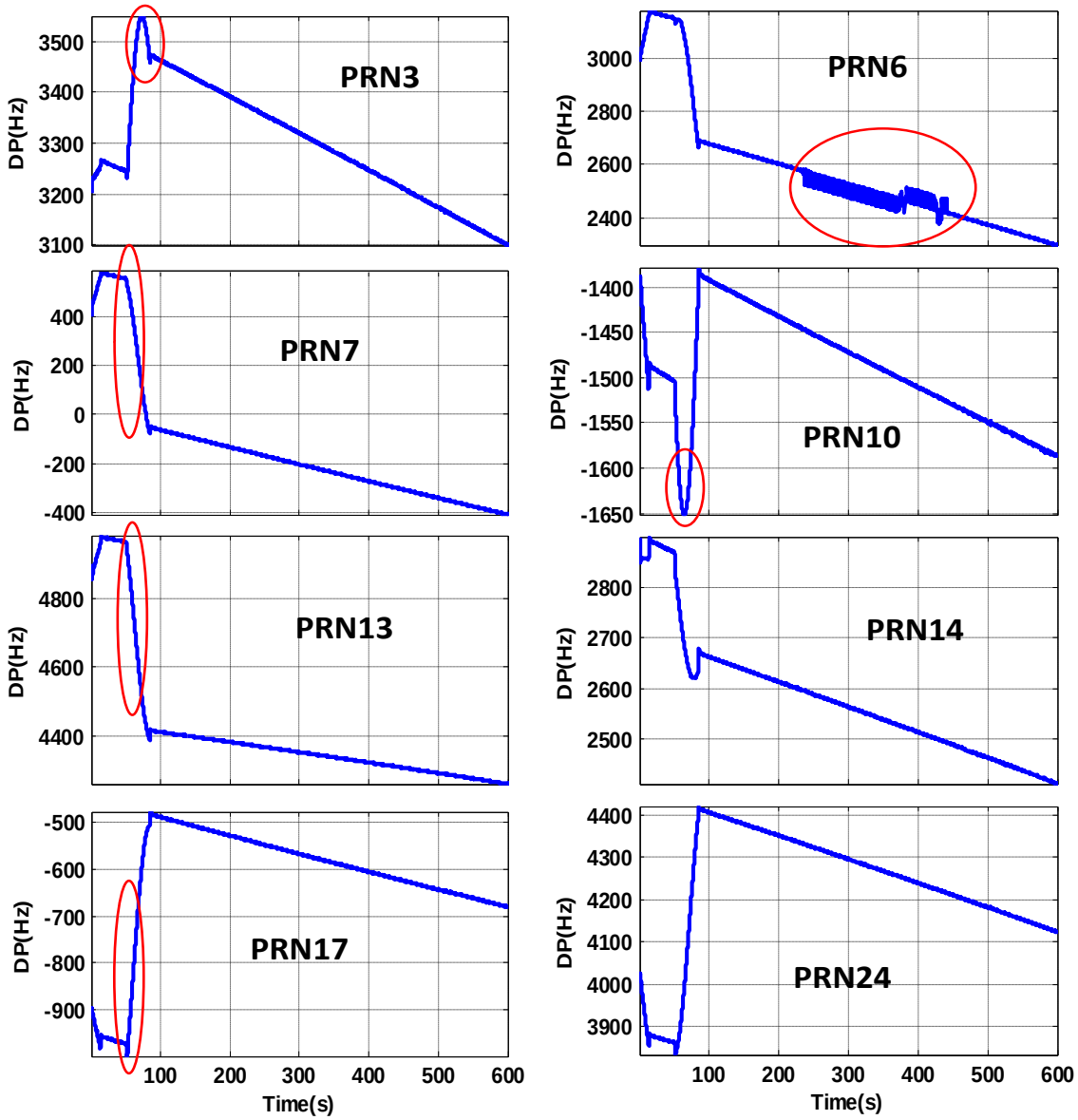

Figure 7.8: Doppler frequency outputs of VTL for high dynamic data tracking.

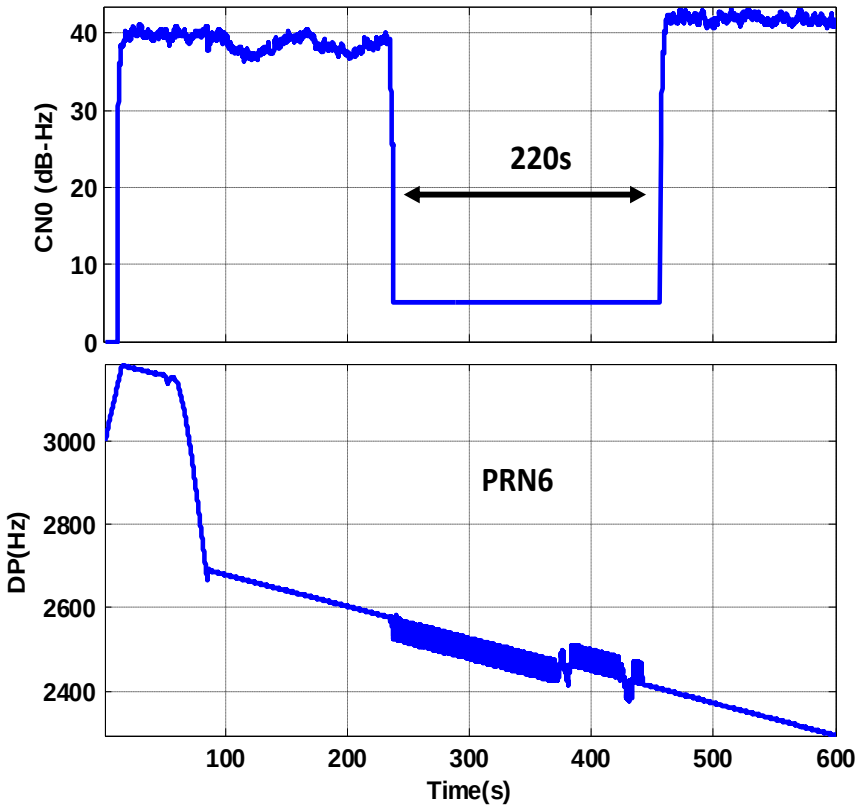

Figure 7.9: VTL tracking results for high dynamic data with signal outages.

7.6 Performance Analysis for Vector Tracking Loop and Scalar Tracking Loops

The Vector tracking loop (VTL) estimates the carrier status of GNSS signals based on robust estimation methods (Kalman filtering) instead of the signal processing methods used in FLL/PLL. To be more specifically, the VTL estimates the Doppler frequency and code phase based on the relative motion between satellites and the user. However, the scalar tracking loop estimates the signal status by processing the digitized incoming signals. So

the advantage of the VTL is that the carrier parameters can be estimated without receiving or processing the incoming signals. The performance of the VTL is depending on the accuracy of the dynamic estimation of both satellite and user positions. The total range error between one satellite and the user can be represented by:

$$\Delta\rho = \delta\rho_{eph} + \Delta\rho_{clk} + \Delta\rho_{ion} + \Delta\rho_{top} + \Delta\rho_{mul} + \xi \tag{7.35}$$

Where: $\Delta\rho_{eph}$ is the ephemerides error, $\Delta\rho_{clk}$ is the clock error of both satellite and user, $\Delta\rho_{ion}$ is the ionosphere error, $\Delta\rho_{top}$ is the troposphere error, $\Delta\rho_{mul}$ is the multipath error, ξ is the error caused by all other factors. Based on the discussion above, the pseudorange budget is given below[Kaplan et al., 2006]:

Table 7.1: GPS Standard Positioning Servise Typical UERE Budget

Segment Source	*Error Source*	*1σ Error(m)*
Space/control	Broadcast clock	1.1
	L1 P(Y)-L1 C/A group delay	0.3
	Broadcase ephemeris	0.8
User	Ionospheric delay	7.0
	Tropospheric delay	0.2
	Receiver noise and resolution	0.1
	Multipath	0.2
System UERE	Total(RSS)	7.1

The user position offset is related to the pseudorange error by the equation:

$$G\Delta P = \Delta\rho \tag{7.36}$$

Where G is the satellite geometry coefficient matrix and ΔP is the user position error vector. The position error can be computed by:

$$\Delta P = (G^T G)^{-1} G^T \Delta\rho; \tag{7.37}$$

$$cov(\Delta P) = (G^T G)^{-1} \sigma^2_{\text{UERE}} \tag{7.38}$$

where σ^2_{UERE} is the pseudorange error std.

The geometry dilution of presision is defined by:

$$GDOP = \frac{\sqrt{\sigma^2_{x_u} + \sigma^2_{y_u} + \sigma^2_{z_u} + \sigma^2_{ct_b}}}{\sigma_{\text{UERE}}} \tag{7.39}$$

The GDOP casts the pseudorange error to user position error. As the VTL estimates the signal code phase based on the user position estimation, so the error in the user position would result in code phase estimation errors. The code tracking loop fails when the code phase estimation contains error is larger than one C/A code chip (300 meters) for GPS L1 signals. The pseudorange error is modeled as Gaussian distribution with standard deviation given by table 7.1. So the user position error can be modeled as Gaussian as well. The standard deviation of the user position error is: $GDOP \times \sigma_{\text{UERE}}$.

During signal outages, the VTL is used to assist the scalar tracking loop. After the signal outages, the estimation results of the VTL are used to initialize the scalar loops. So the probability of failure the receiver tracking loop is depending on the accuracy of VTL code phase estimation. The Q-function or error function of Gaussian distribution is then used to estimate the PDF of code error. The probability of loss lock of the VTL with different GDOP values are listed in table 7.2.

The tracking loop used in the scalar tracking loop is second order PLL with noise band width 15Hz and coherent integration time 1ms. The 1-sigma rule threshold of the PLL

Table 7.2: Probability of loss lock of VTL

GDOP	4	8	16	32
Probability of loss lock	$10^{-13}\%$	$10^{-6}\%$	0.7%	18%

tracking loop is given by:

$$\sigma_{PLL} = \sqrt{\sigma_{tPLL}^2 + \sigma_v^2 + \theta_A^2} + \frac{\theta_e}{3} \leq 15^\circ \tag{7.40}$$

In the meantime, the noise jitter of the PLL is related to the tracking loop parameters by the equation:

$$\sigma_{PLLt} = \frac{360}{2\pi}\sqrt{\frac{B_n}{C/N_0}(1 + \frac{1}{2TC/N_0})} \quad \text{(degrees)} \tag{7.41}$$

The C/N_0 threshold of the tracking loop can be computed (27dB-Hz) by setting $\sigma_{PLL} = 15^\circ$, $T = 1ms$ and $B_n = 15Hz$. The signal processing results further verified this tracking threshold. For satellites PRN4 and PRN11, the C/N_0 can be below 25dB-Hz during the scintillation events. The traditional PLL tracking loop loses lock the signals from PRN4 and PRN11 as shown in the processing results. The STL with optimized parameters (narrow filter bandwidth, longer coherent integration interval) can tracking all satellite in the Ascension Island data[Zhang et al., 2010]. However, the improved tracking performance is gained on the cost of degrade performance system dynamics. Even through the VTL can keep tracking all satellite during the strong scintillation event, the position errors caused by the ionosphere scintillation is still quite large. Figure 7.10 shows the altitude solution of the VTL tracking loop. The position error caused by the scintillation is around 100 meters.

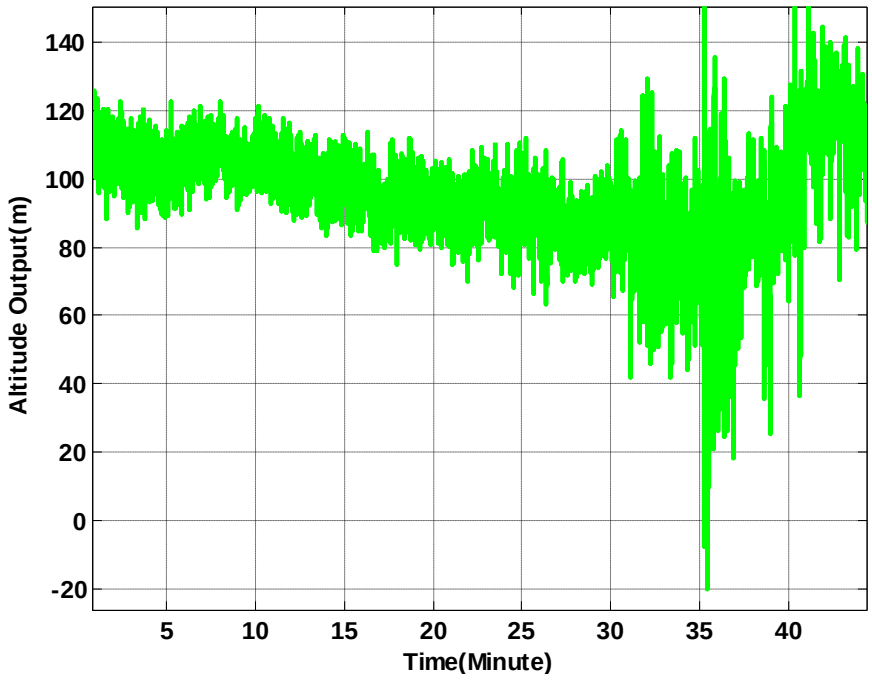

Figure 7.10: Altitude outputs of VTL for Ascension Island data.

7.7 Summary

A new VTL-assisted STL is proposed and the implementation is detailed in this chapter. The VTL combines the task of signal tracking and providing position solutions into one loop. The tracking performance of the new tracking loop structure is explored in details. The limitation of the extended Kalman filter is overcome by adjusting the covariance matrices adaptively. The results show that the VTL tracking the GPS satellite smoothly during a long period of strong scintillation events by making use of information from other heath satellites when the scalar tracking loop fails. The dynamic of the VTL is also significantly improved by prediction of the receiver platform dynamics. The receiver maintains lock of the signal during long time signal outages by making use available ephemerides and

position estimation. The theory deviation and processing results confirm that with valid ephemerides and pseudorange estimation accuracy within one chip offset, the most time-consuming signal re-acquisition can be avoided. The VTL is of practical importance as more navigation satellites would become available in the near future. The VTL can make use of the redundancy measurements to improve the performance of the receiver. The performance of the VTL can be further improved by making use of inertial system outputs. The inertial system can provide better short time position accuracy, so the code phase estimation of the VTL can be further improved as a result.

Chapter 8

Conclusion and Future Works

8.1 Conclusions

The work in this dissertation demonstrated that a general superpose software defined radio front end can be used to study ionosphere scintillation. A new robust tracking architecture is also proposed and evaluated with strong scintillation data and high dynamic data with signal outages. The results confirm that the new tracking loop can maintain lock of GNSS signals during strong scintillation event with signal fading of more than 20dB. Receiver integrity algorithms are integrated in the tracking loop to detect possible errors in a scalar channel. Once a possible error is detected, the vector tracking loop is used to assist the tracking of this channel. The re-acquisition of GNSS signal is avoided by the vector tracking loop. The contribution of this research is summarized in this chapter.

8.1.1 Multi-constellation Multi-frequency GNSS Software Receiver Development

A multi-constellation software receiver is developed and described in details in this work. The software contains algorithms for acquiring and tracking GNSS signals, computes navigation solutions, and generates ionosphere measurements. Currently, the software is able to process the following signals:

- GPS L1 C/A, L2C and L5 signals
- GLONASS L1 and L2 civil signals
- Galileo E1B, E1C

The algorithms to process E5A and E5B have been developed and tested. The USRP2 board is used as a flexible GNSS signal RF front end. Our objective is to evaluate the performance of the USRP2 front end as an ionosphere scintillation monitoring device. We established experimental setups that allow simultaneous data collection of the USRP2 front ends, an instrumentation quality custom GPS front end TRIGR, and two high end commercial GNSS receivers from the same antenna and driven by the same local oscillators. GPS L1, L2C, and L5 and GLONASS L1 and L2 raw IF samples were collected using the RF front ends, while the commercial receivers generated processed signal observables. The IF samples collected by the USRP2 front ends and the TRIGR front end were processed using the same software acquisition and tracking algorithms. The results show that USRP2 typically generates GPS (C/N_0) at about 1-3 dB below that of the TRIGR and 1-2dB less than that averaged output of NovAtel receiver. The carrier phase fluctuations generated by the two front ends are comparable to TRIGR as well. We do not have direct GLONASS signal

IF processing results comparison between the USRP2 and the TRIGR front end as the latter is a dedicated GPS front end. The USRP2 GLONASS processing results are compared with the outputs generated by the Septentrio PolaRxS receiver and their performances appear to be comparable. The results show that GLONASS signals have relatively large (C/N_0) and carrier phase fluctuation which appear to be unrelated to the signal propagation environment. The performance of the USRP2 board matches the Septentrio PolaRxS receiver.

8.1.2 Scintillation Events Analysis

During the past four years, Miami University and Ohio University has jointly deployed a real-time scintillation monitoring and raw RF data collection system at HAARP, Alaska. The setup is able to collect narrow band GPS L1, L2 and wideband GPS L5 and GLONASS L1 and L2 signals. The reconfigurable RF front end USRP2 is used to collect the wideband GNSS signals.

Several natural scintillation events and an artificial scintillation event on PRN 25 with S4 index ranging from 0.2 to 0.5 and carrier phase standard deviation ranging from 13 to 24 degrees on L1 signal and several dual frequency scintillation events are analyzed in detail. The results confirm that scintillation has stronger impacts on L2 and L5 than on L1. Our preliminary results also show that the scintillation on all three frequencies is highly correlated. A similar rate of fluctuations is observed on L1, L2 and L5 for both phase and amplitude. The amplitude correlation coefficients between L1, L2, and L5 are around 0.7 while the phase correlation coefficients are around 0.9. The scintillation time delay between different channels is close to zero.

8.1.3 Robust Tracking Loop Design

A new VTL-assisted STL is proposed and the implementation is detailed in this thesis. The VTL combines the task of signal tracking and providing position solutions into one loop. The tracking performance of the new tracking loop structure is explored in details. The limitation of the extended Kalman filter is overcome by adjusting the co-variance matrices adaptively. The results show that the VTL tracks the GPS satellite smoothly during a long period of strong scintillation events by making use of information from other heath satellites when the scalar tracking loop fails. The dynamic performance of the VTL is also significantly improved by incorporating prediction of the receiver platform dynamics. The receiver maintains lock of the signal during long time signal outages by making use of available ephemerides and position estimation. Theory and processing results confirm that with valid ephemerides and pseudorange estimation accuracy within one chip offset, the most time-consuming signal reacquisition can be avoided. The VTL is of practical importance as more navigation satellites become available in the near future. The VTL can make use of the redundancy measurements to improve the performance of the receiver. The performance of the VTL can be further improved by making use of inertial system outputs. An inertial system can provide better short time position accuracy, so the code phase estimation of the VTL can be further improved as a result.

8.2 Future Work

This dissertation focuses on the robust tracking loop design for strong scintillation conditions and signal outages. The new VTL assisted STL tracking loop has been tested with strong scintillation data collected during last solar maximum. The tracking performance

for the new GPS L5 signals is not evaluated due to lack of strong scintillation data on L5 channel. There are only two GPS satellite broadcasting signals on L5 (till June, 2012), so it is quite difficult to capture a strong scintillation event on L5. The new VTL assisted STL tracking loop has been tested with only one data set from GPS simulator. So the performance of the tacking loop cannot be quantified. The probability of loss lock of the tracking loop under different scenarios is of particular interest for further investigation. As mentioned in the previous part of the thesis that the error in both Doppler frequency and code phase estimation increase with time during signal outages, so the probability of loss lock with different time interval also needs to be studied. In order for further performance evaluation of the tracking loop, field data with signal outages can be collected in dense foliage and urban canyon. The integrity check algorithm plays an essential role in detecting the possible errors of the STL. The current threshold used in the tracking loop is selected based on experiential values. The false alarm rate corresponding to different thresholds is another focus of future work.

Another effort should be focused on the ionosphere scintillation modeling. The correlation of scintillations between signals at different frequencies is of vital importance for predicting the operational availability of future GPS system as the newly added GPS L2C and L5 signals which can provide accurate ionosphere delay estimation. Researchers also interested in the possibility that the GPS receiver may be able to rely on one frequency when it briefly loses other frequencies under scintillation. A previous study reported scintillation correlation coefficients of about 0.7 among signal intensities of L1 and L2 channels based on early GPS data collected at Thule, Greenland during 1989-1991 [El-Arini et al., 2009]. The similar results are also observed in our results. However, extensive scintillation data processing is still needed in order to model and characterize scintillation impacts.

Bibliography

[1] [Aarons, 1982] J. Aarons. Global morphology of ionospheric scintillations. Proceedings of the IEEE, 70(4):360378, 1982.

[2] [Abidi,1995] Abidi A.A., Direct-Conversion Radio Transceivers for Digital Communications. IEEE J. Solid-State Circuits, vol. 30, no. 12, pp. 1399-1410

[3] [Akos,1997] Akos D. M., A software radio approach to global navigation satellite system receiver design. Dissertation, Ohio University

[4] [Basu, 1981] S. Basu. Equatorial scintillationsa review. Journal of Atmospheric and Terrestrial Physics, 43(5-6):473489, 1981.

[5] [Basu et al., 1985] S. Basu, S. Basu, E. MacKenzie, and H. E. Whitney. Morphology of phase and intensity scintillations in the auroral oval and polar cap. Radio Science, 20(3):347356, 1985.

[6] [Beach and Kintner, 2001] T. L. Beach and P. M. Kintner. Development and use of a GPS ionospheric scintillation monitor. IEEE Transactions on Geoscience and Remote Sensing, 39(5):918928, 2001.

[7] [Beniguel and Adam, 2007] Y. Beniguel and J.-P. Adam. Effects of scintillations in GNSS operation. Springer Netherlands, 2007.

[8] [Best 1997] Best, Roland E., Phase Locked Loops: Design,Simulation, and Applications, 3^{rd} Ed., McGraw Hill, ISBN: 0070060517,1997.

[9] Braschak M., Brown H. Jr., Carberry J., Grant T., Hatten G., Patocka R., Watts E. (2010), GPS IIF satellite overview, Proc. ION GNSS, Portland, OR

[10] Brown, R.G. and Hwang, P.Y.C., Introduction to Random Signals and Applied Kalman Filtering with Matlab Exercises and Solutions, 3rd Edition, Wiley, 1996.

[11] [Cabler and DeCleene, 2002] H. Cabler and B. DeCleene. LPV: New, improved WAAS instrument approach. In Proceedings of the 15th International Technical Meeting of the Satellite Division of the Institute of Navigation, pages 10131021,2002.

[12] [Cao et al., 2008]Cao C., Jing G., Luo M., COMPASS satellite navigation system development. PNT challenges and opportunities symposium, Stanford, California

[13] [Chiou et al., 2005] Chiou, T.Y., GPS Receiver Performance Using Inertial-Aided Carrier Tracking Loop, Proc. ION GNSS 2005, pp. 2895-2910.

[14] [Chiou et al., 2008] T.-Y. Chiou, J. Seo, T. Walter, and P. Enge. Performance of a Doppler-aided GPS navigation system for aviation applications under ionospheric scintillation. In Proceedings of the 21st International Technical Meeting of the Satellite Division of the Institute of Navigation, pages 1139-1147, 2008.

[15] [Conker et al., 2003] R. S. Conker, M. B. El-Arini, C. J. Hegarty, and T. Hsiao. Modeling the effects of ionospheric scintillation on GPS/satellite-based augmentation system availability. Radio Science, 38(1):23, 2003.

[16] [Copps 1980] E. M. Copps, G. J. Geier, W. C. Fidler, and P. A. Grundy, Optimal processing of GPS signals, Navigation, vol. 27, no. 3, pp. 171182, 1980.

[17] [Crane, 1977] R. K. Crane. Ionospheric scintillation. Proceedings of the IEEE, 65(2):180199, 1977.

[18] Crols J. and Steyaert M. (1995), A Single-Chip 900 MHz CMOS Receiver Front-End with a High Performance Low-IF Topology. IEEE J. Solid-State Circuits, Vol. 30, No. 12, pp. 1483-1492

[19] Crols J. and Steyaert M. (1998), Low-IF Topologies for High-Performance Analog Front Ends of Fully Integrated Receivers. IEEE Trans. Circuits Sys.-II, vol. 45, no. 3, pp. 269-282

[20] [Datta-Barua et al., 2008] S. Datta-Barua, T. Walter, J. Blanch, and P. Enge. Bounding higher-order ionosphere errors for the dual-frequency GPS user. Radio Science, 43(5), 2008.

[21] [El-Arini et al., 2003] M. B. El-Arini, R. S. Conker, S. D. Ericson, K. W. Bean, F. Niles, K. Matsunaga, and K. Hoshinoo. Analysis of the effects of ionospheric scintillation on GPS L2 in Japan. In Proceedings of the 16th International Technical Meeting of the Satellite Division of the Institute of Navigation, 2003.

[22] [El-Arini, 2009] M. B. El-Arini. Estimating time between fades at Naha, Japan (a case study), personal communication, 22 April, 2009.

[23] [El-Arini et al., 2009] M. B. El-Arini, J. Secan, J. A. Klobuchar, P. H. Doherty,G. Bishop, and K. Groves. Ionospheric effects on GPS signals in the arctic region using early GPS data from Thule, Greenland. Radio Science, 44:14, 2009.

[24] [Enge, 1999] P. Enge. Local area augmentation of GPS for the precision approach of aircraft. Proceedings of the IEEE, 87(1):111132, 1999.

[25] [Forney 1974] Forney, G. D., Jr., "Convolutional Codes II: Maximum-Likelihood Decoding," Information Control, vol. 25, pp. 222-226, June, 1974.

[26] [Fremouw and Ishimaru, 1992] E. J. Fremouw and A. Ishimaru. Intensity scintillation index and mean apparent radar cross-section on monostatic and bistatic paths. Radio Science, 27(4):539543, 1992.

[27] [Fremouw et al., 1978] E. J. Fremouw, R. L. Leadabrand, R. C. Livingston, M. D. Cousins, C. L. Rino, B. C. Fair, and R. A. Long. Early results from DNA wideband satellite experimentcomplex-signal scintillation. Radio Science, 13(1):167187,1978.

[28] [Fremouw et al., 1980] E. J. Fremouw, R. C. Livingston, and D. A. Miller. On the statistics of scintillating signals. Journal of Atmospheric and Terrestrial Physics,42(8):717731, 1980.

[29] [Gallager, 1996] Robert G. Gallager. Discrete stochastic processes. The Kluwer international series in engineering and computer science. Kluwer Academic Publishers,Boston, 1996.

[30] [Ganguly et al., 2004] S. Ganguly, A. Jovancevic, A. Brown, M. Kirchner, S. Zigic,T. Beach, and K. M. Groves. Ionospheric scintillation monitoring and mitigation using a software GPS receiver. Radio Science, 39(1):9, 2004.

[31] [Gao et al., 2009a] G. X. Gao, A. Chen, S. Lo, D. De Lorenzo, T.Walter, and P. Enge. Compass-M1 broadcast codes in E2, E5b, and E6 frequency bands. IEEE Journal of Selected Topics in Signal Processing, 3(4):599-612, 2009.

[32] [Gao et al., 2009b] G. X. Gao, L. Heng, D. De Lorenzo, S. Lo, D. Akos, A. Chen, T. Walter, P. Enge, and B. Parkinson. Modernization milestone: observing the first GPS satellite with an L5 payload. Inside GNSS, (May/June):30-36, 2009.

[33] [GLONASS ICD 2002] GLONASS Interface Control Document Version 5.0

[34] [Groves et al., 2000] Groves K., Basu S., Quinn J., Pedersen T., Falinski K., Brown A., Silva R., and Ning P. (2000), A comparison of GPS performance in a scintillating environment at Ascension Island. Proc. ION GPS, Salt Lake City, UT

[35] Gunawardena S., Zhu Z., van Graas F. (2008), Triple Frequency RF Front-End for GNSS Instrumentation Receiver Applications. Proc. ION GNSS, Savanna, GA

[36] [Gwal et al., 2004] A. K. Gwal, S. Dubey, and R. Wahi. A study of L-band scintillations at equatorial latitudes, volume 34 of Advances in Space Research, pages 2092-2095. Pergamon-Elsevier Science Ltd, Kidlington, 2004.

[37] [Heller et al., 1971] Heller, J. A., and I. M. Jacobs, Viterbi Decoding for Satellite and Space Communications, IEEE Transactions on Communication Technology, vol. COM-19, pp. 835-848, October, 1971.

[38] [Hegarty et al., 1997] Hegarty, C.J., Analytical Derivation of Maximum Tolerable In-Band Interference Levels for Aviation Applications of GNSS, Journal of The Institute of Navigation, Vol. 44, No.1, pp. 25-34, Spring 1997.

[39] [Hein et al., 2005]Hein G. W., Wallner S., Development and design of Galileo. Proc. ION GPS, Cambridge, MA

[40] [Hinedi 1985] Hinedi S. High-Dynamic GPS Tracking. Final Report,JPL Publication 88-35.

[41] Hogenauer E.B. (1981), An economical class of digital filters for decimation and interpolation. IEEE Trans. Acous. Speech Signal Proc., ASSP-29(2):155-162

[42] [Humphreys et al., 2010a] Humphreys T. E., Psiaki M. L., Ledvina B. M., Cerruti A. P., Kintner P. M., Data-driven testbed for evaluating GPS carrier tracking loops in ionospheric scintillation. IEEE Trans. Aero. Ele. Sys., vol.46, no. 4, pp.1609-1623

[43] [Humphreys et al., 2010b] Humphreys T. E., Psiaki M., Ledvina B., Cerruti A., and Kintner P. M., Jr., Modeling the effects of ionospheric scintillation on GPS carrier phase tracking. IEEE Trans. Aero. Ele. Sys., vol.46, no. 4, pp. 1624-1637

[44] [Humphreys et al., 2009] T. E. Humphreys, M. L. Psiaki, J. C. Hinks, B. OHanlon,and P. M. Kintner. Simulating ionosphere-induced scintillation for testing GPS receiver phase tracking loops. IEEE Journal of Selected Topics in Signal Processing,3(4):707-715, 2009.

[45] [Irsigler et al., 2002] Irsigler, M. and Eissfeller, B., PLL Tracking Performance in the Presence of Oscillator Phase Noise, GPS Solutions, Volume 5, Number 4, Spring 2002, Wiley Periodicals Inc.,2002

[46] [Kaplan and Hegarty, 2006] Elliott D. Kaplan and C. Hegarty. Understanding GPS : principles and applications. Artech House mobile communications series. Artech House, Boston, 2nd edition, 2006.

[47] [Kayton and Fried, 1997] M. Kayton and W. Fried. Avionics navigation systems. J.Wiley, New York, 2nd edition, 1997.

[48] [Kelly and Davis, 1994] R. J. Kelly and J. M. Davis. Required navigation performance(RNP) for precision approach and landing with GNSS application. Navigation.Journal of the Institute of Navigation, 41(1):1-30, 1994.

[49] [Kim et al., 2003] Kim, I., R.S. Conker, S.D. Ericson, C.J. Hegarty, M. Tran, M.B. El-Arini, Preliminary Evaluation of the Effects of Scintillation on L5 GPS and SBAS Receivers Using a Frequency Domain Scintillation Model and Simulated and Analytical Receiver Models, Proc. ION ITM, Anaheim, CA, January 2003.

[50] [Kintner et al., 2007] P. M. Kintner, B. M. Ledvina, and E. R. De Paula. GPS and ionospheric scintillations. Space Weather-the International Journal of Research and Applications, 5(9):23, 2007.

[51] [Klobuchar et al., 1996] Klobuchar, J. A., Ionosphere effects on GPS, Ch.12 in global Positioning System: Theory and Applications, Volume 1, edt. B.W. Parkinson, J. J. SpilkerJr., AIAA, 1996.

[52] [Knight, 2000] M. F. Knight. Ionospheric scintillation effects on global positioning system receivers. PhD thesis, 2000.

[53] [Lauri et al., 2008] Lauri Wirola and Jari Syrjarinne, GLONASS Orbits in GPS/Galileo-style Ephemeredes for Assisted GNSS, Proc. ION NTM 2008, Jan. 28-30, 2008, San Diego, California.

[54] [Lashley et al., 2009] Lashley, M., D. M. Bevly, and J. Y. Hung, Performance analysis of vector tracking algorithms for weak GPS signals in high dynamics, IEEE Journal of Selected Topics in Signal Processing, vol. 3, pp. 661673, 2009.

[55] [Lee, 1992] Y. C. Lee. Receiver autonomous integrity monitoring (RAIM) capability for sole-means GPS navigation in the oceanic phase of flight. IEEE Aerospace and Electronics Systems Magazine, 7(5):29-36, 1992.

[56] [Misra et al., 2006] P. Misra and P. Enge. Global positioning system : signals, measurements, and performance. Ganga-Jamuna Press, Lincoln, MA, 2nd edition,2006.

[57] [Morton et al.,2009] Morton, Y. T., Q. Zhou, and F. van Graas, Assessment of second order ionosphere error in GPS range observables using Arecibo incoherent scatter radar measurements, Radio Sci., 44, RS1002, doi:10.1029/2008RS003888, 2009.

[58] [Natali 1984] Natali, F.D., AFC Tracking Algorithms, IEEE Transactions Communications, Vol.COM-32, No. 8, pp. 935-947, August 1984.

[59] [Natali 1986] Natali, F.D., Noise Performance of a Cross-Product AFC with Decision Feedback for DPSK Signals, IEEE Transactions Communications, Vol. COM-34, No. 3, pp. 303-307,March 1986.

[60] [Nee et al., 1991] D. J. R. V. Nee and A. J. R. M. Coenen, New fast GPS code-acquisition technique using FFT, Electronics Letters, vol. 27, no. 2, pp. 158 160, Jan. 1991.

[61] OHanlon B., Psiaki M., Powell S., Bhatti J., Humphreys T. E., Crowley G., and Bust G. (2011), CASES: A smart, compact GPS software receiver for space weather monitoring, Proc. ION GNSS, Portland, Oregon

[62] [Pelgrum et al., 2011] W. Pelgrum, Y. Morton, F. van Graas, S. Gunawardena1, M. Bakich, D. Charney, S. Peng, J. Triplett, A. Vermuru, P. Vikram, Measurement and analysis of artificially-generated and natural ionosphere scintillations effects on GNSS signals, ION ITM, San Diego, Jan. 2011.

[63] Peng S., and Morton Y. (2010), A USRP2-Based Multi-Constellation and Multi-Frequency GNSS Software Receiver for Ionosphere Scintillation Studies. Proc. ION ITM, San Diego, CA

[64] Peng S., Morton Y., Di R. (2012), A multiple-frequency GPS software receiver design based on a vector tracking loop, IEEE/ION PLANS 2012, Myrtle Beach, SC

[65] [Peterson et al., 1961] Peterson, W. W., and Brown, D.T., Cyclic Codes for Error Detection. In Proceedings of the IRE, pp.228235, January 1961.

[66] [Pullen et al., 2009] S. Pullen, Y. S. Park, and P. Enge. Impact and mitigation of ionospheric anomalies on ground-based augmentation of GNSS. Radio Science, 44,2009.

[67] [Razavi 1997] Razavi B., Design Considerations for Direct-Conversion Receivers. IEEE Transactions on Circuits and Systems-II, vol. 44, No. 6, pp. 428-435

[68] Razavi A., Begre-Ebgiabher D., Akos D. (2008), Carrier loop architectures for tracking weak GPS signals. IEEE Trans. Aero. Elec. Sys., 44(2), pp.697-710

[69] [Revnivykh 2010] Revnivykh S., GLONASS status and progress, Proc. ION GPS, Portland, Oregon

[70] [Rino 1979] Rino, C.L., A Power Law Phase Screen Model for Ionospheric Scintillation: 1. Weak Scatter, Radio Science, Vol. 14, No. 6, pp. 1135-1145, 1979a.

[71] Rudell J.C., Ou J., Cho T.B., Chien G., Brianti F., Weldon J.A., and Gray P.R. (1997), A 1.9-GHz Wide-Band IF Double Conversion CMOS Receiver for Cordless Telephone Applications. IEEE Journal of Solid-State Circuits, Vol. 32, No. 12, pp. 2071-2088

[72] [Sampei et al., 1997] S. Sampei and K. Feher, Adaptive dc-offset compensation algorithm for burst mode operated direct conversion receivers, Proc. 42nd IEEE Vehic. Tech. Conf., pp.9396,Denver, May 1997.

[73] [Secan et al., 1997] J. A. Secan, R. M. Bussey, E. J. Fremouw, and S. Basu. High latitude upgrade to the wideband ionospheric scintillation model. Radio Science,32(4):1567-1574, 1997.

[74] [Seo et al., 2009a] J. Seo, T. Walter, T. Y. Chiou, and P. Enge. Characteristics of deep GPS signal fading due to ionospheric scintillation for aviation receiver design. Radio Science, 44, RS0A16, 2009.

[75] [Seo et al., 2009b] J. Seo, T. Walter, and P. Enge. Availability impact on GPS aviation due to strong ionospheric scintillation. IEEE Transactions on Aerospace and Electronic Systems, submitted, 2009.

[76] [Seo et al., 2011] Seo J., Walter T., Enge P., Correlation of GPS signal fades due to ionospheric scintillation for aviation applications. Adv. Space Res., vol. 47, pp.1777-1788

[77] [Sennott 1984] J. W. Sennott, A flexible GPS software development system and timing analyzer for present and future microprocessors, Navigation, vol. 31, no. 2, pp. 8495, 1984.

[78] [Skone et al., 2008] Skone S., Man F., Ghafoori F., and Tiwari R. (2008), Investigation of scintillation characteristics for high latitude phenomena. Proc. ION GNSS, Savana, GA

[79] [Singleton et al., 1961] D. Singleton, G. J. E. Lynch, and J. A. Thomas. Field-aligned ionospheric irregularities and scintillation of satellite radio transmissions. Nature,189(475):30, 1961.

[80] [So et al., 2010] So, Hyoungmin; Lee, Taikjin; Jeon, Sanghoon; Kim, Chongwon; Kee, Changdon; Kim, Taehee; Lee, Sanguk. 2010. Implementation of a Vector-based Tracking Loop Receiver in a Pseudolite Navigation System. Sensors 10, no. 7: 6324-6346.

[81] [Spilker 1996] Spilker, J.J., Fundamentals of Signal Tracking Theory. In: Global Positioning System: Theory and Applications, volume I, eds. Parkinson, B. W. and Spilker, J. J. American Institute of Aeronautics and Astronautics, Inc, 1996,pp. 245-328

[82] [Tran 2004] Tran, M., Performance evaluations of the new GPS L5 and L2 Civil (L2C) signals, Journal of the Institute of Navigation, vol. 51, no. 3, pp. 199212, 2004.

[83] [Tsui 2000] Tsui, J. B. Y., Fundamentals of Global Positioning System Receivers, A software approach, 1st edition, John Wiley and Sons, 2000.

[84] Van Dierendonck, A.J., Klobuchar, J., and Hua, Q., Ionospheric Scintillation Monitoring Using Commercial Single Frequency C/A Code Receivers, Proceeding of the ION-GPS 1993, Salt Lake City, UT, September, 1993.

[85] [van Dierendonck 1996] van Dierendonck A.J. , GPS Receivers. In: Global Positioning System: Theory and Applications,Vol.I, Parkinson, B.W. and Spilker, J.J. Jr., eds., AIAA, pp. 329-407

[86] van Dierendonck A. J., Hua Q., Fenton P., Klobuchar J. (1996), Commercial ionospheric scintillation monitoring receiver development and test results. Proc. ION GPS, Cambridge, MA

[87] Van Dierendonck, A.J., Reddan, P., and Nicholson M., GPS Receiver Performance Characterization under Simulated Ionospheric Scintillation Environments, Proceeding of the ION-NTM 1999, San Diego, CA, January, 1999.

[88] [Van Dierendonck et.al, 2000] A. J. Van Dierendonck and C. Hegarty. The new L5 civil GPS signal. GPS World, (September):64-72, 2000.

[89] [van Dierendonck, A. J. 2005], How GPS receivers measure (or should measure) ionospheric scintillation and TEC and how GPS receivers are affected by the ionosphere? Proc. Ionosphere Effects Sym., Alexandria, VA

[90] [Viterbi et al., 1967] Viterbi, A. J., "Error Bounds for Convolutional Codes and an Asymptotically Optimum Decoding Algorithm," IEEE Transactions on Information Theory , vol. IT-13, pp. 260-269, April 1967.

[91] [Walter et al., 2004] T.Walter, S. Datta-Barua, J. Blanch, and P. Enge. The effects of large ionospheric gradients on single frequency airborne smoothing filters for WAAS and LAAS. In Proceedings of the 2004 National Technical Meeting of the Institute of Navigation, pages 103-109, 2004.

[92] [Walter et al., 2008] T.Walter, P. Enge, J. Blanch, and B. Pervan. Worldwide vertical guidance of aircraft based on modernized GPS and new integrity augmentations. Proceedings of the IEEE, 96(12):1918-1935, 2008.

[93] [Ward 1998] Ward, P., Performance Comparisons Between FLL, PLL and a Novel FLL-assisted-PLL Carrier Tracking Loop Under RF Interference Conditions, Proc. ION GPS, p783-795, Nashvill, TN., September 1998.

[94] [Vikram 2011] Vikram P., Event driven GPS data collection system for studying ionospheric scintillation, MS thesis, Miami University

[95] [Wang et al., 2011] Wang J., Morel J., Morton Y. (2011), Predicting GLONASS satellite orbit based on an almanac conversion algorithm for controlled ionosphere scintillation experiment planning. Proc. ION GNSS, Portland, OR

[96] [Wang et al., 2012] Wang J., Morton Y., Zhou Q., van Graas F., Pelgrum W. (2012), Time-frequency analysis of ionosphere scintillations observed by a GNSS receiver array, Proc. IEEE PLANS, Myrtle Beach, SC

[97] Won Jong-Hoon, Bernd Eissfeller, Thomas Pany, Implementation, Test and Validation of a Vector-Tracking-Loop with the ipex Software Receiver, Proc. ION GPS, Portland, OR, Sept. 2011.

[98] [Yoshida et al., 2008] H. Yoshida, H. Tsurumi, and Y. Suzuki, DC offset canceller in a direct conversion receiver for QPSK signal reception, in 9th IEEE Personal, Indoor, Mobile Commun. Symp., vol. 3,pp. 13141318, Sep. 1998.

[99] [Zhang et al., 2010]Zhang L., Morton Y., Zhou Q., van Graas F., and Beach T. (2010), Characterization of GNSS signal parameters under ionosphere scintillation conditions using sequential and batch-based tracking algorithms. Proc. IEEE PLANS, Palm Springs, CA